Dissertation

submitted to the

Combined Faculty of Mathematics, Engineering and Natural Sciences
of Heidelberg University, Germany

for the degree of

Doctor of Natural Sciences

Put forward by

Ruth Christine Winter
born in Berlin, Germany

Oral examination:
12 December 2025

From Radiation Track to DNA Damage

The Biophysics Behind α– and β^-–Emitters
in Targeted Radionuclide Therapy

Referees: Prof. Dr. Mark E. Ladd
Prof. Dr. Leif Schröder

Von Strahlenspuren zu DNA-Schäden

Die Biophysik hinter α– and β^-–Emittern in der gezielten Radionuklidtherapie

Metastasierende Krebserkrankungen stellen eine zentrale Herausforderung dar und erfordern innovative Behandlungsansätze wie die gezielte Radionuklidtherapie (TRT). Zur Optimierung von TRT und Bekämpfung von Radioresistenzen ist ein grundlegendes Verständnis der radiobiologischen Mechanismen entscheidend, welche vom Radionuklidtyp, der Aktivität sowie der zellulären Lokalisation des Radiopharmazeutikums abhängig sind. Anhand des zielgerichteten Radiopharmazeutikums PSMA-617 für Prostatakrebs wird untersucht, wie die physikalischen Unterschiede des klinisch-erprobten α-Emitters ^{225}Ac und β^--Emitters ^{177}Lu die strahlenbiologische Wirksamkeit und den Therapieerfolg beeinflussen. Die Auswertung von DNA-Doppelstrangbrüchen (DSB) mittels γH2AX-Immunfluoreszenzfärbung und Zellproliferationsassays zeigte eine Überlegenheit des α-Emitters gegenüber dem β^--Emitter, welcher mit nur einem Prozent der Aktivitätsmenge eine vergleichbare Anzahl an DSB induzierte. Durch gezielte Internalisierung konnte die therapeutische Wirksamkeit der α-Strahlung mit kurzer Reichweite (47–85 µm) signifikant verbessert werden, jedoch nicht bei β^--Strahlung mit längerer Reichweite (1,5–1,7 mm). Die Anzahl an DSB blieb nach α-Exposition bis zu 72 Stunden auf einem hohen Niveau, während sie nach β^--Exposition und externer Photonenbestrahlung zurückging. TRT in Kombination mit DNA-PK-Inhibitor Nedisertib® zeigte erhöhte Wirksamkeit und wies sogar bei niedrigen Inhibitorkonzentrationen ein Potenzial zur Reduzierung der eingesetzten Aktivität und Überwindung von Radioresistenzen auf. Diese Ergebnisse unterstreichen die Bedeutung der Strahlenbiologie in TRT und heben dabei die Relevanz von α-Emittern sowie Kombinationsstrategien für effektivere und verträglichere Krebstherapien hervor.

From Radiation Track to DNA Damage

The Biophysics Behind α– and β^-–Emitters in Targeted Radionuclide Therapy

Metastatic cancer remains a major challenge, necessitating innovative treatments like Targeted Radionuclide Therapy (TRT). Understanding the underlying radiobiological mechanisms influenced by radionuclide type, administered activity, and cellular localization is of utmost importance for optimizing TRT effectiveness and combating radioresistance. This study uses the prostate cancer-addressing radiopharmaceutical PSMA-617 to investigate how the physical differences between clinically-used α-emitter ^{225}Ac and β^--emitter ^{177}Lu affect radiobiological efficacy and therapeutic outcome. Immunofluorescent γH2AX staining of DNA double-strand breaks (DSBs) and cell proliferation assays demonstrated that the α-emitter outperformed the β^--emitter, achieving a similar amount of DSBs with only 1 per cent of the activity. Notably, targeted internalization significantly enhanced therapeutic efficacy of short-range α-emitters (47–85 µm), while having negligible impact for longer-range β^--emitters (1.5–1.7 mm). Furthermore, the amount of α-induced DSBs remained high for up to 72 hours, while it decreased for β^--exposure and external photon irradiation. Combining TRT with the DNA-PK inhibitor Nedisertib® further enhanced treatment efficacy and demonstrated resistance-overcoming potential, allowing for a reduction in activity even at low inhibitor concentrations. These findings underscore the importance of radiobiology in TRT and highlight the relevance of α-emitters as well as combination strategies for more effective and well-tolerated cancer treatments.

Contents

List of Abbreviations

DNA	deoxyribonucleic acid
DNA-PK	DNA-dependent protein kinase
DNA-PKcs	DNA-dependent protein kinase catalytic subunit
DNA-PKi	DNA-PK inhibitor
DSB	double strand break
EBRT	external beam radiation therapy
HR	homologous recombination
LET	linear energy transfer
mCRPC	metastatic castration-resistant prostate cancer
NHEJ	non homologous end-joining
PARPi	poly ADP-ribosylation inhibitor
PSMA	prostate-specific membrane antigen
ROS	reactive oxygen species
SoC	standard of care
SSB	single strand break
SSTR2	somatostatin receptor type 2
TαT	targeted alpha therapy
TRT	targeted radionuclide therapy

1 Introduction

1.1 Motivation

What disease do you fear the most?

Is your answer Cancer*?*

Then you are not alone.

Most people know someone who has been or is battling cancer, making it a personal matter and a very present reality for many. A cancer diagnosis often evokes feelings of helplessness and uncertainty, along with drastic changes to everyday life - not only for patients, but also for their relatives. Furthermore, cancer does not discriminate by age or social status and can emerge suddenly and unpredictably. These personal experiences contribute to widespread fear throughout society.

This is reflected in numbers as well, according to a survey conducted by DAK-Gesundheit, a major German statutory health insurance provider, 73% of Germans named cancer as the disease they fear the most [1]. Yet, statistically, cardiovascular diseases remain the leading cause of death in Germany [2]. Why then is cancer feared more? Because fear is not just about statistics and rationality, it is about uncertainty and the unknown. The emotional stress, the exhausting treatments, the unpredictability of treatment outcomes, as well as the looming threat of recurrence all contribute to the deep fear surrounding cancer.

To overcome this fear, cancer treatments must not only be effective but also well-tolerated. These efforts must be complemented and reinforced by a deeper understanding of cancer biology, effective early detection methods, and accessible, widely available screening programs. This need becomes even more urgent as the number of cancer cases is expected to rise significantly in the coming years. The International Agency for Research on Cancer (IARC) projects that approximately one in five individuals will develop cancer during their lifetime [3], with a staggering 21.3 million new cancer diagnoses anticipated worldwide by 2025 [4].

As cancer is as diverse as humanity, it is nearly impossible to find a universal “one

to fit them all" treatment. Despite this challenge, significant progress has been made in recent decades, with overall survival rates steadily increasing over time. Moreover, since 1995, the European Medicines Agency (EMA) has approved almost 200 new cancer medications [5], reflecting the rapid advancement of cancer research and treatment options.

However, what constitutes an ideal cancer treatment? An effective cancer treatment should ideally fulfill the following key criteria:

High Specificity: selectively targeting cancer cells while sparing normal, healthy cells

High Efficacy: completely eliminating all cancerous cells, even in advanced disease stages with metastatic spread

Minimal Toxicity: inducing few or manageable side effects that do not compromise quality of life

This is what targeted radionuclide therapy (TRT) and targeted alpha therapy (TαT) aim for. As endoradiotherapy - internal radiotherapy - they are both systemic and cancer-specific targeted treatments. The underlying concept involves conjugating a (DNA) damaging agent - a radionuclide - with a target-specific vector, typically a small molecule or antibody, which enables the selective differentiation between tumor cells and healthy tissue. This targeted approach allows for the precise delivery of a lethal dose directly to the tumor site. Furthermore, due to its systemic nature, this therapy can simultaneously treat both the primary tumor and metastatic sites. As a result, TRT and TαT, demonstrate mostly mild side effects, leading to improved quality of life and prognosis for patients.
Notably, the treatment of metastatic castration-resistant prostate cancer (mCRPC) with prostate-specific membrane antigen (PSMA)-targeting radioligands, namely [^{177}Lu]Lu-PSMA-617 and [^{225}Ac]Ac-PSMA-617, has emerged as a highly effective platform for managing advanced disease [6, 7]. The radiopharmaceutical [^{177}Lu]Lu-PSMA-617 received FDA (U.S. Food and Drug Administration) and EMA approval in 2022 as Pluvicto®(Novartis, Basel, Switzerland), marking a significant milestone in TRT. This achievement was made possible through a huge effort of multiple disciplines, as TRT requires the collaboration and synergy of radiochemistry and -pharmacy, physics, biology, and medicine. To enumerate just some of the challenges that needed to be overcome in developing TRT: synthesizing and optimizing pharmacophores for specific binding, developing suitable chelators for the

radionuclide coordination and optimizing labeling procedures, evaluating compound's stability, considering and identifying radionuclides with desirable properties for therapy and potential imaging applications, producing and delivering high-purity radionuclides, estimating and calculating absorbed dose and biological effectiveness of the compound, and immaculately translating these findings into clinical practice and securing marketing authorization.
With the first approval of TRT as a treatment option, new challenges and opportunities arise. A comprehensive understanding of radiobiology and the optimization of dosimetry are crucial aspects for successful therapy planning, optimization, and outcome prediction. While these aspects are well understood in the established standard of care (SoC) treatment of external beam radiation therapy (EBRT), the mechanisms unique to TRT present a more complex landscape and comprehensive studies have only recently begun [8]. Furthermore, the mechanisms in TRT affecting DNA damage induction and therefore radiation dose delivery and biological effectiveness are more complex and multi-parameter-dependent. The interplay of various factors influences DNA damage and biological effectiveness in TRT. These factors include radionuclide distribution, delivery, and cellular localization, as well as the specific properties of the radionuclide, such as emitter type and half-life. Additionally, activity concentration and exposure time play a crucial role for the total delivered dose.
The complexity of these interactions makes it difficult to predict the biological outcome and effectiveness of TRT. Furthermore, the principles governing DNA damage induction and repair may differ from those observed in EBRT, since TRT continuously introduces DNA damage over an extended period of time, whereas EBRT delivers the dose inducing DNA damage in a short burst during the irradiation treatment, allowing cells undisturbed time for repair afterwards. Therefore, the relationship between absorbed dose and tissue damage needs to be redefined for TRT and compared to current knowledge from EBRT. As illustrated in Figure 1.1, solving this complex, multidisciplinary puzzle is crucial to advancing TRT to the next level.

This thesis aims to contribute to a profound understanding of the fundamental principles behind DNA damage induction and repair, with a focus on the unique characteristics of TRT. By closely evaluating the different physical parameters of TRT, this work will additionally provide essential knowledge to enhance the accuracy and effectiveness of TRT dosimetry. The key research questions driving this work are outlined in Section 1.2.

Figure 1.1: **The puzzle of Targeted Radionuclide Therapy:** the field of TRT presents a complex and multidisciplinary puzzle, with each piece relying on input from various disciplines. The therapeutic outcome depends on precise understanding and management of factors such as biological distribution, specific targeting capabilities, cellular uptake, and the unique properties of the radionuclide itself, including emitter type, half-life, activity concentration, and exposure time. This intricate interplay between these variables shapes the delivery and effectiveness of radiation-induced DNA damage, requiring careful optimization for effective therapy planning and outcome evaluation. By contributing a part in unraveling this complex puzzle, we aim to unlock the full potential of TRT, improving treatment optimization and outcomes for patients who require innovative therapies for challenging diseases. Created in Biorender https://BioRender.com

1.2 Research Questions

This thesis addresses four key research questions that aim to bridge existing knowledge gaps in the field. The subsequent paragraphs will elaborate on each question, highlighting its relevance to current research deficits and the potential benefits of finding answers.

Q1 How do physical parameters such as activity concentration, emitter type, and exposure time impact the biological effectiveness of TRT?

As outlined in the previous Section 1.1, the outcome of TRT depends on multiple physical parameters influenced by the used radionuclide. Notably, α- and β^--emitters exhibit distinct characteristics in terms of their range in tissue, with α-particles having a limited range of 20 µm to 80 µm and β^--particles exhibiting a significantly longer range of 2 mm to 11.5 mm. Due to their relatively short range, α-emitters selectively damage primarily targeted cells expressing the corresponding receptor, making them very suitable for TRT due to their high specificity. In contrast, β^--radionuclides may be more suitable for treating heterogeneous tumors, as their extended range facilitates damaging of non-target-expressing tumor cells as well [9, 10]. The distinct physical properties of these particle types can lead to unique damage patterns in DNA that must be taken into account for accurate dosimetry and optimal biological effectiveness. A thorough understanding of these distinct properties is crucial for optimizing dosimetry and maximizing therapeutic efficacy. However, a major challenge in current TRT studies is the multitude of variables that can be manipulated, resulting in a scarcity of consistent comparisons between different emitters under uniform experimental conditions. This lack of standardization hinders the quantitative evaluation of their biological effectiveness and the impact of specific physical parameters. Furthermore, existing studies often suffer from methodological limitations, such as using only one activity level or exposure time and inconsistent reporting of applied activities. This makes it challenging to compare the properties and effects of different radionuclides evaluated in various experimental setups. This knowledge gap in understanding the specific impact of radionuclide physical properties on DNA damage patterns is addressed with this research question.

Q2 How can a single-cell simulation be designed to estimate absorbed dose as a function of subcellular radionuclide localization and to model DNA damage induction?

The different physical properties of various radionuclides necessitate the use of distinct activity ranges to achieve comparable biological effectiveness. For instance, 100 kBq can lead to complete different biological response, depending on the employed radionuclides. Consequently, activity alone is not a suitable parameter for quantitative comparison between radionuclides. As the biological effectiveness is strongly correlated with the absorbed dose, the absorbed dose would be a valuable parameter for comparing studies. However, determining the absorbed dose experimentally in TRT is extremely challenging, if not impossible, and thus requires accurate and reliable modeling within a simulation framework. To accurately predict the biological response to TRT, it is essential to understand how the localization of the radionuclide (whether membrane-bound or internalized) affects the absorbed dose distribution and subsequent DNA damage. Matching experimental data with sophisticated simulations can help to understand the complex relationship between radionuclide distribution and biological effect, ultimately leading to the development of a robust simulation framework for improved dosimetry. To simulate the complex physical and biological processes involved in TRT, Monte Carlo modeling is a critical computational approach. Monte Carlo methods rely on the use of random sampling techniques to simulate the stochastic nature of radiation transport. One of the most widely used platforms for such simulations is Geant4 (Geometry and Tracking), an open-source Monte Carlo simulation toolkit developed by CERN. For radiobiological applications, Geant4-DNA, an extension of Geant4, provides the tools necessary to simulate radiation interactions at the molecular and cellular levels. It includes dedicated models for simulating track structures, direct and indirect DNA damage, and subsequent biological endpoints such as strand breaks and complex DNA lesions. Although several simulation studies have attempted to model the effects of TRT, there is substantial variability in their scope and design. Differences in geometry, cellular models, radionuclide distribution assumptions, physics models, and biological endpoints (e.g., DNA damage types) contribute to a fragmented understanding. A comprehensive simulation framework that integrates all relevant parameters - particularly the precise subcellular localization of radionuclides - is needed to better quantify how localization influences absorbed dose and resulting biological outcomes.

Q3 What biological differences exist in the induction (e.g., size, structure) and long-term repair of DNA damage caused by α- and β^--emitters?

Thorough comparison of biological effectiveness and characteristics of α- and β^--emitters in regards to DNA damage is crucial for tailoring TRT to individual patient needs. Notably, it is crucial to gain a deeper understanding of the repair mechanisms following TRT, as they may differ significantly from those observed after EBRT. In particular, in TRT DNA damage induction and repair occur concurrently due to the continuous decay of radionuclides, which can lead to a complex biological response. To facilitate repair, cells must unwind their densely packed chromatin, which makes them more vulnerable to further DNA damage by the next emitted particle. This presents a unique challenge to cellular repair pathways and may result in increased frequency of clustered DNA damage or misrepair, potentially leading to distinctly different biological outcomes compared to EBRT. Moreover, the high linear energy transfer (LET) of α-emitters versus the lower LET of β^--emitters likely results in qualitatively different DNA damage structures - such as more complex double-strand breaks - that may engage distinct repair pathways or differ in repair efficiency. While direct DNA damage responses to TRT have been more frequently studied, fewer investigations have focused on the long-term dynamics of DNA repair following exposure to TRT. This underscores the need for more comprehensive studies that specifically examine the differences in long-term repair processes between α- and β^--emitters, alongside comparative analyses with the gold standard of EBRT, to better understand where and how these treatment modalities differ in their biological responses. Understanding these differences in both the induction (e.g., size, complexity, spatial distribution) and long-term repair of DNA lesions is vital not only for elucidating the biological effects of various emitters but also for identifying optimal combination therapies that can radiosensitize or inhibit DNA repair to overcome radioresistance [11].

Q4 Can combination therapy with a DNA repair inhibitor improve treatment outcomes by enhancing efficacy, reducing required activities, and potentially overcoming radioresistance?

Despite the efficacy of [^{177}Lu]Lu-PSMA-617 as a therapeutic agent for mCRPC, approximately 30% of patients develop resistance to this treatment [12]. In such cases, an alternative approach involves switching to the α-emitting [^{225}Ac]Ac-PSMA-617 or employing a tandem therapy that combines both radiopharmaceuticals [13]. Unfortunately, radioresistance to α-radiation has also been reported. In a cohort of 60 patients treated with [^{225}Ac]Ac-PSMA-617, 37% exhibited a poor therapeutic response despite high PSMA expression in their tumors. Next-generation sequencing of biopsies from these non-responsive patients revealed mutations in genes involved in DNA damage repair and checkpoint pathways [14], suggesting that deficiencies or alterations in these critical mechanisms may allow tumor cells to survive despite high radiation-induced DNA damage. Therefore, combining TαT with agents that specifically inhibit DNA damage response proteins or repair pathways may be an effective strategy for overcoming the reported radioresistance. However, since TRT - and particularly TαT - are relatively recent therapeutic modalities, there remains a significant gap in understanding the detailed mechanisms underlying tumor response and resistance. Additionally, DNA repair inhibitors such as poly ADP-ribosylation inhibitor (PARPi) and DNA-PK inhibitor (DNA-PKi) have only recently emerged as novel treatment options, and their interplay with other therapies, including TRT, is not yet well understood or extensively studied. Consequently, results from combination therapy studies targeting DNA damage response pathways alongside TRT remain limited. This highlights the urgent need for more comprehensive *in vitro* investigations to elucidate the biological interactions between TRT and DNA repair inhibitors, which will be critical for optimizing combination treatment strategies.

1.3 Outline

This thesis is structured as follows: The next Chapter 2 focuses on introducing the fundamental principles relevant in the scope of this work. Given that TRT is an interdisciplinary research field, this chapter covers both biomedical principles (Section 2.1), including cell biology and cancer development, as well as physical

principles (Section 2.2). The latter encompasses an overview of radioactive decay, properties of various radionuclides, and key concepts underlying DNA damage induction by different types of radiation. The last Section 2.3 in this Chapter focuses on basic principles of TRT. In the following Chapter 3, a comprehensive overview of the current state of TRT is provided, focusing on the newest developments as well as recent pre- and clinical outcomes.
Methods and Experimental Design are explained in detail in Chapter 4. The sections represent the three main studies, DNA damage induction and repair (Section 4.1), absorbed dose simulation (Section 4.2), and cell proliferation after mono- or combination therapy of TRT (Section 4.3). Each section follows a uniform structure, mirroring the experimental procedure to facilitate reproduction of the studies. The sections begin with a brief introduction outlining the rationale and experimental design, followed by a detailed protocol describing cell culture procedures, compounds, and specific treatments used. After the detailed protocol, the analysis procedure is explained.
The results are presented in Chapter 5 and discussed in the subsequent Chapter 6. The structure of this chapter aligns with the four research questions introduced in Section 1.2. The study results of DNA damage induction are incorporated in Subsection 5.1 and 5.3. Subsection 5.2 describes the development of a simulation framework determining the absorbed dose, while Subsection 5.4 presents the results of the combination therapy of TRT with a DNA repair inhibiting DNA-PKi Nedisertib® (Merck, Darmstadt, Germany).
Finally, Chapter 7 summarizes the main findings and evaluates their impact. This is complemented by an outlook on future developments in TRT and rational design for further studies.

2 Fundamentals

In this chapter, the necessary knowledge to understand the performed experiments and results is provided. The first Section 2.1 focuses on the relevant biological mechanisms and processes in radiobiology, including DNA structure as well as induction and repair of DNA damage. This is followed by an introduction to the basic principles of carcinogenesis, which are important for understanding the vulnerabilities of cancer therapies and the challenges they face. The next Section 2.2 summarizes fundamental physical principles relevant in the scope of this work. Radioactive decay and physical properties of α- and β^--emitters are outlined, followed by DNA damage induction of various radiation types. Section 2.3 gives a brief overview of TRT, with a short excursion into radiochemical principles and description of the used PSMA-targeting compound.

2.1 Biomedical Principles

Understanding the effects of irradiation on human cells requires basic knowledge of cell composition, cell cycle and DNA. Starting with the concept of cells in general, important features of an animal cell are explained. Detailed descriptions of topics relevant to this work, including DNA structure and cell proliferation, follow. Afterwards, an overview of the classification of DNA damages and repair processes is given. The development of cancer and its hallmarks are specified. These are crucial to understanding the challenges cancer therapy faces.

2.1.1 Biological Cell Structure and DNA Damage Repair

Biological Structure of an Eukaryotic Cell

A living organism is defined to have the following capabilities: reproduction, growth, and development, and exchange of energy and matter with its environment [15]. A cell is the smallest unit that fulfills all these requirements. One distinguishes prokaryotes and eukaryotes. Eukaryote cells organize their DNA into a membrane-bound nucleus and contain membrane-bound organelles such as mitochondria, while in prokaryotic cells the DNA lies unpackaged in the cytoplasm. Prokaryotes are usually single-cell organisms like Escherichia coli (E. coli). Eukaryotes are the basis for all multicellular organisms as fungi, plants, and animals.
To understand the effects of TRT, the typical structure of a human (animal) cell is the relevant model. In Figure 2.1, the schematic cross-section of such a cell is shown. Two of the most important targets in cancer therapy are the nucleus, which contains DNA, and the mitochondria, which act as a cellular power plant. These can be targeted specifically to cause fatal damage and cell death.

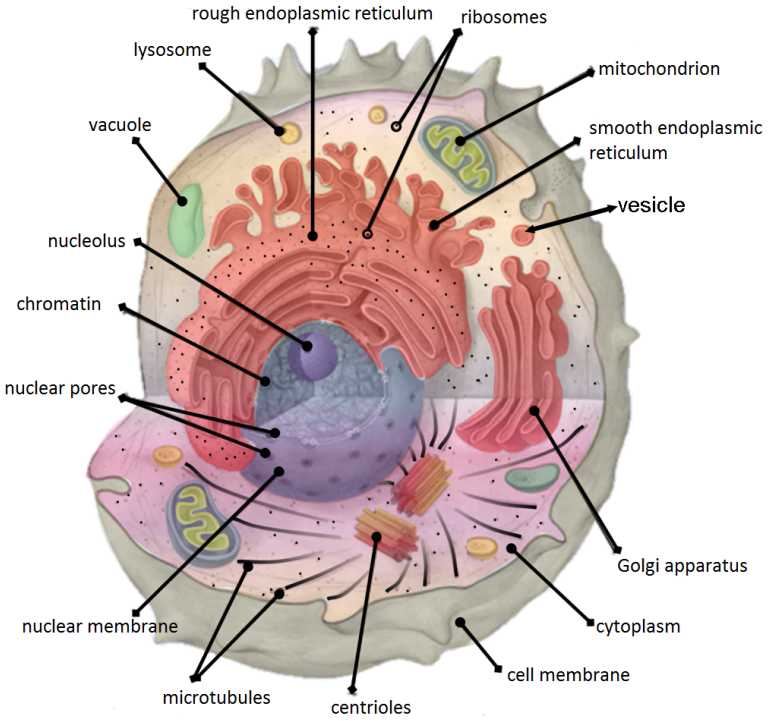

Figure 2.1: **Structure of a eukaryotic cell:** a cell with a nucleus and various cell organelles is shown. The cell nucleus, which packages and organizes DNA, is the characteristic feature of a eukaryotic cell. Illustration acquired from Bingbongboing, CC BY-SA 4.0, http://creativecommons.org/licenses/by/4.0/, via Wikimedia Commons [16]

The cell membrane acts as a barrier separating the interior of the cell from the external environment. It regulates the movement of substances into and out of the cell and plays a key role in various cellular functions, including cell adhesion and signaling. Inside, the cell is filled with cytoplasm that surrounds numerous organelles as well as the nucleus. Mitochondria are important membrane-covered cell organelles responsible for cellular respiration and energy production.
The nucleus is defined by the nuclear membrane, which isolates its contents from the cellular cytoplasm and regulates the traffic of proteins and other molecules through nuclear pores. In the nucleus, the DNA is organized as chromatin.

Cell Proliferation and Cell Cycle

Each cell originates from another preexisting cell. The cell cycle is the process that regulates this continuous iteration of duplication and cell division. Cell proliferation requires both cell division and growth, happening at the same time, leading to an increasing population of cells with a constant average size. In cancer cells, cell proliferation is often uncontrolled, or the proliferation rate is increased compared to normal cells. If a cell population has experienced severe damage, cell proliferation is slowed down or stopped due to arrest in the cell cycle or loss of cells by cell death.
The fundamental principle in the cell cycle is the replication of the DNA, which has to be error-free to guarantee a fully functional cell and avoid lethal mutations or degeneration leading to tumorigenesis. Therefore, the cell cycle is organized in different stages interrupted by various checkpoints to ensure that everything works properly. Generally, the cell cycle is split into four different successive phases: G_1 (Gap 1), S (synthesis phase), G_2 (Gap 2), and M (mitotic phase) illustrated in Figure 2.2.
The cell spends most of its time in the interphase, which consists of G_1, S and G_2. In this stage, the cell increases in size, duplicates its chromosomes, and gets ready to divide. Following interphase, the cell proceeds through mitosis and finishes division by splitting into two genetically identical daughter cells. Each daughter cell then enters interphase, starting a new cycle.
The duplication of the DNA takes place in the S-phase (DNA Synthesis) where each chromosome is replicated. At the beginning of mitosis, these intertwined pairs of identical chromosomes are condensed to sister chromatids in the characteristic shape (compare drawing in the circle right to the “M” in Figure 2.2). These sister chromatids are pulled apart later on in the mitosis by the mitotic spindle (next

circle following). Finally, the two DNA copies are packed into two nuclei, which is the end of mitosis. The final step of the M phase is then cytokinesis, where the cell divides into two identical daughter cells, each containing a nucleus and a set of duplicated cell organelles such as mitochondria. [15]

G_1 and G_2 serve two purposes. Firstly, they are known as "gap phases" because they allow cells to grow and prepare for the next cell division, which requires a certain amount of time. Secondly, during these phases, the cell assesses whether the internal and external environmental conditions are suitable for proceeding with the next cell division.

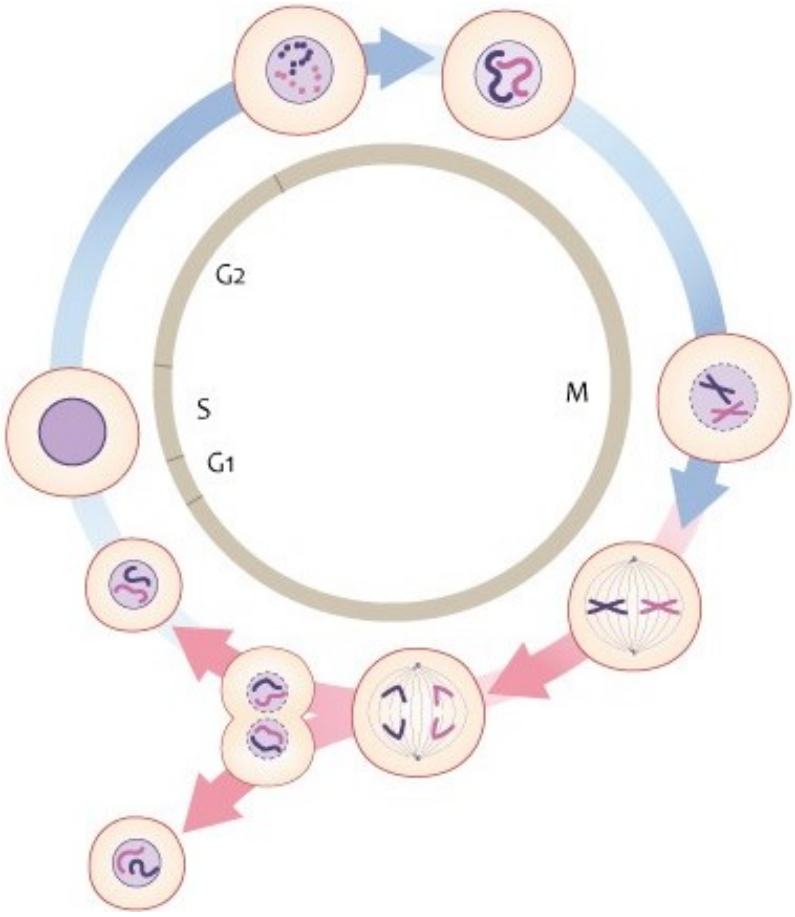

Figure 2.2: **Cell cycle:** the cell cycle is divided into four distinct, consecutive phases, G_1, S, G_2, and M. Most of the time the cell spends in interphase (G_1, S, G_2). During the M phase, the cell undergoes mitosis (separation of the duplicated DNA into two identical copies) and cytokinesis (splitting into two daughter cells). Illustration acquired from Genomics Education Programme, CC BY 2.0, https://creativecommons.org/licenses/by/2.0, via Wikimedia Commons [17]

DNA Structure and Organization

The DNA (Deoxyribonucleic acid) is the molecule that contains the genetic instructions necessary for the reproduction, growth, development, and function of cells. As such, maintaining the integrity of DNA is crucial for cellular health and proper functioning. Damage to DNA can have severe consequences, including cell death. Therefore, DNA is the primary target of radiotherapy, which aims to exploit this vulnerability by inducing DNA damage in cancer cells while minimizing harm to healthy tissues.

The structure of the DNA was decrypted by Watson and Crick in 1953 [18]. They were the first to propose a structure with two helical chains coiled around the same axis, forming a right-handed double helix. The two DNA strands are known as polynucleotides, as they are made up of simple monomeric units called nucleotides. Central for their conclusions were the X-ray diffraction photographs of DNA that Rosalind Franklin performed [19].

Each nucleotide is composed of one of four nitrogen-containing nucleobases (cytosine [C], guanine [G], adenine [A], and thymine [T]), the sugar deoxyribose, and a phosphate group. The deoxyribose is the backbone of the chain on the outside of the helix. The nucleobases located inside the double helix are responsible for the binding of the two chains. As only specific base pairs can bond together (AT and GC), the sequence of one strand defines the sequence of the other strand, which is helpful when it comes to damage repair. The sequence of the bases encodes the genetic information.

The human genome consists of 46 chromosomes. Of these, 44 chromosomes exist as pairs of homologous chromosomes, i.e., two copies of the same chromosome, one inherited from the mother and one from the father. These are called autosomes. The last two chromosomes are heterosomes X and Y, which determine gender.

A chromosome is a linear DNA double helix with a specific base sequence containing various genes. Genes are shorter base sequence segments that encode one specific protein, a set of protein variants, or an RNA molecule that fulfills an important role for the cell. Proteins have multiple functions essential for cell survival. They catalyze reactions, serve as signal receptors or motors, and thereby control central processes, e.g. DNA repair. The process by which RNA molecules are made using the base sequence of the specific gene is called transcription. The synthesis of a protein using an RNA molecule is called translation. In addition to genes, DNA also contains non-coding regions and regions that regulate gene tran-

scription.
In total, all chromosomes together would result in a chain of 2 m length if stretched out and strung together. The typical nucleus has a diameter of 6 µm. Hence, the nuclear DNA needs to be organized tightly to fit into this small volume. [15]

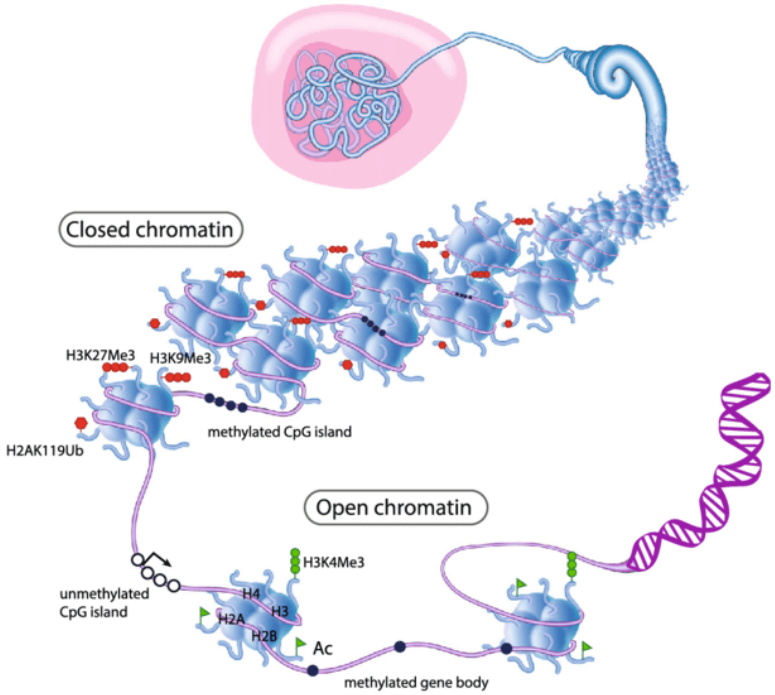

Figure 2.3: **From DNA to chromatin:** the DNA strand is wound around the histone octamer, forming a complex called nucleosomes. The nucleosomes are organized either in open, loosely arranged chromatin (euchromatin) or closed, densely packed chromatin (heterochromatin). Illustration acquired from Holliday et al. Breast Cancer Research (2018), CC BY-SA 4.0, http://creativecommons.org/licenses/by/4.0/ [20]

The nucleosome represents the primary unit of DNA packaging and consists of the DNA double helix wrapped approximately 1.7 times around a histone octamer core. This octamer is composed of two copies each of the histones H2A, H2B, H3, and H4, as illustrated in Figure 2.3. By arranging DNA into nucleosomes, its length is compacted to about one-third of the original.
Furthermore, the ensemble of nucleosomes and non-histone proteins that are attached to the DNA is referred to as chromatin. This is the next step in DNA compaction. Two different organizational forms are distinguished. The higher compacted form of the chromatin is called heterochromatin (HC), and the less compact one is euchromatin (EC). Open chromatin regions (EC) facilitate gene transcription and are identified by active histone modifications such as H3K4Me3 and

widespread histone acetylation (see Figure 2.3). In contrast, the remaining DNA is organized into inactive heterochromatin, which frequently includes repetitive sequences. This form of chromatin is marked by repressive histone modifications like H3K27Me3, H3K9Me3, and H2AK119Ub.[15]

DNA Damages and Repair Processes

Every second, our DNA is exposed to various endogenous and exogenous stressors, including metabolic byproducts, ultraviolet light from the sun, and background ionizing radiation, all of which can induce molecular damage to the DNA.
A basic distinction is made between damage that is due to a change in one or more bases of DNA and is caused by hydrolysis or oxidation, and damage that is known as strand breaks. The first type often occurs spontaneously due to heat, metabolic imbalance, external factors (e.g. UV, radiation, chemicals), or errors during replication. For the most part, it can be repaired easily and quickly using various mechanisms. Hereby, the complementary arrangement of bases at both DNA strands facilitates the detection and repair of damage.
Breaks of the whole DNA strand, however, are more challenging for the DNA repair machinery. Single strand breaks (SSB) are usually easier to repair because the other intact strand can be used as a blueprint. Double strand breaks (DSB) are the most difficult to repair and can lead to cell death or malignant mutation if not repaired correctly.
Therefore, the induction of many DSBs is crucial for the aim of cancer therapy, which is the eradication of all malignant cells. The ability of cells to repair such damage plays a critical role, as cancer cells often have impaired repair mechanisms due to deficiencies in specific pathways. However, this does not always provide a clear advantage for healthy cells with intact repair mechanisms. In some cases, cancer cells can adapt by upregulating alternative, faster repair pathways, which enables them to efficiently repair DNA damage despite an increased risk of mutations. Furthermore, many cancer cells have faulty control mechanisms that allow them to bypass normal cell cycle checkpoints and continue proliferating even in the presence of DSBs. [15]
To detect DSBs in experiments with (living) cells, γH2AX, the phosphorylated form of histone H2AX, is often used as a confident marker. As explained in section 2.1.1, DNA is wrapped around a core histone molecule composed of the individual histone proteins H2A, H2B, H3, and H4. Accounting for 10% of total H2A in human cells, H2AX is a variant of the H2A protein.

In the presence of DNA damage, this molecule is phosphorylated at the 139th serine, and this phosphorylation is referred to as γH2AX. Per DSB hundreds to thousands of H2AX are phosphorylated within minutes. Labeling with γH2AX is the first step in locating DNA damage and signals the cell machinery to recruit the necessary repair proteins. Hence, it is a perfect biomarker to quantify early DSBs and observe the kinetics of the repair process as it is dephosphorylated after a successful repair. [21, 22]

To repair DSBs, mainly two repair pathways are applied in eukaryotic cells, the non homologous end-joining (NHEJ) and the homologous recombination (HR). Both pathways have their advantages and disadvantages, and while several key factors influencing pathway choice are understood, the full decision-making process remains complex and not entirely resolved. The choice between DNA repair pathways is influenced by factors such as the cell cycle phase, DNA damage complexity, and chromatin context, with NHEJ dominating in G_1 and HR favored in S/G_2 phases [23, 24].

On the one side, HR leads to accurate repair because it can reconstruct lost sequences by copying the sister chromatid. To fulfill the repair, a sequence homologous to the sequence of the damaged area has to be searched on the copied DNA template. Once found, the missing DNA sequence is synthesized and inserted at the damage to restore the DNA [25]. Hence, HR is only applicable during the late S and G_2 where a complete copy of the DNA is available. This is also the reason for higher radioresistance in cells during these stages of the cell cycle [26, 27].

On the other hand, NHEJ with only 0.5 h repair time is the faster repair path compared to 7 h and more for HR. On the downside, NHEJ is intrinsically mutagenic. While HR uses the intact copy of the damaged DNA as a template, NHEJ modifies the broken DNA ends and ligates them together without respecting homology and thereby generates deletions or insertions. As depicted in Figure 2.4, the damaged site is recognized by the recruitment of the KU heterodimer complex (KU70 and KU80). The site is then stabilized by the DNA-dependent protein kinase catalytic subunit (DNA-PKcs). Together, the KU heterodimer and the DNA-PKcs form the DNA-dependent protein kinase (DNA-PK) complex. Then the DNA ends are processed further by additional enzymes and rejoined [28, 29].

Therefore, inhibitors of DNA-PK are used to sensitize cells for radiation-induced DNA damage. By blocking the ATP-binding site of DNA-PKcs, the kinase activity is inhibited and the recruitment of further repair proteins is stopped. Using a DNA-PK inhibitor together with a DNA damage-inducing agent such as radiation

can prevent the repair of induced DSBs and lead to accumulation of DSBs [30]. An example of a tested DNA-PK inhibitor is M3814, which has proven to work effectively when combined with external radiation [31].

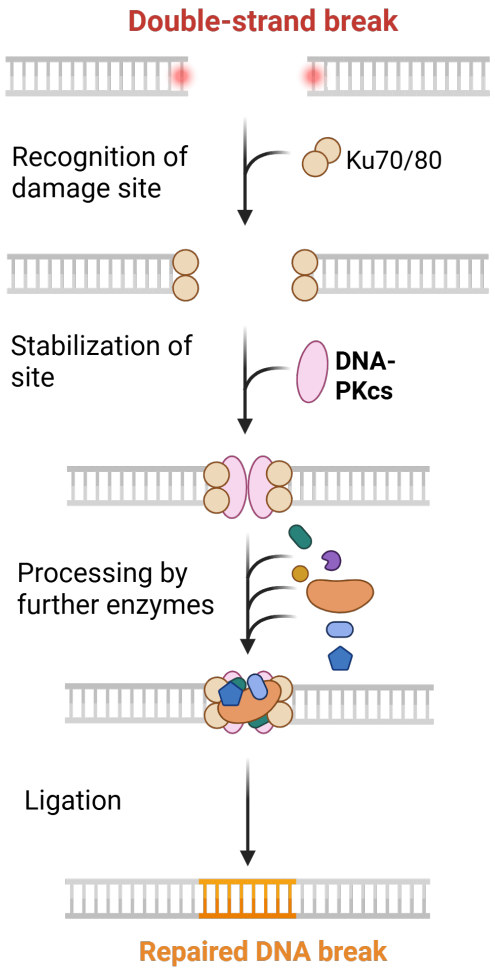

Figure 2.4: **Role of DNA-PK in NHEJ:** the DNA-dependent protein kinase complex formed from the KU heterodimer and the catalytic subunit of DNA-dependent protein kinase is essential for the repair of DSB via NHEJ, as it helps stabilize the site of damage and recruit more enzymes for the repair process [28]. Created in Biorender `https://BioRender.com` and adapted from template BioRender (2025) [32]

2.1.2 Cancer Development and Hallmarks

Carcinogenesis

Defective repair of DNA damage can lead to mutations in the genome of the cell. If these mutations do not affect important genes, the cell may continue its cell cycle without restriction. If the mutations are of significance, this can either result in programmed cell death (apoptosis) or cancer.
Cancer is defined as uncontrolled growth by cell division and not restricted by environmental conditions (e.g., if there is space or need for new cells) [33]. These cancerous cells can form a lump of tissue, commonly called a tumor. Malignant cancer is further characterized by its ability to metastasize, that is, to invade surrounding tissues and travel to distant places in the body from its origin to form new tumors. If left untreated, cancer can invade the entire body and become a life-threatening disease if it destroys the tissues and organs necessary for the organism to survive.

Hallmarks of Cancer

In 2000, the concept of hallmarks of cancer, defining biological capabilities that tumors develop over time, was introduced. Since then, the six hallmarks which were described first have been expanded to ten, depicted in Figure 2.5. Structuring tumor development into these hallmarks has tremendously helped the understanding of carcinogenesis and especially the mechanisms which lead to highly aggressive, metastatic, and treatment-resistant forms of cancer.[34, 35]
The ten hallmarks are: sustaining proliferative signaling (1), evading growth suppressors (2), activating invasion and metastasis (3), enabling replicative immortality (4), inducing or accessing vasculature (5), resisting cell death (6), avoiding immune destruction (7), deregulating cellular metabolism (8), tumor-promoting inflammation (9) and genome instability and mutation (10). Hallmark 1-8 are functional capabilities, enabling survival, proliferation, and dissemination of cancer cells. Obtainment of these capabilities is promoted by the two enabling characteristics, 9 and 10. Most of these hallmarks challenge cancer treatments as they can lead to evasion of treatment or resistance, whereas others make the tumor more vulnerable and encourage the development of new treatments. [35]

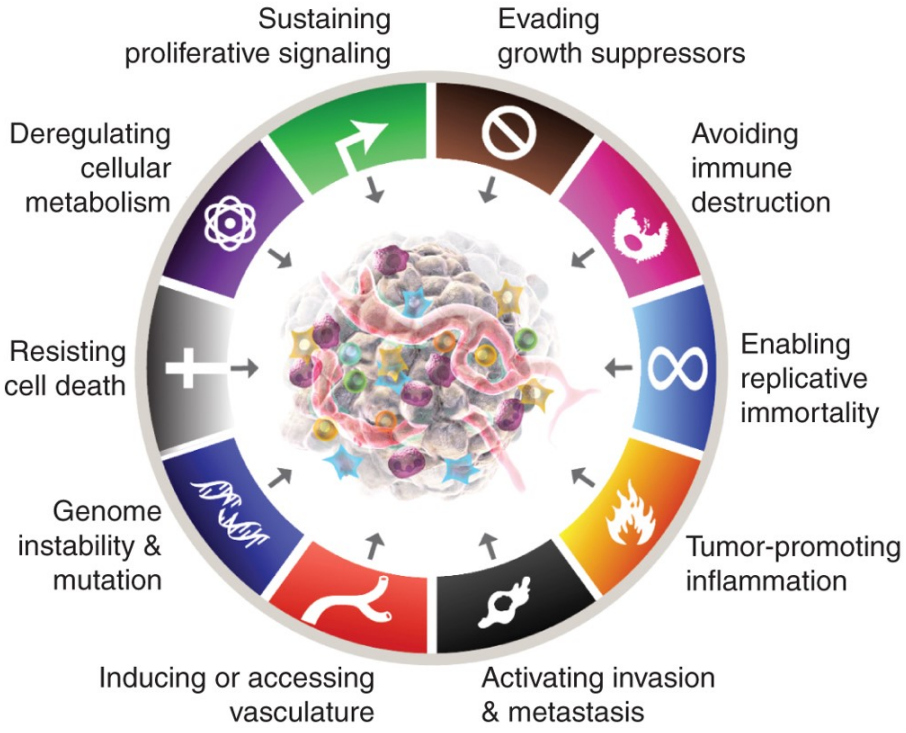

Figure 2.5: **Hallmarks of Cancer:** these features of cancer first described in [36] have helped to better understand cancer, to study and link certain mechanisms. Figure acquired with permission from [35], licence number 6096380886912

Promoting tumor invasion and metastasis can also lead to overexpression of certain antigens compared to normal tissue. This overexpression can then be used as a target to detect and monitor disease status and, more importantly, deliver treatment specifically to the tumor. This is exactly what targeted radionuclide therapy is aiming for. Specifically for prostate cancer, an overexpression of the prostate-specific membrane antigen (PSMA) was discovered and associated with poor prognosis and higher risk of biochemical recurrence [37]. Unfortunately, the biological function of PSMA is not yet fully understood. Studies suggest that PSMA plays a multifunctional role and is involved in cell survival, proliferation and migration [38, 39]. Its overexpression and association with aggressive disease stage make PSMA a suitable target for TRT.

Additionally, TRT is using the up-regulated formation of new blood vessels (angiogenensis) to deliver the radiopharmaceuticals effectively. As systematic therapy, it can also tackle metastasized diseases and α-emitters can even overcome hypoxia induced by deregulation of cellular metabolism.

2.2 Physical Principles

In this section, physical principles relevant for TRT are introduced. Starting with a description of the radioactive decay and continuing with characteristic properties of α- and β^--emitters. Afterwards, the DNA damage induction of various radiation types (α, β^- and external photon irradiation) is outlined and differences are emphasized.

2.2.1 Radioactive Decay and Physical Properties of α and β^--Emitters

Radioactivity

The phenomenon of radioactivity was discovered and explored by three pioneers, Henri Becquerel and Marie and Pierre Curie in 1896 [40–42]. They observed that some elements emit radiation spontaneously without any external stimulation. At that time it was Marie Curie who called the new phenomenon „radioactivity“. After several experiments, they concluded that different elements emit different types of radiation. Two types were deflected in a magnetic field, thus charged, whereas the third was not deflected at all and had to be neutral. They likewise observed that the rays had different properties in penetration.
Sir Ernest Rutherford then coined the terms “alpha (α)” and “beta (β)” rays for the two types of charged rays. α-rays were described to be positively charged, highly ionizing, and easily absorbed. Contrarily, β-rays carry a negative charge, are easily deflected by a moderate magnetic field, and have a greater penetration than α-rays [43–45].
Paul Ulrich Villard then studied the third type of rays more extensively, which were characterized as non-deviable and extremely penetrating [46, 47]. This third type was named “gamma (γ)” rays.
Nowadays, the three types of radiation (α, β, and γ) emitted through radioactive decay are still referred to these early classifications, but more detailed knowledge about the origin of radioactivity was acquired. While the aforementioned pioneers were able to study the nature of the various radiation emitted by radioactive elements, they were unable to find out why this radiation is emitted. Therefore, it is necessary to understand the structure of the atom. With the discovery of the neutron by James Chadwick, the following structure of the atom was proposed:

an atom consists of a nucleus, built up from protons and neutrons, surrounded by a cloud of electrons [48].
Furthermore, when discussing radiotherapy, the discover of the X-rays by Wilhelm Conrad Röntgen in 1895 should not be forgotten [49]. Like γ-rays, X-rays are classified as electromagnetic radiation, characterized by photons. The origin of the photon could be either the from an atomic nucleus undergoing a γ-decay, hence γ-ray, or from an energy differences during a transition in the electron shell or slow down of charged particles like electrons, referred to as X-rays.

Every atom is defined by the mass number A, which is the sum of protons and neutrons in the nucleus (nucleons), and the atomic number Z, which is the number of protons (and as well electrons). Atoms with equal Z but different A belong to the same chemical element and are called isotopes. They differ in the number of neutrons ($N = A - Z$) in the nucleus. However, the stability of the nucleus depends on the ratio of protons and neutrons as well as on the total number of nucleons. Low atomic number nuclei are stable with a ratio of neutrons/protons close to 1, while for higher atomic number nuclei, a ratio < 1 is favored. The line of stable isotopes is depicted in the nuclide chart in Figure 2.6. If the isotope is unstable, it can rearrange its number of protons and neutrons to a more favorable, less energetic (stable) state by emission of particles (e.g. α, e^-), emitting a γ-quant (photon) or fission of the whole nucleus. The first two processes involve the emission of ionizing radiation, particles or electromagnetic waves whose energy is large enough to detach electrons from atoms or molecules, thereby putting them in a charged, ionized state. This ionizing radiation is often referred to "radioactive radiation" and nuclei that undergo this process are called radionuclides. In this thesis, the focus lies on the α- and β^--decay modes, as these are the prominent decay modes of the used radionuclides. They will be explained in the next paragraph. [50, 51]

Radioactive Decay

The α-decay takes typically place in heavy isotopes with $Z > 52$. When a nucleus undergoes an α-decay, it will emit an α-particle, consisting of two neutrons and two protons (charge +2), essentially the nucleus of a helium atom. This is described technically in Equation 2.1. The element resulting from the decay, also called daughter, has then an atomic number $Z - 2$ and a mass number $A - 4$.

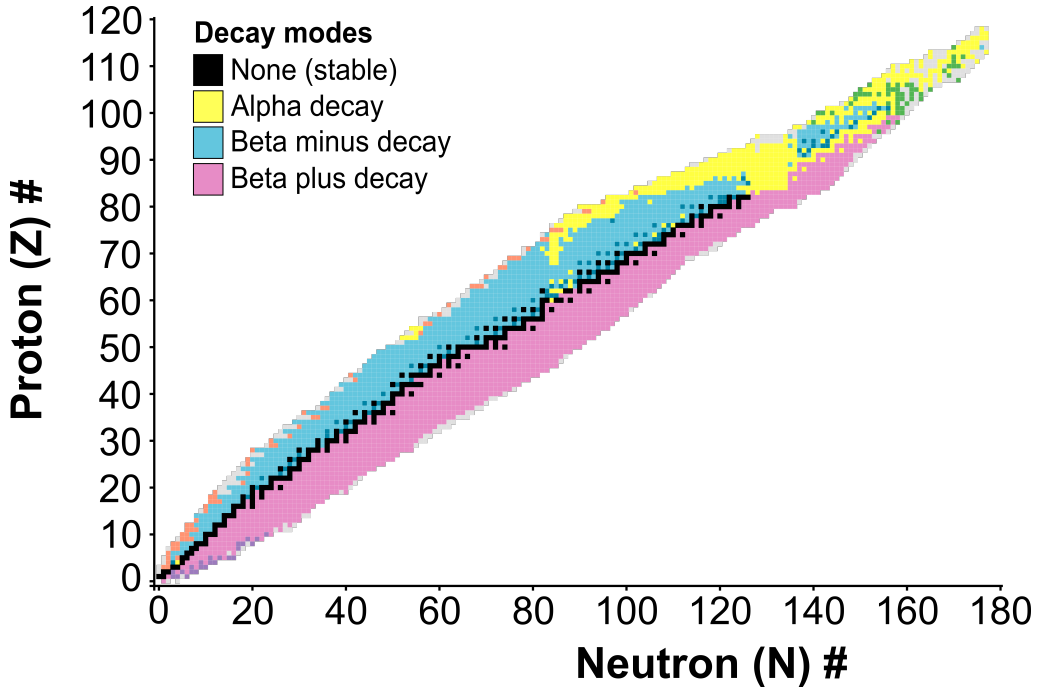

Figure 2.6: **Nuclide chart:** stable isotopes are represented by black color, isotopes with undergo α-decay in yellow, and β^--decay in blue. Only decay modes that are relevant in the scope of this thesis are included in the legend. The figure was created using data from NuDat 3. National Nuclear Data Center, information extracted from the NuDat database, https://www.nndc.bnl.gov/nudat/ [52]

If the daughter nucleus is again unstable, it would undergo further radioactive decay until it has decayed to a stable state. Especially heavy radioisotopes often undergo a decay chain with multiple α-decays. These are interesting candidates for therapeutic treatment, as the biological effectiveness increases with multiple α-particles. [53, 54]

Alpha decay: $${}^{A}_{Z}\mathrm{X}^{N} \rightarrow {}^{A-4}_{Z-2}\mathrm{Y}^{N-2} + \alpha \qquad \text{with} \qquad \alpha = {}^{4}_{2}\mathrm{He} \tag{2.1}$$

For β-decay, two modes can be distinguished, β^- and β^+. The β-decay is generally characterized by a transformation of a nucleon. Thus, in neutron-rich nuclei, a neutron is transformed into a proton (β^+-decay), and in proton-rich nuclei, a proton is transformed into a neutron (β^--decay). Hence, the β-decay is characterized by a stable mass number A, while Z and N gain or decrease one number, depending on the specific decay mode. When a proton decays into a neutron, charge and energy must be conserved during this reaction. Therefore, a particle with opposite charge of the proton, an electron, is emitted together with an antineutrino $\bar{\nu}_e$.

The antineutrino is a particle with almost mass zero and neutral charge, which is needed for the energy conservation in the reaction. Because the particle emitted during this radioactive decay is negatively charged, the decay was called β^- (refer to Equation 2.2). [53, 54]

Beta minus decay: $${}^{A}_{Z}\mathrm{X}^{N} \rightarrow {}^{A}_{Z+1}\mathrm{Y}^{N-1} + \mathrm{e}^- + \bar{\nu}_e \qquad \text{with} \qquad \mathrm{n}^0 \rightarrow \mathrm{p}^+ + \mathrm{e}^- + \bar{\nu}_e \tag{2.2}$$

Contrarily, during the β^+-decay, a proton decays into a neutron. In this case, a charge equal to a proton is necessary on the product side for charge conservation. This is the β^+-particle, also known as positron e^+, which is the antiparticle of the electron. To conserve energy, a neutrino ν_e is emitted as well during this decay (refer to Equation 2.3). At the end of its track the e^+ is annihilated by recombination with an e^-, which creates two photons emitted at the energy of 512 keV in opposite directions of 180°. Positron-emission tomography (PET) uses this process to reconstruct images where the initial signal comes from radioisotopes undergoing β^+-decay. [53, 54]

Beta plus decay: $${}^{A}_{Z}\mathrm{X}^{N} \rightarrow {}^{A}_{Z-1}\mathrm{Y}^{N+1} + \mathrm{e}^+ + \nu_e \qquad \text{with} \qquad \mathrm{p}^+ \rightarrow \mathrm{n}^0 + \mathrm{e}^+ + \nu_e \tag{2.3}$$

In the following, some general laws and variables that describe radioactive decay and its properties are introduced. The radioactive decay is a spontaneous process that cannot be externally influenced, accelerated, or slowed down. As a result, it is impossible to predict exactly when a decay of a certain atom will occur. However, certain parameters define how a radioactive probe (a specific number of radioactive atoms) behaves over time. The decay constant λ, which is specific to each radionuclide, can be used to describe how the initial number of atoms N_0 at time zero ($t = 0$) decreases over time (refer Equation 2.4).

$$N(t) = N_0 \, exp(-\lambda t) \tag{2.4}$$

With $N(t)$, the activity $A(t)$ can be defined. The activity A describes the number of decays or emitted particles N per second (refer to Equation 2.5).

$$A(t) = \lambda \cdot N(t) = \lambda \cdot N_0 \, exp(-\lambda t) = A_0 \, exp(-\lambda t)$$
$$\text{unit: Becquerel} \quad [A] = 1\,\mathrm{Bq} = 1\,\mathrm{s}^{-1} \tag{2.5}$$

The next important quantity that can be extracted from Equation 2.4 is the half-life period $T_{1/2}$, which describes the time after which half of the initial number of radionuclides N_0 has decayed (refer to Equation 2.6) [51].

$$\begin{aligned} N(t) = T_{1/2} = N_0 exp(-\lambda T_{1/2}) = N_0/2 \qquad & | \, ln(\ ) \\ ln(exp(-\lambda T_{1/2}) = ln(1/2) \qquad & \\ -\lambda T_{1/2} = ln(1) - ln(2) = -ln(2) \qquad & | : -\lambda \\ T_{1/2} = \frac{ln(2)}{\lambda} \qquad & \end{aligned} \tag{2.6}$$

In Figure 2.7, the decay schemes of the α-emitting radionuclides, ^{225}Ac, ^{227}Th and ^{223}Ra, studied in this work are depicted. All three radionuclides undergo multiple α-decays until reaching a stable state. As ^{223}Ra is the daughter nuclide of ^{227}Th, the decay chain of ^{227}Th on the right side of the figure, represents both radionuclides. ^{223}Ra has always one α-decay less than ^{227}Th. Notably, there is a split in all decay chains, where one isotope can either undergo a β^--decay or an α-decay (^{213}Bi for ^{225}Ac and ^{211}Bi for ^{227}Th and ^{223}Ra). When calculating the cumulative α-energy of all α-particles emitted across the entire decay chain (refer to Table 2.1, this split is taken into account, leading to two values for the cumulative α-energy. However, as displayed in Figure 2.7, the probability for one decay chain is higher.

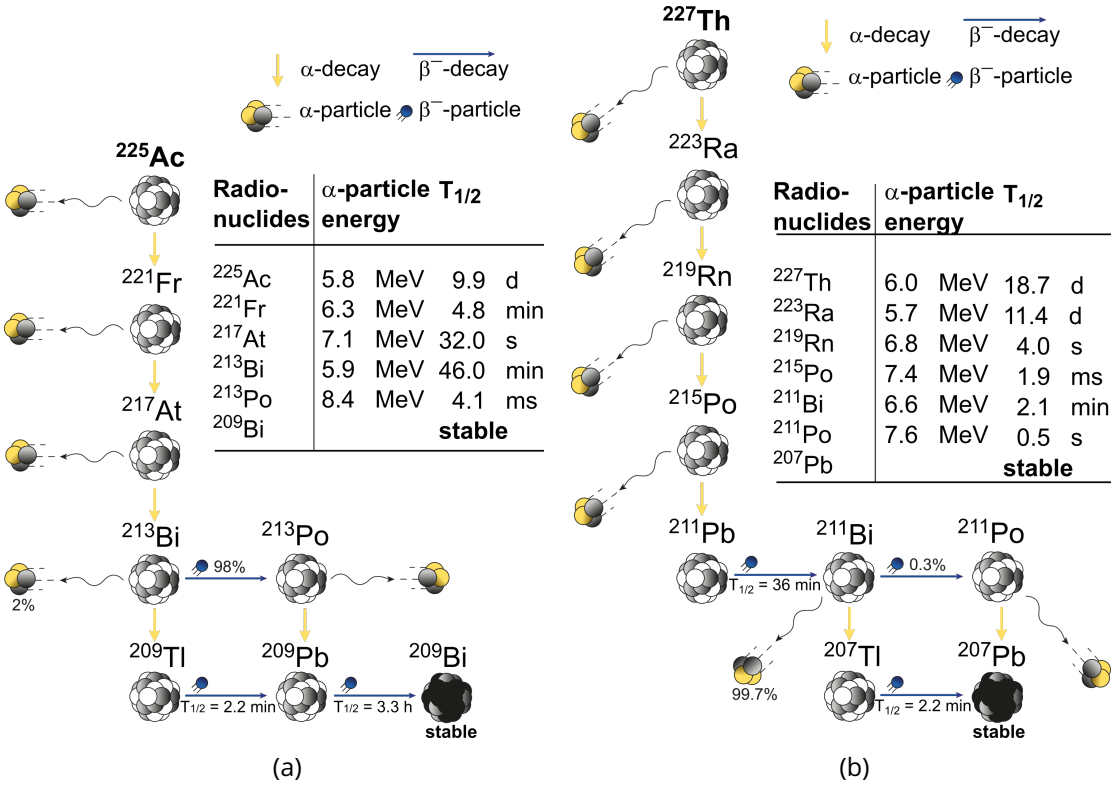

Figure 2.7: **Decay chain of ^{225}Ac and ^{227}Th:** the decay chain of the radionuclide ^{225}Ac is depicted on the left in (a) and decay chain of the radionuclide ^{227}Th with daughter nuclide ^{223}Ra on the right side in (b). Daughter nuclides, energies of α-particles and $T_{1/2}$ are specified for the individual decays. Figure acquired and adapted with permission from Roscher et al. Pharmaceuticals (2020), CC BY 4.0 https://creativecommons.org/licenses/by/4.0/ [55]

The decay scheme of the β^--emitter ^{177}Lu employed in this work can be seen in Figure 2.8. The isotope just undergoes one β^--decay until ending in a stable state. However, for this decay, multiple energy transitions for the decay are possible, resulting in different energies of the emitted β^--particle. The energy displayed in the Figure refers to the maximum energy which the β^--particle can have. The average energy for a β^--particle is given in Table 2.1.

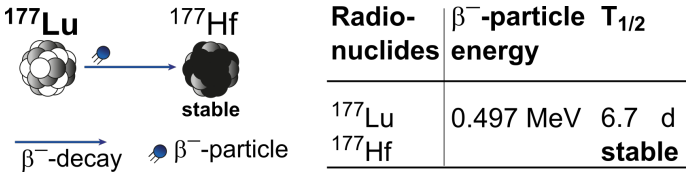

Figure 2.8: **Decay scheme of ^{177}Lu:** the β^--emitter ^{177}Lu decays directly to a stable isotope. Information of decay energies taken from the NuDat database [52].

Physical Properties of α and β^--Particles

The interactions with matter are quite distinct comparing α- and β^--particles, thus electrons e^-. When considering charged particle interaction with matter, an often-referred key quantity is the LET. The linear energy transfer is defined by the amount of energy deposited by ionizing radiation in matter. Its unit is energy per unit length, commonly expressed in keV/µm. The LET is strongly related to the biological effect of the particle.

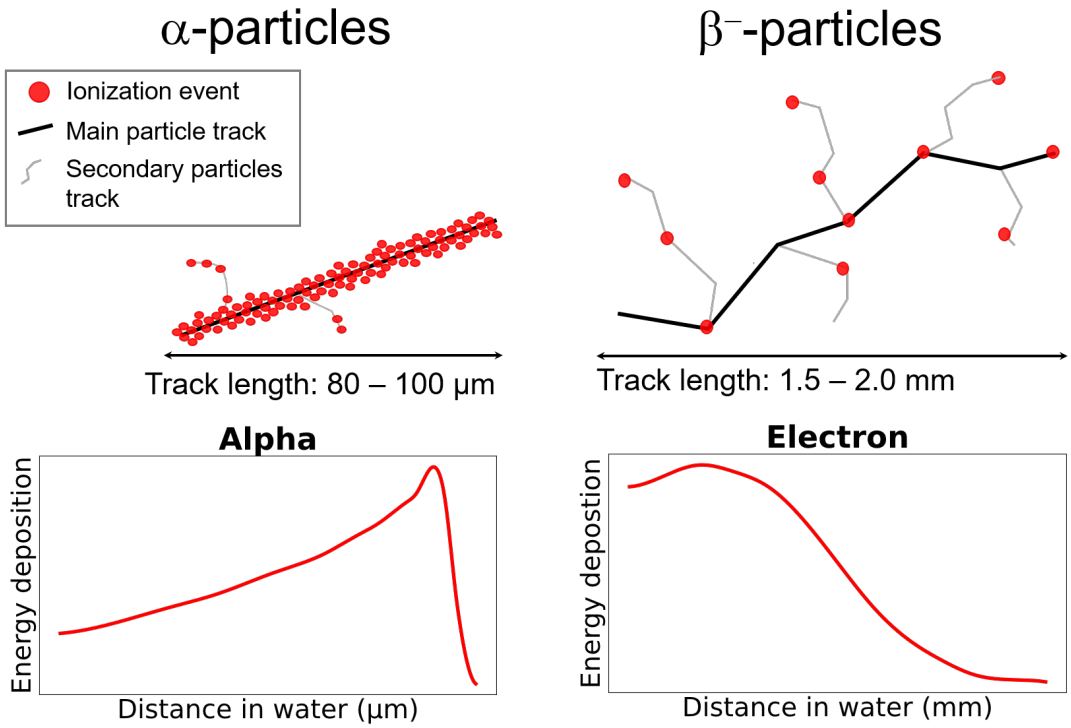

Figure 2.9: **Schematic track structure and energy deposition of α- and β^--particles:** α-particles have a straight, densely ionized track, and deposit most of their energy at the end of the track (Bragg peak). β^--particles are scattered during their interactions, and produce some secondary electrons (δ e^-) along their track. They deposit small amount of energy during each interaction and their path ends when the energy is decreased to zero. Path structures and energy deposition in water are only shown schematically to illustrate these processes.

Generally, a higher LET means denser ionization tracks, leading to more severe and complex DNA damage in cells, which is harder to repair, thus increasing the biological effect or damage. However, this relationship holds only up to a certain point. Experimental evidence shows that beyond an LET of approximately 200 keV/µm, the relative biological effectiveness actually decreases [56]. A phenomenon which is referred to as the "overkill effect," where the energy deposited

becomes so concentrated that additional energy does not translate into proportionally more biological damage. Furthermore, the biological effect at a given LET is also influenced by the type of particle. Additionally, the biological effect at a given LET depends also on the type of particle, since different particles can produce distinct track structures, and on the specific cell or tissue being irradiated, making the relative biological effectiveness a complex, system-dependent parameter [57].

Table 2.1: **Comparison of physical and biological properties of selected therapeutic radionuclides:** properties relevant for biological effectiveness like energy of emitted particle and LET are given, based on data from NuDat database [52]. For α-emitters, the cumulative α-energy is defined, which is the sum of the energy of all α-particles emitted across the decay chain. The mean α-energy is calculated by dividing by the number of α decays in the chain. Decay chain splits for ^{227}Th and ^{223}Ra at ^{211}Bi (^{227}Th: 5 α per chain, ^{223}Ra: 4 α per chain), and for ^{225}Ac at ^{213}Bi (^{225}Ac: 4 α per chain). The cumulative and mean α-energy with the larger probability are printed in bold. For details of decay chains refer to Figure 2.7 and 2.8.

	α-emitter			β^--emitter
Property	**^{227}Th**	**^{223}Ra**	**^{225}Ac**	**^{177}Lu**
Half-life [days]	18.7	11.4	9.9	6.6
Particle energy [MeV]	6.0	5.7	5.8	0.50 (max), 0.13 (avg)
# α-particles in decay chain	6 (5)	5 (4)	5 (4)	-
Cumulative α-energy [MeV]	**32.5**/33.5	**26.5**/27.5	25.1/**27.6**	-
Mean α-energy [MeV]	**6.5** / 6.7	**6.6**/6.7	6.3/**6.9**	-
Range in tissue [µm]	50–70	50–70	47–85	1500–1700
LET [keV µm^{-1}]	80–120	80–120	70–120	0.08–0.33
Hits for cell killing		~2-10		~2000

Electrons are negatively charged and very light. Therefore, an electron has a large number of small interactions along its track and its LET is low. During each interaction, only a small amount of energy is deposited, and the electron is easily scattered in these interactions. Due to these properties, the penetration depth of electrons in tissue (water) is in the range of a few millimeters. A typical track structure of an electron and its energy deposition is sketched in Figure 2.9.

α-particles carry a double positive charge and are quite heavy, compared to other ionizing radiation particles like electrons or protons. Their track is densely ionized, and most energy is deposited at the end of the track, when the α-particle has

slowed down enough for direct interaction (for illustration see Figure 2.9). Their LET is large, but their penetration depth in tissue is short, in the range of around 100 µm. [54]. Physical properties of the selected radionuclides are summarized in Table 2.1. In the scope of this thesis, β^--particles will be classified as long-range in comparison to α-particles. However, in a general setting, β^--particles would be considered as mid-range or even short-range compared to X-rays or γ-radiation which could exhibit ranges in tissue from 1 mm - 0.5 m strongly dependent on their energy [58].

2.2.2 DNA Damage Induction of Various Radiation Types

Absorbed Dose

When discussing the biological effects of ionizing radiation on biological tissues, the quantity of absorbed dose D_a is important to define. The D_a refers to the total of energy E absorbed during interactions of the ionizing radiation with atoms and molecules per unit mass m of the substance (refer to Equation 2.7). [54]

$$D_a = \frac{E}{m} = \frac{\text{Energy absorbed in volume}}{\text{Mass of volume}} \qquad (2.7)$$
$$\text{unit: Gray} \quad [D_a] = 1\,\text{Gy} = 1\,\text{J/kg} = 1\,\text{m}^2/\text{s}^2$$

Indirect and Direct DNA Damage Induction

In general, the processes that take place during radiation exposure can be divided into four stages: physical, physico-chemical, chemical, and biological stages. [54, 59, 60]

physical stage (10^{-16} s): water radiolysis, a process consisting of ionization ($H_2O \rightarrow (H_2O)^+ + e^-$) and excitation of water molecules (H_2O^*), is started as well as ionization of DNA macromolecules leading to direct DNA damage induction (SSBs and DSBs) (Figure 2.10b);

physico-chemical stage (1 µs): reactive oxygen species (ROS) formation, through reactions of free electrons, ionized and exited water molecules, such as charged ions ($(OH)^-$, H^+, $(H_3O)^+$, O_2^-), free radicals ($H^\bullet$, $HO^\bullet$) and hydroperoxide H_2O_2; ROS formation is highly dependent on the presence of oxygen O_2;

chemical stage (few seconds): ROS diffuse within the tissue, induce oxidative stress and interact with organic molecules; chemical alterations are induced leading to indirect DNA damage; at the end of the stage, first chemical reconstitution and repair of damages is started, while DNA damage is also fixated by oxygen, which impedes or even prevents its repair;

biological stage (several minutes - decades): short-term (approx. 72 h) repair of DNA damage and biological effects such as cell death occurs, provided the damage is fatal; in the long term, early biological effects of treatment such as regression or progression of the tumor as well as side effects in healthy tissue are evident; late biological effects due to radiation exposure can occur up to decades after treatment and include the occurrence of cancer.

The above-described processes occur upon every interaction of ionizing radiation with biological tissue. However, there are important differences between different types of ionizing radiation, mainly depending on their physical interaction with matter described in the paragraph above. A simplified summary of the prevalent mechanism is shown in Figure 2.10a
For β^--particles as well as external radiation consisting of photons with low ionizing potential, the DNA damage induction is prevalently mediated through the indirect mechanism of ROS production and their interaction with the DNA. Direct DNA damage by ionization of the DNA strand can also take place (as depicted in Figure 2.10b), however the amount of DNA damage induced by this mechanism is low compared to the indirect DNA damage induction (ratio of 30 : 70 for direct to indirect damage) [61, 62]. Furthermore, low LET radiation induces primarily SSBs rather than DSBs, which are more challenging to repair (ratio 10:1 of SSB : DSB for low LET γ-radiation) [63].

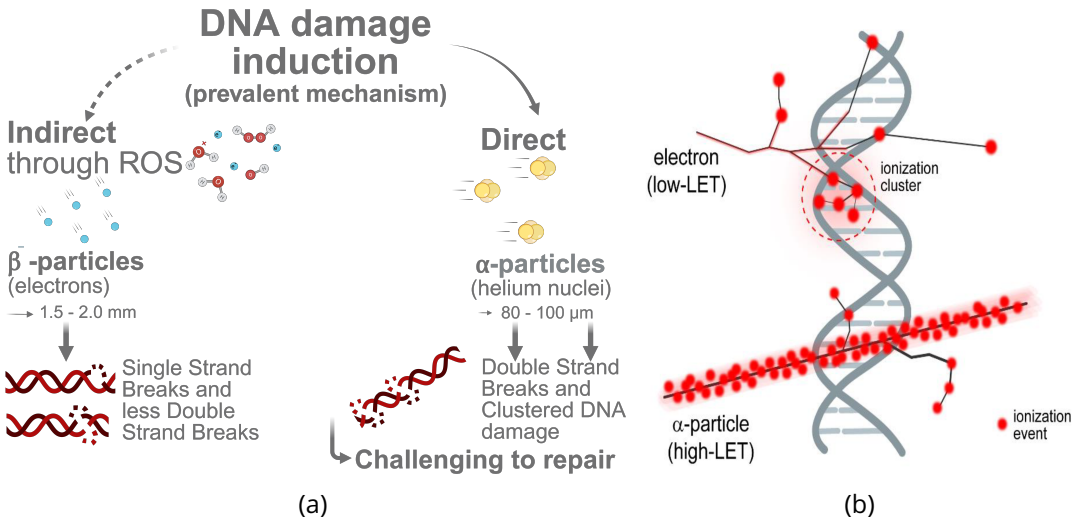

Figure 2.10: **DNA damage induction by α- and β^--particles:** prevalent mechanism (a) and comparison of direct DNA damage induction (b)
(a) Created in Biorender https://BioRender.com and (b) Figure acquired from Iliakis et al. Cancers (2019), CC BY 4.0 https://creativecommons.org/licenses/by/4.0/ [64]

In contrast, α-particles are considered as high LET radiation. Their main mechanism is direct DNA induction through collision with the DNA macromolecule. Indirect mediation of DNA damage through ROS is not of major importance. Although radical formation very close to the DNA damage site might even enhance the effect of the directly induced damage [65, 66]. Additionally, α-particles are prone to induce more DSBs than SSBs and even clustered DSB, which are more complex and challenging to repair. Studies concluded that even 61% of induced DSBs are complex [67]. Their range is dependent on their energy, but typically around one to few cell diameters for an energy between 1 MeV to 6 MeV [68, 69]. During a collision with a DNA molecule, most of the energy is deposited at this site, leading to complex DSB and energy deposition within the vicinity of critical structures. Studies show that contrary to β^--particles, α-particles of energy 5.5 MeV deposit 90% of their total energy in a sphere with only 500 µm [9]. Characteristic for DNA damage induced by α-particles is that the lesions induced by a single particle are spatially and temporally correlated along the narrow track of the particle [70]. The close proximity of multiple DSBs makes the repair even more challenging and error-prone. This track can also be visualized in microscopy by immunofluorescent staining of γH2AX or other DSB markers. On the downside, due to their short range in tissue, α-particles need to be close to the nucleus to induce lethal DNA damage. This is only possible with TRT.
Closing this paragraph, it is important to remark that the current knowledge about

DNA damage induction is mainly from experiments with EBRT. Treatment with external photon irradiation usually happens in a relatively short time ($\sim$ minutes), whereas radiation exposure in TRT occurs over several days, depending on the specific half-life of the applied radionuclide. Thus, while with external photon irradiation treatment the stages described above take place successively, in TRT with each emitted particle, a new process is started with the physical stage along the particle track. Therefore, in TRT all the described phases occur simultaneously, and the effects of these differences are not yet very well understood [11].

2.3 Targeted Radionuclide Therapy

This section introduces the key principles of TRT and details the chemical structures of the radiopharmaceuticals used to target PSMA. It also provides a brief overview of fundamental radiochemistry and radiopharmacy concepts, including the radiolabelling procedures employed.

2.3.1 Radiochemistry and Radiopharmacy

The development of radiopharmaceuticals is a complex process, as multiple factors simultaneously impact target-specific binding and pharmacokinetic properties. A delicate balance must be established between blood circulation time and clearance to enable sufficient accumulation at tumor lesions while minimizing exposure to non-targeted structures. The translation of a compound into clinical use requires years of optimization, involving the careful tuning of ligand specificity - influenced by the linker moiety connecting the ligand and chelator - and radionuclide-chelating agent interactions. Even small modifications can have a profound impact on these critical factors [71]. Regarding the employed radiopharmaceutical PSMA-617 targeting PSMA, the literature provides a comprehensive overview of the properties, including its chemical synthesis [72], stability measurements, and performance in vitro [73, 74] and vivo studies [75, 76]. Moreover, details on recent clinical developments will be presented in Chapter 3.
When working with radiopharmaceuticals, relevant quantities include molar activity A_m and specific activity A_s. The molar activity A_m of a radiopharmaceutical is defined as the amount of radioactivity per unit mole of the compound, with a unit of Bq/mol. Similarly, the specific activity A_s is defined as the amount of radioactivity per weight of the compound in the unit Bq/g [77].

Furthermore, the principle of radiolabeling is a crucial aspect of TRT. It is referring to the process of combining a target-specific pharmaceutical (ligand with attached chelator) with a chosen radionuclide (either for therapy or diagnostic imaging). Depending on the pharmaceutical, different radiolabelling methods are employed. In this work, the target molecule is used in excess and combined with an appropriate buffer to maintain compound stability throughout the labelling process. Subsequently, the radionuclide is added to the mixture, which is then heated to catalyze the reaction. The specific conditions for each radiolabelling procedure are detailed in Table 4.1 in the Methods Chapter. The goal of radiolabelling is to achieve a high radiochemical yield, defined as the percentage of radioactivity successfully attached to the pharmaceutical relative to the total radioactivity used. Maintaining a high radiochemical yield (typically > 95%) is essential to minimize the presence of cold (non-radioactive) pharmaceutical molecules, which can competitively bind to the target receptor without delivering therapeutic radiation. Excess cold compound may significantly reduce the effectiveness of treatment by blocking receptor sites and thereby impacting therapeutic outcomes. Furthermore, unbound radionuclides that did not successfully attach to the pharmaceutical and are therefore non-targeted can contribute to background signal, potentially causing false or misleading results in assays.

2.3.2 PSMA-targeting Radiopharmaceutical for Prostate Cancer

PSMA-617 consists of a ligand targeting the PSMA with high affinity linked to the chelator DOTA. In the scope of this work, mainly the radionuclides β^--emitter ^{177}Lu ($T_{1/2}$= 6.6 d, E_{e^-} = 0.5 MeV) and the α-emitter ^{225}Ac ($T_{1/2}$= 9.9 d, E_α = 6 MeV) were used in combination with the described pharmaceutical PSMA-617. As the DOTA chelator is not optimal for the radionuclide ^{225}Ac, instead of PSMA-617, an analogue was synthesized by Martin Schäfer, which is equipped with the Macropa chelator (PSMA-716). This analogue will be referred to as [^{225}Ac]Ac-PSMA-716 in the following. The structure of both radiopharmaceuticals is depicted in Figure 2.11. The Macropa chelator has proven favorable for studies with ^{225}Ac [78]. Both radiopharmaceuticals obtained high radiochemical yield above >95%. Details of the labeling procedure are stated in Table 4.1 in the next chapter 4 (Table 4.1).

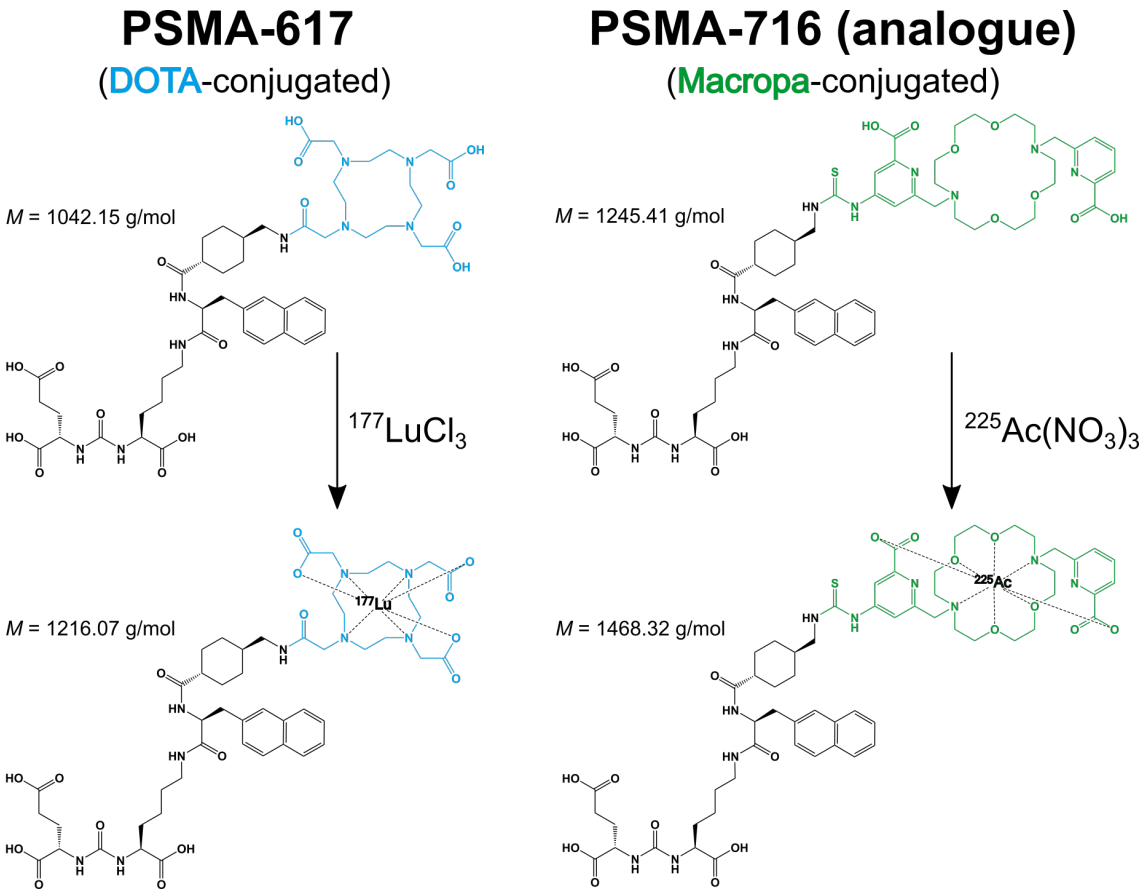

Figure 2.11: **Structure PSMA-617 and PSMA-716:** chemical structure of PSMA-617 and analogue PSMA-716 optimized for ^{225}Ac with the Macropa chelator instead of DOTA. Molar masses M are stated for both compounds before and after radiolabeling.
Chemical structures were drawn in ChemDraw® (Revvity Signals Software, Waltham, MA, USA) by Martina Benešová.

3 State of the Art: Targeted Radionuclide Therapy

The first clinical application of radiopharmaceuticals dates back to the 1940s, when the radioisotope ^{131}I ($T_{1/2}$= 8.0 d, Mean E_{e^-} = 0.97 MeV) was utilized in the treatment of benign and malignant thyroid disorders [79]. However, for nearly seven decades, Na^{131}I remained the sole therapeutic radiopharmaceutical, while focus was primarily on developing radiopharmaceuticals for diagnostic (imaging) purposes [80]. In 2013, the therapeutic potential of radionuclides gained momentum with the FDA approval of [^{223}Ra]$RaCl_2$(Xofigo®, Bayer, Berlin, Germany) for treating bone metastasis in patients with mCRPC [81].
The introduction of peptide-targeted radiopharmaceuticals marked a significant milestone for TRT, with the FDA approval of [^{177}Lu]Lu-DOTA-TATE (Lutathera®, Novartis, Basel, Switzerland) in 2018 for somatostatin receptor type 2 (SSTR2)-positive gastroenteropancreatic neuroendocrine tumors and [^{177}Lu]Lu-PSMA-617 (Pluvicto®, Novartis, Basel, Switzerland) in 2022 for the treatment of PSMA-positive mCRPC [82, 83]. The global success of these radiopharmaceutical therapies has sparked a surge in interest and attention towards developing additional radiopharmaceuticals to treat various types of cancer. According to the FDA, there are now 13 radiopharmaceuticals approved for therapeutic use [84]. The recent extension of the FDA approvals for pediatric patients with Lutathera® in 2024 [85] and Pluvicto® for use before chemotherapy in 2025 [86] demonstrates the potential of TRT as a future pillar in cancer treatment.
Within two decades, TRT has evolved towards precision medicine. Notably, the combination of a diagnostic agent with a therapeutic agent (the "treat what you see" approach) to form a theranostic pair offers a significant advantage in TRT, enabling more precise patient selection and close monitoring of treatment response. As illustrated schematically in Table 3.1, TRT holds promise in overcoming certain limitations of current SoC (EBRT and cytostatic chemotherapy) as well as emerging therapies like checkpoint inhibition immunotherapy. Clinical trials have demonstrated the efficacy of TRT as a monotherapy, offering systemic treatment that

is particularly valuable in advanced disease stages with widespread metastasis, where conventional first-line treatments, such as EBRT, often fall short. The direct and specific killing mechanism of TRT sets it apart from indirect approaches mediated through, e.g., activation of the immune system in checkpoint inhibition immunotherapy. While TRT offers numerous benefits, its relatively recent emergence as a treatment option means that several knowledge gaps must be addressed to optimize its use and unlock its full potential.

Table 3.1: **Comparison of SoC of cancer treatment options to Targeted Radionuclide Therapy**: five criteria of ideal cancer treatment are evaluated across the four treatments: EBRT, cytostatic chemotherapy, and checkpoint inhibition immunotherapy. Decisions are based on ideal working therapy and simplified treatment mechanisms to stress out the potential of optimized TRT.
✔ indicates that a treatment meets the desired criterion, (✔) signifies partial fulfillment, and ✗ denotes that a treatment does not achieve this goal.

	Treatment Modalities			
Criteria	EBRT	Chemotherapy	Immunotherapy	**TRT**
Effective Monotherapy	✔	✔	(✔)	✔
Treatment/ Target Monitoring	✗	✗	(✔)	✔
Directly Killing Tumor Cells	(✔)	(✔)	(✔)	✔
Systemic Treatment/ Metastasis Irradication	(✔)	✔	✔	✔
Selective and Specific Targeting	(✔)	(✔)	✔	✔

Understanding and predicting therapeutic efficacy and potential side effects of TRT requires a solid knowledge of radiobiology. Moreover, radiobiological principles are crucial for unraveling mechanisms of treatment resistance and informing effective combination therapies. Current reviews identify several knowledge gaps in this field, as highlighted below: [80, 87, 88]:

1. Influence of various radioisotopes on DNA damage and repair pathways: discover mechanisms and compare how radioisotopes with different energies, emission ranges, and radiation types impact DNA damage induction and repair mechanisms to establish accurate dose-effect relationships;

2. Understanding the causes of radioresistance: distinguishing between primary resistance at the start of treatment and acquired resistance during treatment;

3. Improving dosimetry-based estimation of absorbed dose: addressing challenges related to individual differences in absorbed dose deposition, patient-specific factors, and radiopharmaceutical properties;

4. Investigating non-targeted effects such as bystander, crossfire, and abscopal effects;

5. Developing effective combination treatment strategies: optimizing timing, sequencing, and dosing;

6. Exploring short- and long-term toxicity of TRT to identify potential side effects and long-term health impacts.

This research aims to address knowledge gaps 1, 3, and 5 by studying the radiobiology of α- and β^--emitting radionuclides. Understanding these differences is vital when selecting a radionuclide for therapeutic applications and designing radiopharmaceuticals with specific targeting properties.
On one side, β^--emitters require the attachment of hundreds of radiotracers to a targeted cell to induce damage, whereas α-emitters, due to their high radiotoxicity, can achieve this with only a few radiotracers [89]. On the other side, β^--particles are capable of irradiating large volumes of multicellular dimensions and are considered ideal for treating large tumors. In contrast, α-particles are better suited for irradiating small cell clusters and are typically used for treating hematological tumors or micrometastases.
Non-targeted effects, such as bystander and crossfire effects, have been observed for certain radiopharmaceuticals in various studies. Although the efficacy of these

effects may vary depending on the radionuclide used, they are important because they can compensate for biological heterogeneity in target expression and enhance therapeutic efficacy. For short-range α-particles, bystander effects have been reported, where non-irradiated cells exhibit irradiated-like effects due to signals received from a nearby irradiated cell. Upon bone irradiation in a mouse model by [^{223}Ra]RaCl$_2$, γH2AX foci and apoptosis were also observed in tumor cells beyond the range of the α-emitters (70 µm) [90]. In contrast, the crossfire effect is of higher relevance for the longer-range β^--particles, allowing radiation to affect nearby cells. *In vitro* dosimetry studies with 10%, 40%, and 70% of all cells labelled with ^{177}Lu prove that the β^--emitter is efficient in large cell clusters (0.5 mm to 1 mm) due to significant contribution to overall dose via the crossfire effect [91].

4 Experimental Design and Methods

The following Chapter presents the three studies conducted in the framework of this thesis, with all details necessary to reproduce or carry out similar studies. The study of **DNA damage induction and repair** (Section 4.1) was carried out, on the one hand, to evaluate the impact of different physical parameters of TRT on the biological effect (research question Q1 in Section 1.2) and, on the other hand, to identify differences in DNA damage induction and repair of α- and β^--emitters (research question Q3 in Section 1.2). **Simulation in GEANT4-DNA based on experimental data** (Section 4.2) aims to answer research question Q2. **Cell proliferation** (Section 4.3) was performed as a second biological assay to support the observations from DNA damage induction (research question Q2 in Section 1.2) and assess the potential of a combination therapy of TRT and a DNA repair inhibitor (research question Q4 in Section 1.2).

4.1 DNA Damage Induction and Repair via Immunofluorescent Microscopy

4.1.1 Rationale and Experimental Design

To assess the DNA damage induction, immunofluorescent microscopy of γH2AX was chosen. As explained in Subsection 2.1.1, γH2AX is the gold standard for observation of DSBs. As γH2AX is recruited rapidly to DNA damage sites (within 30 min), this method is suitable to detect early DNA damage. By measuring the signal of γH2AX foci over the course of time, DNA damage repair and radiosensitivity can be determined. γH2AX foci persisting after 24 h are an indication of DNA damage, which is difficult to repair [22, 92] . To determine the DNA damage at different time points, immunofluorescence staining for γH2AX was performed after fixing the samples at different time points.

Cells were exposed to radionuclides and radiopharmaceuticals directly in cell culture medium, allowing binding and internalization of the radiopharmaceuticals. To limit cross-irradiation between samples, a transwell insert system in a 24-well plate format was used. Cells were seeded in individual inserts, allowing spatial separation of samples on multiple 24-well plates during exposure to radionuclides, thus limiting possible cross-irradiation from one sample to the next.

4.1.2 Experimental Procedure

Cell Culture

Three established prostate cancer cell lines with different PSMA expression were selected. A non-PSMA-expressing cell line, PC-3, was chosen a control to evaluate impact of PSMA-targeting. All cell lines were obtained from the American Type Culture Collection (ATCC) :

PSMA-positive LNCaP: derived from an androgen-sensitive human lymph node metastatic lesion of prostatic adenocarcinoma, CRL-1740 [93]

PSMA-positive C4-2: derived from LNCaP under androgen-depleted conditions in a mouse model, CRL-3314 [94]

PSMA-negative PC-3: derived from a bone metastasis of a grade IV prostatic adenocarcinoma, CRL-1435 [95]

All three cell lines were grown in RPMI-1640 medium (#P04-16500) supplemented with 10% fetal calf serum (FCS) (#P40-37500) and 1% L-glutamine (L-GLN) (#P04-82100). Cells were incubated at 37 °C in an environment of humidified air containing 5% CO_2. Routine cell culture was performed regularly using room-temperature phosphate-buffered saline (PBS; pH 7.4, #P04-36500) for washing and 0.05% trypsin (#P10-023100) for cell detachment. All materials were ordered from PAN Biotech.
The cells were seeded 24 h prior to treatment in the transwell insert (#353095) placed in the companion plate #353504, Falcon®). A volume of 300 µL per insert with a density of $1.6 \cdot 10^5$ cells mL^{-1} was used. Details of the method can be found in the Appendix A.1.

Compounds and Radiolabelling

The structure of the used compounds, PSMA-617 and its analogue PSMA-716, optimized for ^{225}Ac radiolabelling, are disclosed in Subsection 2.3.2 (refer to Figure 2.11). Specifically, the structure of PSMA-617 was modified to incorporate a Macropa chelator, which is better suited for ^{225}Ac, instead of the DOTA chelator. Notably, the clinically used [^{225}Ac]Ac-PSMA-617 is the original PSMA-617 structure with the DOTA chelator. Both structures, PSMA-617 and PSMA-716, were synthesized and kindly provided by Martin Schäfer. For synthesis and analysis, all chemicals (>95% purity; for radiolabeling, highly pure chemicals) and solvents (HPLC-grade purity; for radiolabeling, metal-free ultrapure water) were purchased commercially from CheMatech (Dijon, France), Iris Biotech (Marktredwitz, Germany), Merck (Darmstadt, Germany), Sigma-Aldrich (Taufkirchen, Germany), and VWR International (Bruchsal, Germany) and used as received without any further purification or drying.
In the following, the conditions of the radiolabeling are stated. Physical parameters of the used radionuclides ^{177}Lu and ^{225}Ac, are given in Subsection 2.2.1 (refer also to Table 2.1).
The radionuclide ^{177}Lu was purchased from ITM Pharma Solutions (Garching, Germany) as $^{177}LuCl_3$ in liquid form solved in 0.04 M HCl.
The radionuclide ^{225}Ac was supplied by Prof. Svetlana Selivanova from the Canadian Nuclear Laboratories (CNL, Chalk River, Canada) in a solid form as [^{225}Ac]-$AcCl_3$. Additionally, ^{225}Ac was provided by the European Commission, DG Joint Research Centre (JRC Karlsruhe, Germany) in solid form as $^{225}Ac(NO_3)_3$, by BWXT in solid form (Vancouver, Canada) and by Global Morpho Pharma (GMP, La Chapelle-sur-Erdre, France) as $^{225}Ac(NO_3)_3$ dry film. For experiments, the full activity batch was subsequently diluted in ultra-pure and metal-free 0.04 M HNO_3 (TraceMetal Grade nitric acid, 67–69%, Fischer Scientific), resulting in $^{225}Ac(NO_3)_3$.
Radiolabeling was always performed directly on the same day as treatment. Details of radiolabeling conditions for ^{177}Lu and ^{225}Ac can be found in Table 4.1. Conditions were kept similar for each experiment, only the volume of activity differed slightly depending on the actual activity concentration. Radio-chemical yield (RCY) was determined for each labeling by reversed phase thin layer chromatography (TLC Silica gel 60 RP-18 F_{254}s, #1055600001, Merck, Darmstadt, Germany). As liquid phase, Na citrate (0.1 M, pH 5.5) was used.

Table 4.1: **Radiolabeling conditions for ^{177}Lu and ^{225}Ac:** details of radiolabeling for both PSMA-compounds. Concentration was 1 mM for PSMA-617 and 0.5 mM for PSMA-716, solved in DMSO first and further diluted to the specified concentration in ultrapure H_2O. Radiolabeling was performed in 1.5 mL Eppendorf tubes (Protein LoBind®).

Radiolabeling conditions	$^{225}Ac(NO_3)_3$	$^{177}LuCl_3$	Volumes
Activity	1 MBq	20 MBq	5-10 µL
Buffer	TRIS 0.1 M, pH 7.0	sodium acetate 0.4 M, pH 5.0	50 µL
Compound	2 nmol PSMA-716	1 nmol PSMA-617	4 µL / 1 µL
Temperature	95 °C	95 °C	
Time	15 min	30 min	
Molar activity	0.5 MBq/µmol	20 MBq/µmol	
RCY (via radio-RP-TLC)	>96%	>99%	

The radionuclide ^{223}Ra was provided by Bayer Vital GmbH (Leverkusen, Germany) as the product Xofigo® ([^{223}Ra]$RaCl_2$, PZN - 11595344) [96].
The radionuclide ^{227}Th was manufactured at IFE (Oslo, Norway) and provided as [^{227}Th]$ThCl_4$.

Treatment

An illustration of the experimental workflow is given in Figure 4.1. Cells were treated 24 h after seeding. Treatment consisted of exposure to radionuclides - non-targeted radionuclides: [^{225}Ac]$Ac(NO_3)_3$, [^{177}Lu]$LuCl_3$, [^{223}Ra]$RaCl_2$, and [^{227}Th]$ThCl_4$ or PSMA-bound radiopharmaceuticals [^{177}Lu]Lu-PSMA-617 and [^{225}Ac]Ac-PSMA - directly in the cell culture medium. Therefore, different concentrations of radionuclides and radiopharmaceuticals were prepared with the usual supplemented cell culture medium. Used activities and corresponding activity concentrations are displayed in Table 4.2.
Additionally, some samples were treated with external photon irradiation to compare with the gold standard in radiation biology. Therefore, the Multirad225-X-ray Faxitron was used [97]. For the dose rate of 2.151 Gy/min, the irradiation times

given in Table 4.2 were performed on Shelf 4 to reach doses between 0.5 Gy to 2.5 Gy.

Table 4.2: **Administered activities in DNA damage induction assay:** the initial activity concentration was measured in an ISOMED 2010 dose calibrator, based on which further dilutions were then calculated for the lower activity concentrations below the ISOMED measurement range [98]. Irradiation times for external photon irradiation were calculated from the given dose rate of 2.151 Gy/min (Multirad225-X-ray Faxitron [97]).

TRT	**α-emitter** ^{225}Ac, ^{223}Ra, ^{227}Th	**β^--emitter** ^{177}Lu	**external irradiation** X-rays (γ)	
Total activity per sample [kBq]	0 / 1 / 5 / 10 / 100	0 / 100 / 500 / 1000 / 5000	Dose [Gy]	0.0 / 0.5 / 1.0 / 1.5 / 2.0 / 2.5
Activity concentration [kBq µL^{-1}]	0.000 / 0.003 / 0.016 / 0.033 / 0.333	0.00 / 0.33 / 1.67 / 3.33 / 16.67	Irradiation time [min]	00:00 / 00:14 / 00:28 / 00:42 / 00:56 / 01:10

Medium in the transwell inserts was exchanged with the active solution (300 µL), and cells were arranged on multiple 24-well plates spatially distanced to avoid cross-irradiation effects. Plates were incubated at humidified 37 °C in 5% CO_2 for either 1 h or 4 h. At the end of the radioactive exposure time, the radioactive medium was removed and replaced with non-active, usual supplemented medium. Samples were then fixed following the procedure in the Appendix at specified time points (refer to A.1).

Immediate DNA damage: directly after 1 h and 4 h of radionuclide exposure, furthermore fixation after 1 h radionuclide exposure and 3 h of recovery time with non-active medium to achieve equal biological time (total 4 h after treatment started). Samples treated with external photon irradiation were fixed 30 min post-irradiation.

These time points were also used to evaluate the influence of physical parameters such as activity concentration and exposure time on induced DNA damage and to compare the two emitter types α and β^-.

DNA damage and repair: for long term observation, fixation after total time of 24, 48 and 72 h after treatment started (repair time = total time - active incubation period (either 1 or 4 h));

Samples irradiated externally were also fixed at 4, 24, 48 h post-irradiation.

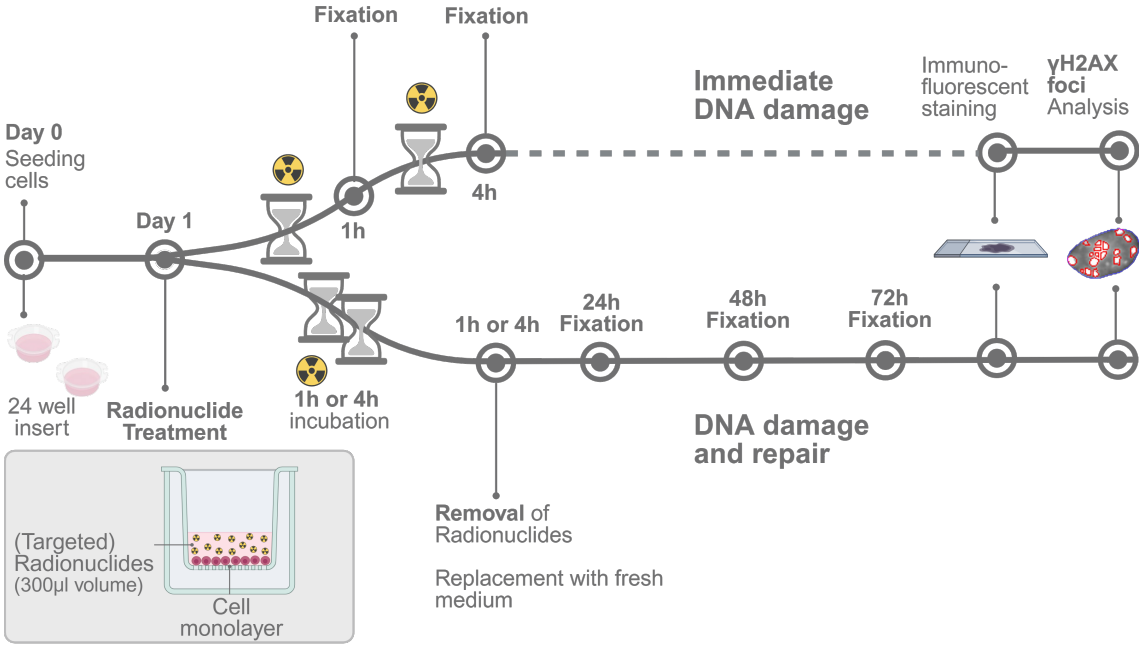

Figure 4.1: **Experimental workflow DNA damage induction in TRT:** samples were incubated with medium containing non-targeted radionuclide or radiopharmaceuticals with activities specified in Table 4.2. Samples were fixed following the procedure in the Appendix A.1 at various time points.
Created in Biorender https://BioRender.com

Immunofluorescent Staining for γH2AX

To observe the DSBs, immunofluorescent staining for γH2AX was performed following the protocol in the Appendix. An indirect immunofluorescence antibody staining was executed, using a primary antibody targeting the phosphorylation on the 139th serine of the H2AX histone protein, hence γH2AX (#BLD-613402, Biozol). The secondary antibody (#AB_2534088, Thermo Fisher Scientific), tagged with the desired fluorophore Alexa Fluor™ 488, then recognizes the primary antibody and binds to it. This method was chosen for its high sensitivity and robustness. Additionally, for the staining of the cell nucleus DAPI (4',6-Diamidin-2-phenylindol, #D1306, Thermo Fischer Scientific) was used, which is the most common nucleic stain. Detailed procedure of the immunofluorescent staining can be found in the Appendix A.1.

Microscopy

The samples were imaged using the inverted microscope Nikon Eclipse Ti2-E [99]. For magnification, the CFI Super Plan Fluor ADM ELWD 20x objective (#MRH48230, N.A. 0.45/ working distance 8,2-6,9 mm) was combined with a 1.5x lens, resulting

in a total magnification of 30x. Cell nuclei with DAPI stain were imaged in wide-field fluorescence with an exposure time of 50 ms (filter LED-DAPI-A, MXR00714, Semrock, excitation 392/23 and emission 447/60). γH2AX was imaged in the GFP channel with an exposure time of 400 ms (filter LED FITC-A, MXR00716, Semrock, excitation 474/27 and emission 525/45). The gain was set to 1 for both fluorophores. Images were saved in .nd2 format as well as exported as single .tif images for each channel and position. Depending on the cell density of the individual sample, 10-20 different positions were taken, aiming for a total of 400-1000 cells per sample for further analysis.

4.1.3 Analysis Procedure

The single .tif images were then further processed to analyze γH2AX foci on single cell level. For this purpose, algorithms implemented by Ramon Lopez Perez in the software MATLAB (MATLAB R2022b Update 2, 9.12.0.2105380, the MathWorks, Natick, Massachusetts, USA) were used. The individual processing steps are illustrated in Figure 4.2. The images acquired in the DAPI channel were taken to identify the single nuclei. Parameters for nuclei identification were optimized to separate nuclei close to each other and exclude nuclei not in focus. A mask for each nucleus was created and applied to the images in the GFP channel (γH2AX staining). Foci were then segmented in the single nuclei. By variation of multiple parameters, background correction and foci segmentation could be optimized. The output of the analysis includes the following parameters for each analyzed cell:

Nucleus specific: Total intensity, Contour Area [px], Total intensity of γH2AX signal in the nucleus mask

Foci specific: Number of Foci, Mean intensity of γH2AX foci, mean focus area [px]

For each sample, the analysis results of all single cells were further processed leading to the following output:
Number of nuclei in the sample (# nuclei), number of nuclei without foci identified, mean number of γH2AX foci and the corresponding error (std/$\sqrt{\#\,\text{nuclei}}$)), maximal and minimal number of foci, mean foci intensity, mean foci area and corresponding error, total nuclear intensity of DAPI stain, total γH2AX intensity.

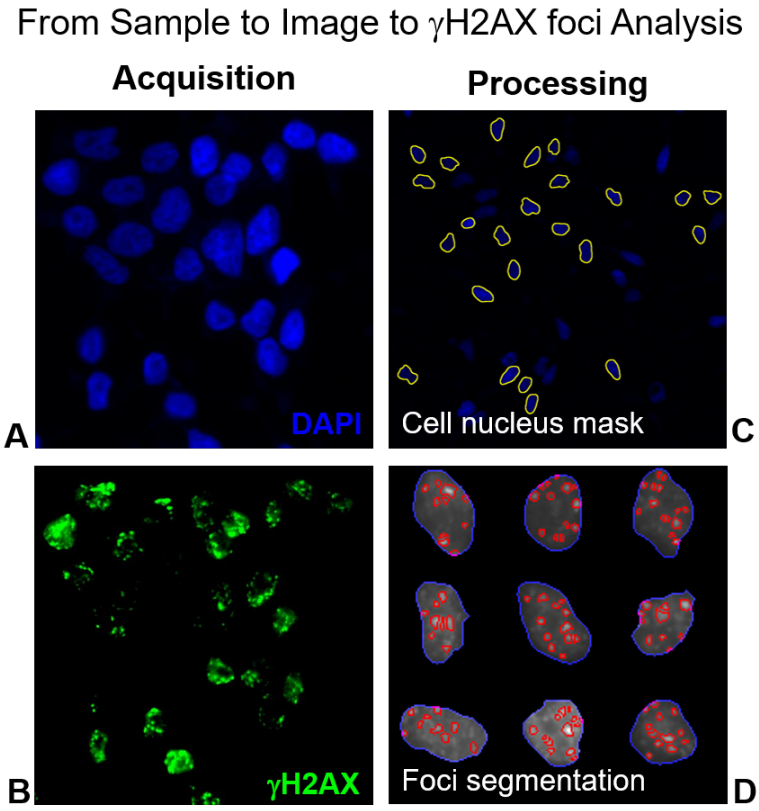

Figure 4.2: **Image processing with MATLAB:** immunofluorescence microscope images (A, B) were processed in MATLAB to count single γH2AX foci. First, the nuclei were identified (marked by a yellow rim, C), based on the DAPI channel, then single foci were segmented in the GFP channel (red selections, D).

For statistical analysis, the mean of these parameters for duplicates within one experiment and for reproduced experiments under the same conditions was taken. These were calculated in the software Jupyter Notebook (version 6.5.7, using Python 3.12.7 [100]). Graphic visualization of the data was done in Jupyer Notebook as well. Mean values of γH2AX foci number, foci area or intensity for each treatment are plotted against the applied activities/doses for each cell line. Mean values are displayed as dotted curves, with the standard deviation for the mean values visualized as transparent band around the curve. However, only discrete measurements at the specified activity values were performed. This visualization was chosen explicitly to facilitate comparison between different treatment conditions such as non-targeted vs. PSMA-bound activity. For some measurements the standard deviation is quite larger, representing biological variability in the data, which could be attributed to different passage numbers.

4.2 Simulation in Geant4 DNA based on Experimental Data

4.2.1 Rationale and Aims

TRT is a novel, promising therapeutic approach. However, the knowledge of the effect of TRT, such as the patient's response to therapy and the dose required for successful treatment, is sparse. Monte Carlo modeling of DNA damage can make an important contribution to the validation of experimental data and the simulation of effects depending on radionuclides distribution. The GEANT4-DNA extension of the general-purpose Geant4 (Geometry and Tracking) Monte Carlo toolkit is ideally suited for this task. This simulation toolkit not only simulates the physical DNA strand breaks induced by the radionuclides, but also predicts the repair of DNA damage and the formation of γH2AX foci.
The main activity in this project is dedicated to the first experimental validation of the Geant4-DNA simulation toolkit for the modeling of direct and indirect biological damage induced by α- or β^-particles in human cells. This validation takes place in two steps, combining Monte Carlo simulations and special radiobiological experiments to distribute the radionuclides. The first simulation is intended to determine the absorbed dose of different radionuclides (^{177}Lu, ^{227}Th, ^{223}Ra and ^{225}Ac) depending on their biological distribution in a single cell model. The aim is to investigate the influence and effect of different distributions of these radionuclides (at the cell membrane, in the cytoplasm) on the absorbed dose (details in Subsection 5.2.2). This will be performed with a simplified model, which can then be expanded and adapted to a more accurate simulation of the experimental situation in the future. Experimental data will be evaluated to get a baseline distribution of localization of radionuclides (refer to Subsection 4.2.3 and 5.2.1).
In the further process, a more advanced model for simulating induced DNA damage (SSB, DSB, complex DSB) will be developed to compare simulation results with the experimental results of the DNA damage induction test (see section 4.1). This comparison may enable us to better understand the DNA damage mechanisms of TRT at the nanometre level, representing one of the most promising approaches in cancer treatment. Furthermore, an accurate model would enable the simulation of different experimental situations *in silico* and decide on the most promising experiment approaches. Combining the large experimental data set and suitable simulation would provide foundational knowledge about dosimetry and therapy

optimization for patients. In addition, validation of the GEANT4 DNA toolkit with experimental data is crucial to further improve simulation accuracy.
Aim of this chapter is to introduce basic principles of Monte Carlo modeling and the GEANT4 DNA toolkit (Subsection 4.2.2). In Subsection 4.2.3, the method to determine the radionuclide localization experimentally is described. The insights gained from this assay shall serve as the foundation for the first simulation.

4.2.2 Introduction into Geant4-DNA

Geant4 a Monte Carlo simulation toolkit for the simulation of the passage of particles through matter with high precision, and includes extensive libraries for physical processes across a wide range of energies. Monte Carlo simulations are a method to predict the probability of various events when the potential for a random variable is present. More specifically, it is impossible to predict or simulate the exact path of a single α-particle, because the single interactions of the particle with matter are random and not predictable. However, by modeling the process with a high statistical rate (1000 or more α-particles), the track length and deposited energy of an α-particle of a certain energy passing a defined material can be estimated. This method is widely applied in treatment planning and dose estimation for patient in clinics.
Geant4 is a free software package, and the source code is available under an open-source license [101, 102]. Within the Geant4 toolkit, it is possible to define the geometry of a simulation, the environment (such as physics, interaction of particles with matter), and the tracking of particles during a simulation run. Parameters like deposited energy and particle track length can be extracted from a simulation run. Visualization of geometry and the passage/track of various particles is possible.
Geant4 DNA extends the Geant4 toolkit further to model processes induced by ionizing radiation, like biological damage at the DNA scale. The physics processes in Geant4-DNA are based on interactions with water and other biological materials [103]. Additionally, physico-chemistry and chemistry are implemented to enable modeling of water radiolysis and thus induction of DNA damage described in Subsection 2.2.2 [104]. Molecular geometries, like DNA molecules, allow quantification of biological DNA damage *in silico* and differentiation of SSB, DSB and complex DSB [105–108]. The ability of Geant4-DNA to represent radiation interactions at nanometric scales makes it particularly well-suited for modeling the biological effects of TRT, where the spatial distribution of energy deposition is highly localized

and can vary significantly depending on the intracellular distribution of the radiopharmaceutical.
Geant4-DNA has already been applied to simulate effects of TRT on single cell level as well as on cell layers [109–111].

4.2.3 Experimental Localization of Radionuclides with Cellular Uptake Assay

To determine the binding to cellular membrane and internalization of the used radiopharmaceuticals ([^{177}Lu]Lu-PSMA-617 and [^{225}Ac]Ac-PSMA-716) as well as unlabeled radionuclides ($^{177}LuCl_3$, $^{225}Ac(NO_3)_3$ and $^{223}RaCl_2$), the cellular uptake assay was applied. For this assay, cells are plated in a 24-well plate one day before the experiment. As the adherence of the LNCaP cell line is weak, plates were coated with poly-L-lysine before plating of the cells. The assay was performed with all three cells lines (LNCaP, C4-2 and PC-3) described in Subsection 4.1.2.
Cells were treated with radionuclides and radiopharmaceuticals at different activity concentrations. Radiolabeling was performed analogically to parameters stated in Table 4.1. Cells were incubated at 37 °C with 250 µL of radioactivity diluted in supplemented cell culture medium for a specific time. At the end of the incubation period, the radioactive medium was removed and cells were washed three times with 500 µL of ice-cold PBS. To assess the membrane-bound activity, cells were incubated twice with 500 µL of glycine buffer (50 mM; pH 2.8) for 5 min. Then the cells were again washed once with 500 µL of ice-cold PBS and lysated afterwards with 500 µL of NaOH (0.3 M; pH 14) to evaluate internalized fraction. Both fraction of glycine wash (for membrane binding) and lysate (for internalization) were collected in gamma counter tubes and counted directly in a gamma counter (^{177}Lu: Cobra Autogamma B5003, Canberra, Packard; Frankfurt, Germany, ^{225}Ac and ^{223}Ra: 2410/2470 Wizard2, Perkin Elmer, Waltham, USA). To account for total activity, a defined fraction of the radioactive incubation medium (1/10 = 25 µL) was measured as standard. For statistical purposes, all conditions were performed at least in triplicate.
For analysis, the mean was calculated from the triplicate for each condition. The average percentage of membrane-bound activity was then calculated by normalizing the sum of both glycine washes to the total activity used, determined by the standard measurements. The average percentage of internalization was calcu-

lated likewise, normalizing the lysate by the total activity. All calculations were performed in Excel (Microsoft Excel 2019, Microsoft Corporation), and data visualization in Jupyter Notebook.

4.3 Effect of Mono- and Combination Therapy on Cell Proliferation

4.3.1 Rationale and Experimental Design

The γH2AX immunofluorescent assay evaluating the DNA damage and repair after exposure to TRT (compare Section 4.1), can only measure the direct impact on DNA damage through TRT. However, the assay is limited in predicting long-term effects of the treatment, such as the ability to proliferate. Since cancer cells can acquire mechanisms to overcome or ignore even persistent DNA damage, it is crucial to additionally assess cell proliferation after treatment. Cell proliferation is an important indicator of the biological effectiveness of the treatment that cannot be extrapolated from DNA damage alone. Furthermore, the assessment of cell proliferation is also used to test a combination therapy of TRT and a DNA repair inhibitor, more specifically a DNA-PK inhibitor. To determine the most effective combination, several parameters must be tested, such as different activity concentrations (TRT) and concentrations of the DNA-PK inhibitor, as well as a treatment plan for the combination: subsequent or parallel treatment, with the order having the better effect. That is why an assay that enables high throughput and quick evaluation is favorable.
As a method for assessing cell proliferation, the resazurin assay was chosen [112–114]. Resazurin is a cell-permeable, blue redox dye, which is reduced only by viable, metabolically active cells to resorufin. As resorufin is a highly fluorescent pink compound, the amount of metabolically active cells can be determined by measuring the fluorescence intensity. Hence, the study of cell proliferation by the resazurin assay allows for the determination of the number of viable cells after treatment, as well as directly comparing different treatment conditions to each other by studying differences in fluorescence signal (shift from blue to pink).

4.3.2 Experimental Procedure

Cell Culture

The three prostate cancer cell lines described in Subsection 4.1.2 were used. One day before the experiment (Day 0), cells were seeded in 96-well flat-bottom plates (sterile cell culture plate with flat bottom, color: black with transparent bottom, #644090, Kisker Biotech). To account for the different proliferation rates of the three cell lines and to ensure that the density at the end of the experiment (day 8) is still within the sensitive range of the resazurin test, a different cell number was seeded for each cell line. The optimal number of cells, incubation length, and incubation time with resazurin were determined in preexperiments. LNCaP are the slowest proliferating cells and PC-3 the fastest, resulting in the following numbers seeded for each cell line per well: 1750 (LNCaP), 1300 (C4-2), 1000 (PC-3). Details of the procedure are specified in Appendix C.2.

DNA Repair Inhibitor

As highlighted in Paragraph 2.1.1, DNA-PKi can be used to block DNA repair and radiosensitize cells, possibly also overcome radioresistance. In this work, the commercially available DNA-PKi Nedisertib® (M3814, Peposertib®, MSC2490484, #S8586, Selleckchem) was chosen, which has already proven to enhance the effect of EBRT *in vitro* and *in vivo* [31]. Assessment of its safety profile in clinical trials (NCT02316197, NCT02516813) as monotherapy and in combination with EBRT has shown positive results [115]. *In vitro* studies reported that Nedisertib® can suppress the repair of radiation-induced DNA damage by NHEJ, leading to mitotic catastrophe and apoptotic cell death in cancer cells deficient in the other main repair pathway, HR [116]. The compound was prepared according to the manufacturer's instructions. A range of concentrations was then prepared from the initial stock, two controls (control 0 µM, DMSO control) and six concentrations of Nedisertib® (0.01, 0.1, 1, 5, 10 and 50 µM). Details of the preparation are documented in Appendix C.2.

Compounds and Radiolabelling

The radiopharmaceuticals [^{177}Lu]Lu-PSMA-617 and [^{225}Ac]Ac-PSMA-716, described in Section 4.1.2 were used in this assay. Additionally, the radionuclides ^{177}Lu and ^{225}Ac were used in their unlabeled form as $^{177}LuCl_3$ and $^{225}Ac(NO_3)_3$. Radiolabeling procedures are identical to the ones specified in Table 4.1. ^{223}Ra and ^{227}Th were not used in this assay due to limited availability.

Treatment

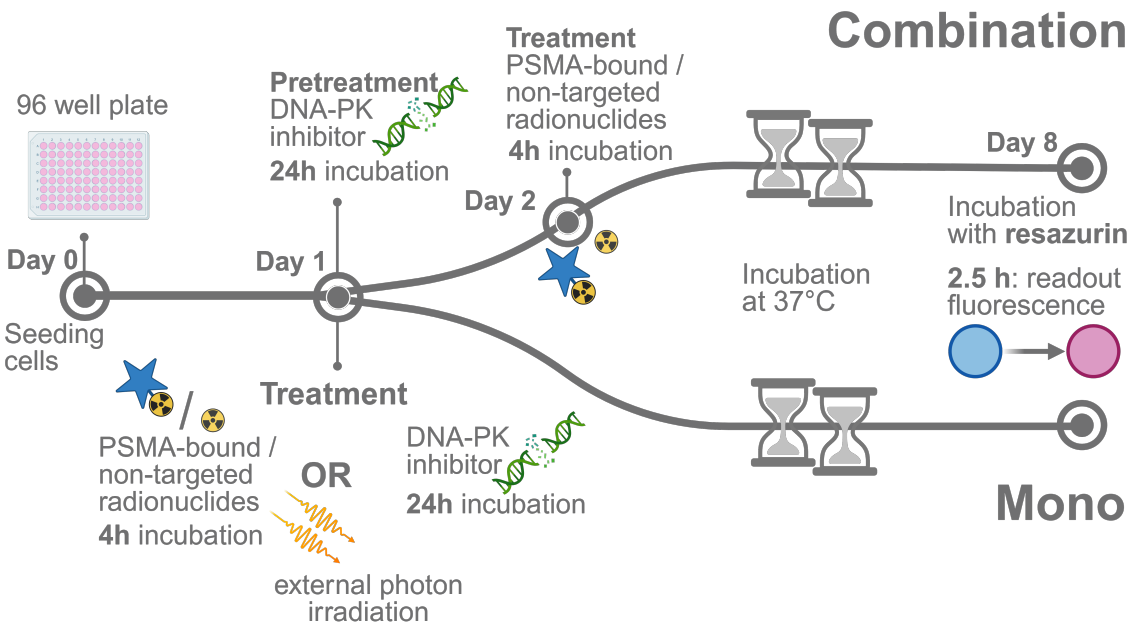

Figure 4.3: **Experimental workflow cell proliferation assessment:** monotherapy involved treatment of cells with either TRT, external irradiation or DNA-PKi Nedisertib® at Day 1. Cells were incubated with medium containing non-targeted radionuclides or radiopharmaceuticals or DNA-PKi Nedisertib® , with concentrations specified in Table 4.3.
For combination therapy, cells were treated with DNA-PKi Nedisertib® on Day 1 and then with TRT on Day 2.
In both assays, the endpoint was on Day 8, when the cells were incubated with resazurin-supplemented medium for 2.5 h and then the fluorescence signal was read out via a plate reader.
Created in Biorender https://BioRender.com

Cells were treated 24 h after seeding, at Day 1. Before starting with combination treatments, all treatment modalities were thoroughly assessed as monotherapy. The treatment modalities comprise TRT with an α-emitter ([^{225}Ac]Ac-PSMA-716 or $^{225}Ac(NO_3)_3$) or a β^--emitter ([^{177}Lu]Lu-PSMA-617 or $^{177}LuCl_3$), the DNA-PKi Nedisertib® as well as external photon irradiation (Multirad225-X-ray Faxitron) as gold standard for comparison. The concentrations used for TRT and DNA-PKi are stated in Table 4.3. Combination therapies were then executed following the scheme in Figure 4.3. For combination with TRT, pretreatment with DNA-PKi was done on Day 1, with an incubation time of 24 h. Hence, on Day 2, DNA-PK supplemented medium was removed, replaced by usual supplemented medium (1x wash), and then exchanged with TRT supplemented medium. The radioactive exposure time was 4 h, similar to the DNA damage assessment. After 4 h, the active medium was

removed and replaced by the usual supplemented medium.
For combination with external photon irradiation, pretreatment with DNA-PKi was performed as described above on Day 1. After 1 h of pretreatment, cells were irradiated at specified doses. Afterwards, the cells were placed again in incubation. The DNA-PKi-supplemented medium was then removed after a total of 24 h incubation time at Day 2 and exchanged for the usual supplemented medium. Cells were incubated again until Day 8. This procedure was performed analogously to previous experiments performed at the institute with the DNA-PKi and external photon irradiation.

Table 4.3: **Administered concentrations in cell proliferation assay:** for TRT initial activity concentration was measured in a dose calibrator ISOMED 2010, further dilutions for lower activity concentrations below the range of the ISOMED were performed by 1:4 dilution between each concentration [98]. Irradiation times for external radiation (Multirad225-X-ray Faxitron [97]) were calculated from the dose rate of 2.151 Gy/min.

TRT				**external photon irradiation X-Rays**	**DNA-PK inhibitor** Nedisertib®
α**-emitter** ^{225}Ac	β^-**-emitter** ^{177}Lu	α**-emitter** ^{225}Ac	β^-**-emitter** ^{177}Lu		Compound
Activity concentration [kBq mL^{-1}]		Activity per sample [kBq]		**Dose** [Gy]	concentration [µM]
control (0)	0	0	0	0	0
0.156	78	0.023	12	1.5	0.01 5
0.625	312	0.094	47	2.5	0.1 10
2.5	1250	0.375	188		1 50
10	5000	1.5	750		

Cells were then allowed to proliferate until Day 8 under usual cell culture conditions. Quadruplets of each experimental condition were seeded.
In addition, pretreatment with TRT and subsequent treatment with DNA-PKi and parallel treatment with both modalities were investigated with ^{225}Ac.

Measurement of Fluorescence Signal

As explained above, cells were incubated until Day 8, and then the cell proliferation was measured via the resazurin assay. For the assay, the cell medium was exchanged with cell medium supplemented with 10% of resazurin stock solution, with a volume of 165 µL per well. Cells were incubated for 2.5 h until the fluorescence difference between samples maximized. Then plates were measured using the fluorescence readout function of the plate reader Varioskan Lux with excitation set to 530 nm and emission to 590 nm (Software Skanlt). For statistical analysis, each plate was subsequently measured five times.

4.3.3 Analysis Procedure

Data of the plate reader Varioskan Lux was exported in .xlsx files, which could be further processed in Excel (Microsoft Excel 2019, Microsoft Corporation). For each well, the mean was calculated from the five measurements. Then of the quadruplet for each experimental condition, the mean and the standard deviation were calculated. All samples were then normalized to the control (completely untreated) of the corresponding experiment. Data was then imported into Jupyter Notebook (version 6.5.7, using Python 3.12.7 [100]). If multiple repetitions of the same experimental setup were performed, the mean of the normalized values was calculated.
Graphic visualization of the data was done in Jupyer Notebook as well. Mean values of normalized cell proliferation for each treatment are plotted against the applied activities/doses for each cell line. Mean values are shown as dotted curves, with the standard deviation represented by a transparent band surrounding each curve. However, it is important to note that only discrete measurements were performed at specific activity or compound concentrations. This style of visualization was intentionally chosen to facilitate comparison between different treatment conditions, such as non-targeted versus PSMA-bound activity. For some measurements, the standard deviation is considerably large, reflecting biological variability in the data. This variability could be attributed to differences in passage number, which may influence results in this multi-day assay.
To assess statistically significant differences between treatment conditions - such as different radiation types (α-emitter vs. β^--emitter) or targeting strategies (PSMA-bound vs. non-targeted activity) - a paired Student's t-test was used. This test was

appropriate because the data were obtained from the same cell line under experimental different conditions, meaning the samples were not independent. Using a paired test controls for biological variability within the same system, allowing more accurate detection of treatment-specific effects. All statistical analyses, including t-tests, were performed using Jupyter Notebook.

5 Results

Four different research questions were specified in the introduction. In the previous Chapter 4, three main studies were presented, the results of which aim to address the questions raised. A brief overview of the four questions and the related studies is given.

Q1 studies the impact of various physical parameters on the outcome of TRT. DNA damage induction (Section 4.1) and cell proliferation (Section 4.3) after TRT were studied to gain further insights on biological effectiveness of parameters such as emitter type, activity concentration, and exposure time. Detailed results are presented in the next Section 5.1.

Q2 focuses on understanding how to design a Monte Carlo simulation that models the effects of TRT within a single-cell framework. The primary objective is to estimate the energy deposited in the cell nucleus, which depends on the subcellular localization of the radionuclides. To inform the simulation, cellular uptake experiments were conducted to determine the localization patterns of radionuclides for the radiopharmaceuticals used (see Subsection 4.2.3). Geant4-DNA is introduced as a suitable platform for developing such simulations (see Subsection 4.2.2). Section 5.2 presents both the experimentally determined radionuclide localizations and the development of a simplified single-cell simulation. The ultimate aim—modeling DNA damage induction—is discussed in the following chapter (see Section 6.2).

Q3 deals more specifically with the induction and repair of DNA damage and with the characteristic structure of DNA damage patterns. Differences of α- and β^--emitters are hereby in focus (Section 5.3).

Q4 aims for an initial proof of concept for a effective combination therapy of TRT and a DNA-PKi, Nedisertib®. Different parameters to optimize treatment settings, such as concentrations of single compounds and treatment schedule, are studied (Section 5.4).

5.1 Physical Parameters Determining the Biological Effect

The biological effects of TRT - including DNA damage induction, repair processes, and eventual cell death - depend on several key characteristics of the radionuclide used. These include its physical properties, such as the type of radiation emitted (e.g., α- or β^--particles), the energy of the emitted particles, and the physical half-life of the radionuclide. Each of these factors contributes to the damaging potential of TRT. Radiation type and energy define the range and impact of DNA damage and are therefore crucial to the effect of a single particle. The half-life determines the temporal distribution of emissions, affecting how frequently particles are emitted and, therefore, the likelihood of damage occurring within a specific time frame. In addition to these specific properties, the total activity administered in treatment is a key parameter, as it defines the overall number of decay events and thus the cumulative potential for biological damage. As α-emitters have a greater biological effectiveness than β^--emitters, different ranges of total activity are necessary to induce a comparable effect. This relationship is assessed quantitatively in this section. Furthermore, concerning TRT, the targeting itself and the resulting localization of radionuclides play a crucial role. The potential of the targeted approach is investigated by comparing PSMA-targeted radionuclides to their non-complexed, non-targeted counterparts. In addition, three different cell lines are used, of which two are expressing the target receptor (PSMA) and one is not. As a last parameter, the effect of the exposure time, hence incubation length with radionuclides, is studied. The standard of 4 h exposure time is compared to a reduced exposure time of 1 h. The immediate DNA damage after 1 h and the DNA damage after 1 h and additional 3 h recovery time before fixation, resulting in a biological repair time equal to the 4 h exposure time sample, are examined.

5.1.1 Qualitative Observations - Differences between the Radiation Types

Before discussing the parameters in detail, a brief qualitative overview will be provided in this subsection. As mentioned earlier, α- and β^--emitters demonstrate distinct biological effectiveness. Therefore, a specific range of activities for each emitter type was selected to achieve comparable numbers of γH2AX foci.

For α-emitters, total activities of 1 kBq to 100 kBq were used, and for β^--emitters, 100 kBq to 5000 kBq. For external photon irradiation, which served as the gold standard, a dose range of 0.5 Gy to 2.5 Gy was applied, corresponding to typical values used commonly in *in vitro* studies [117].

Figure 5.1 exemplifies representative microscopy images with immunofluorescent γH2AX staining, along with corresponding detected γH2AX foci numbers per nucleus and total γH2AX intensity per nucleus for all three radiation types. The signal intensity and number of γH2AX foci are visually and numerically comparable across all three radiation types within the employed activity and dose ranges. This similarity enables a direct quantitative comparison, which will be presented in the following subsections.

Beforehand, some characteristics of the radiation types can be deduced qualitatively from the Figure 5.1. By examining the γH2AX distribution within the displayed cells, it becomes apparent that β^--emitters and external irradiation result in a homogeneous distribution spread across the individual cells, whereas α-emitters induce bright and larger foci within the cell but exhibit a heterogeneous distribution across cells. Comparing equal activities of 100 kBq for both α- and β^--emitters, the distinct biological effectiveness of both emitter types is evident. While with the β^--emitter ^{177}Lu, the effect of 100 kBq is visually almost indistinguishable from the control, the same activity with the α-emitter ^{225}Ac induced so much DNA damage that it led to an almost homogeneous γH2AX staining of the entire nucleus. As the analysis method is unable to separate single foci anymore in this setting, the detection of foci number decreases, while the increase of DNA damage is clearly visible in the total γH2AX intensity.

Comparing the distribution of the γH2AX foci, it appears that external irradiation and β^--emitters induce smaller but more numerous foci, whereas foci induced by α-emitters are larger and less frequent per cell. Overall, the foci number increases more slowly with α-emitters, resulting in a lower total number of detected foci compared to β^-- and external irradiation. Additionally, the brightness of α-particle-induced foci is higher and increases strongly with activity, while the increase is less pronounced for β^--emitters and the intensity remains almost constant with external irradiation. These differences are connected to the distinct DNA damage induction mechanisms among the radiation types (α-emitters: direct; external irradiation and β^--emitters: indirect), which will be further discussed in Subsection 5.3.

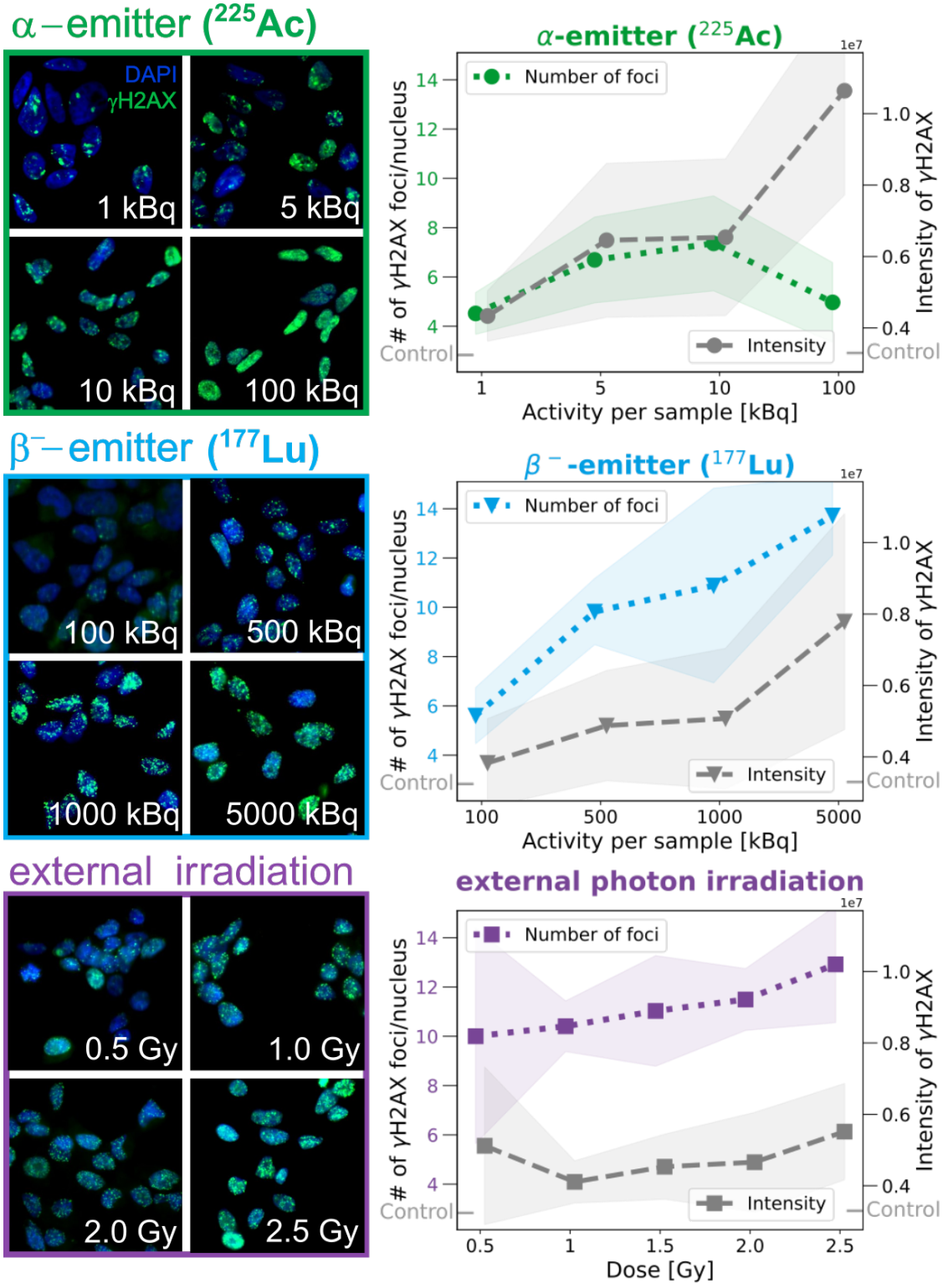

Figure 5.1: **Microscopic overview of DNA damage induction by different radiation types:** on the left side, a qualitative overview of DNA damage induction is visualized by immunofluorescent γH2AX staining (green) of the three radiation types studied, α- and β^--emitters as well as external photon irradiation. The cell nucleus is stained with DAPI (blue). Samples treated with α- and β^--emitters were exposed to radionuclides for 4 h and then fixed. External irradiated samples were fixed 30 min post irradiation, which is when the maximum in the γH2AX signal is typically reached. On the right side, the corresponding detected γH2AX foci number (colored curves, left y-axis) and total γH2AX intensity (dashed gray curves, right y-axis) are exemplified for one cell line (C4-2, PSMA-positive).

5.1.2 Comparison of three α-emitters: ^{225}Ac, ^{227}Th and ^{223}Ra

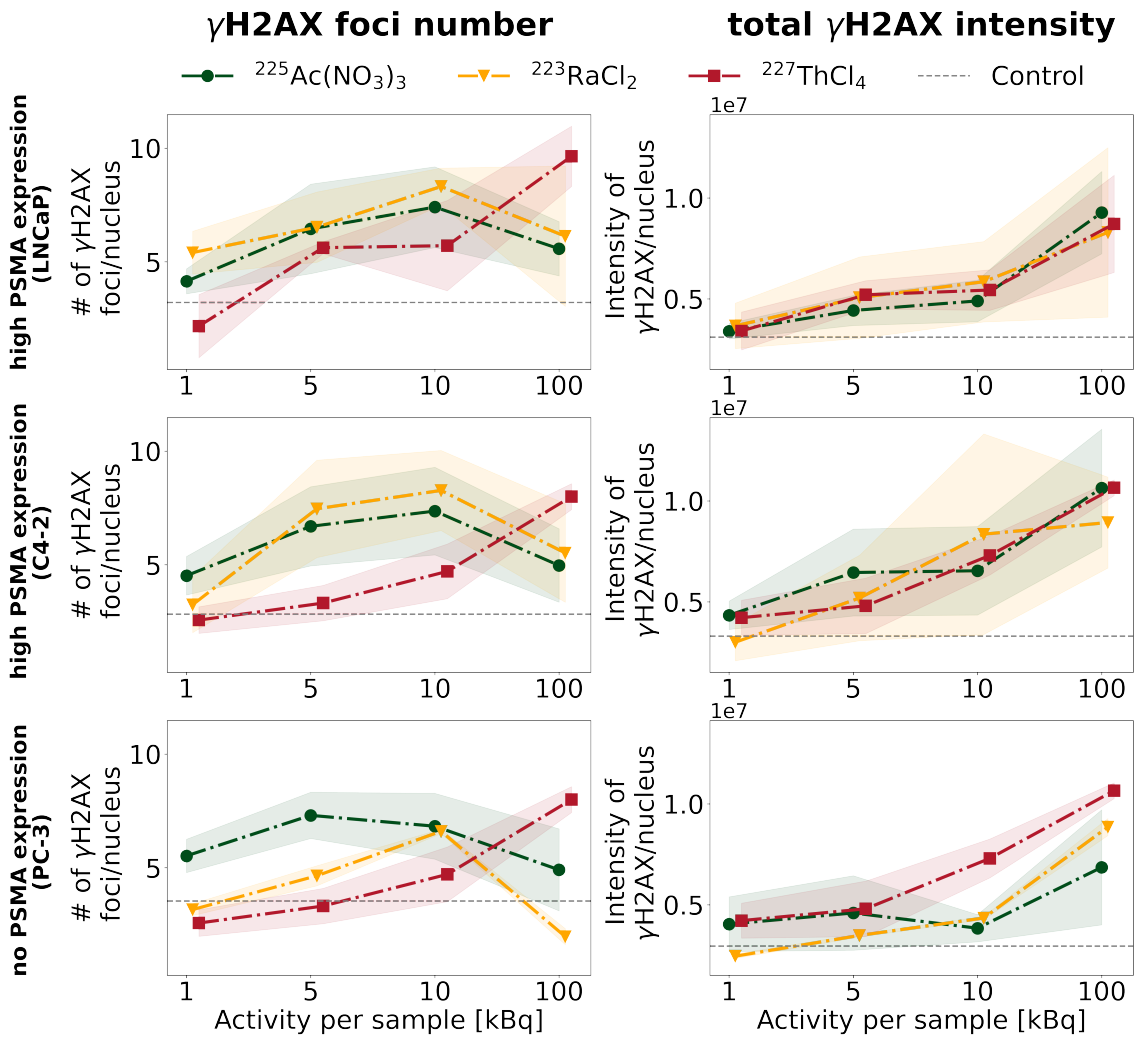

Figure 5.2: **Comparison of three α-emitters: ^{225}Ac, ^{227}Th and ^{223}Ra:** all three radionuclides were used in their non-complexed form, notably $^{225}Ac(NO_3)_3$, $^{227}ThCl_4$ and $^{223}RaCl_2$. Cells were exposed to the radionuclides for 4 h with direct fixation. Mean number of detected γH2AX foci (upper row) and intensity of total γH2AX signal (lower row) are displayed. The intensity of the total γH2AX signal is most relevant for the highest activity of 100 kBq, where the separation of single foci is failing in the analysis process. The assay could not be performed with ^{227}Th on the PC-3 cell line (PSMA-negative), due to the sudden non-availability of this radionuclide.

The DNA damage assay was conducted with three different α-emitters, ^{225}Ac, ^{227}Th and ^{223}Ra, the latter being the daughter nuclide of ^{227}Th. The properties of these radionuclides are listed in Table 2.1. Notably, their half-lifes and mean α-energies fall within a similar range. When comparing the total γH2AX intensity (displayed in the lower row in Figure 5.2), no significant differences were observed between the three radionuclides. This finding is supported by the calculated ratios for the

total γH2AX intensity (^{225}Ac/^{223}Ra, ^{225}Ac/^{227}Th, ^{223}Ra/^{227}Th), which are all close to one (refer to Table 5.1, lower part).
Regarding the detected foci numbers, ^{225}Ac and ^{223}Ra exhibited similar results for PSMA-positive cell lines, LNCaP and C4-2, with ratios around one (^{225}Ac/^{223}Ra ratio: [0.88, 1.06]). However, ^{225}Ac is overcoming ^{223}Ra in PSMA-negative PC-3 cells, particularly at lower activities (^{225}Ac/^{223}Ra ratio: 1.45). Compared to ^{227}Th, ^{225}Ac and ^{223}Ra induced more DNA damage in LNCaP and C4-2 (^{225}Ac/^{227}Th ratio: [1.45, 1.78]; ^{223}Ra/^{227}Th ratio: [1.70, 1.76]). The slight increase in DNA damage observed with ^{223}Ra and ^{225}Ac can be attributed to the decay scheme (Figure 2.7). Specifically, multiple short-lived α-decays occur, leading to a higher frequency of α-particles emitted by ^{223}Ra and ^{225}Ac within the 4 h exposure time compared to ^{227}Th. This may result in increased DNA damage.

Table 5.1: **Comparison of three α-emitters: ^{225}Ac, ^{227}Th and ^{223}Ra:** all three radionuclides were used in their non-complexed form, notably $^{225}Ac(NO_3)_3$, $^{227}ThCl_4$ and $^{223}RaCl_2$. The exposure time was 4 h with direct fixation. The ratio of the different α-emitters to each other was calculated for foci number and total γH2AX intensity within each activity and all cell lines (data corresponds to Figure 5.2). For each cell line and ratio, the mean was calculated across all activities (last column).

		Activity [kBq]				Mean ratio
Foci number	**Ratio**	**1**	**5**	**10**	**100**	(across all activities)
LNCaP	^{225}Ac/^{223}Ra	0.77	0.99	0.89		0.88
	^{225}Ac/^{227}Th	1.91	1.15	1.30		1.45
	^{223}Ra/^{227}Th	2.49	1.16	1.46		1.70
C4-2	^{225}Ac/^{223}Ra	1.39	0.90	0.89		1.06
	^{225}Ac/^{227}Th	1.76	2.02	1.56		1.78
	^{223}Ra/^{227}Th	1.26	2.25	1.76		1.76
PC-3	^{225}Ac/^{223}Ra	1.75	1.57	1.03		1.45
γH2AX Intensity		**1**	**5**	**10**	**100**	
LNCaP	^{225}Ac/^{223}Ra	0.93	0.87	0.84	1.12	0.94
	^{225}Ac/^{227}Th	1.00	0.85	0.90	1.06	0.95
	^{223}Ra/^{227}Th	1.08	0.97	1.08	0.95	1.02
C4-2	^{225}Ac/^{223}Ra	1.45	1.24	0.78	1.19	1.17
	^{225}Ac/^{227}Th	1.03	1.34	0.90	1.00	1.07
	^{223}Ra/^{227}Th	0.71	1.08	1.14	0.84	0.94
PC-3	^{225}Ac/^{223}Ra	1.65	1.32	0.88	0.77	1.16

5.1.3 Impact of Targeting

For ^{225}Ac and ^{177}Lu, PSMA-targeting was performed with the radiopharmaceutical [^{177}Lu]Lu-PSMA-617 and its analogue optimized for ^{225}Ac, [^{225}Ac]Ac-PSMA-716. The PSMA-bound radionuclides were compared to non-complexed and therefore non-targeting radionuclides, $^{177}LuCl_3$ and $^{225}Ac(NO_3)_3$. A further control was introduced by using two PSMA-expressing cell lines, LNCaP and C4-2, as well as a non-PSMA-expressing cell line, PC-3. The results of the experiments with an exposure time of 4 h and direct fixation are shown in Figure 5.3.

Overall, the experiments demonstrated that targeting is only superior to the non-targeted approach, when combined with a short-range α-emitter, ^{225}Ac. In both PSMA-positive cell lines, targeted treatment with [^{225}Ac]Ac-PSMA-716 resulted in significantly more DNA damage than non-targeted treatment, as confirmed by Student's t-test ([^{225}Ac]Ac-PSMA-716/$^{225}Ac(NO_3)_3$ ratio: [1.4, 1.3]). In contrast, for the PSMA-negative cell line PC-3, where no internalization occurs due to lack of target receptor, targeted and non-targeted ^{225}Ac had similar effects on DNA damage ([^{225}Ac]Ac-PSMA-716/$^{225}Ac(NO_3)_3$ ratio: 1.0). However, for the long-range β^--emitter ^{177}Lu, no significant difference was observed between targeted and non-targeted treatment in any of the cell lines ([^{177}Lu]Lu-PSMA-617/$^{177}LuCl_3$ ratio: 0.9). In fact, slightly higher numbers of γH2AX foci were detected for non-targeted $^{177}LuCl_3$, indicating that internalization has no benefit over membrane-bound activity for the long-range β^--emitters. The ratios calculated for induced DNA damage of PSMA-bound to non-targeted treatment are displayed in Table 5.2 for both radionuclides.

Table 5.2: **Effect of PSMA-targeting - direct comparison of PSMA-bound and non-targeted activity:** the number of γH2AX foci was used to calculate a ratio of PSMA-bound/non-targeted for similar activities for both radionuclides. For each cell line, the average ratio was the calculated over all three single ratios

	PSMA-bound / non-targeted					**Mean**
	^{225}Ac [kBq]	1	5	10		
LNCaP		1.8	1.3	1.2		**1.4**
C4-2		1.6	1.3	1.2		**1.3**
PC-3		1.0	0.9	1.2		**1.0**
	^{177}Lu [kBq]	100	500	1000	5000	
LNCaP		1.0	0.7	0.6	1.2	**0.9**
C4-2		0.9	0.7	0.8	1.0	**0.9**
PC-3		0.9	0.7	1.3	0.9	**0.9**

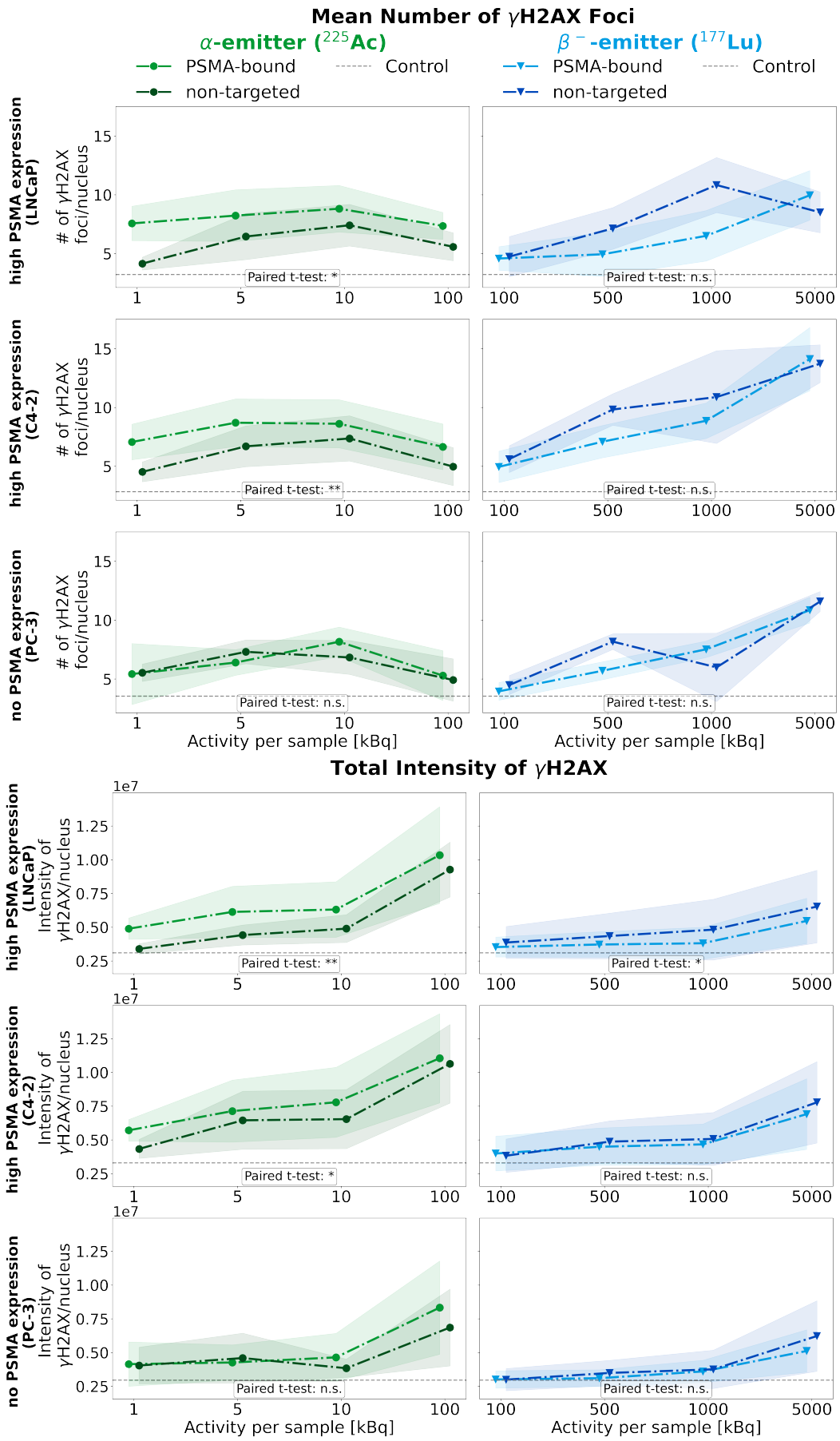

Figure 5.3: **Comparison of PSMA-bound to non-targeted activity with ^{225}Ac and ^{177}Lu:** mean values of repetitions are plotted as a dashed line, accompanied by a light transparent band representing the standard deviation. Significant intervals are denoted by: * = $p < 0.05$, ** = $p < 0.01$, *** = $p < 0.001$. Non-significant results ($p > 0.05$) are indicated as "n.s." (paired Student's t-test).

The DNA damage assessment results are consistent with those from the cell proliferation study (Section 4.3). Notably, no significant difference was observed between targeted [^{177}Lu]Lu-PSMA-617 and non-targeted $^{177}LuCl_3$ treatment with the long-range β^--emitter in all three cell lines (p-value > 0.05, Student's t-test). In contrast, a significant difference was found for the short-range α-emitter ^{225}Ac in the PSMA-positive cell lines (LNCaP and C4-2), confirming that internalized activity enhances the efficacy of ^{225}Ac. Again, no significant difference between targeting and non-targeting was found the PSMA-negative cell line (PC-3), which lacks internalization via PSMA-targeting. The results are presented graphically in Figure 5.5, including significance intervals of the calculated p-values.
Furthermore, when comparing both radionuclides directly to each other, as illustrated in Figure 5.4, the superiority of the α-emitters becomes evident. Even at an activity concentration 500 times higher, the β^--emitter was outperformed by the α-emitter, as the latter is introducing more complex DNA damage and challenging cell proliferation even in the long term. Additionally, a striking difference between the two emitters was observed in the PSMA-negative PC-3 cells, where ^{225}Ac showed a decrease in cell proliferation at high concentrations, whereas ^{177}Lu had no effect on cell proliferation.

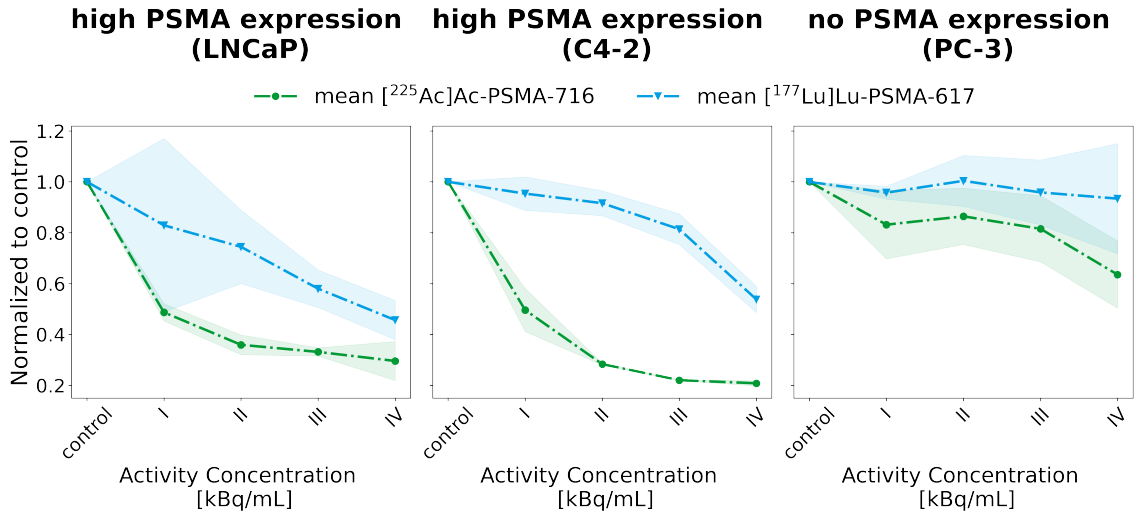

Figure 5.4: **Cell proliferation - direct comparison of [^{225}Ac]Ac-PSMA-716 and [^{177}Lu]Lu-PSMA-617 :** mean values of repetitions are plotted as a dashed line, accompanied by a light transparent band representing the standard deviation. Different activity concentrations were used for both radionuclides specified in Table 4.3. Dose I to IV correspond to ^{225}Ac: [0.156, 0.625, 2.5, 10] and ^{177}Lu: [78.1, 312.5, 1250, 5000] kBq/mL.

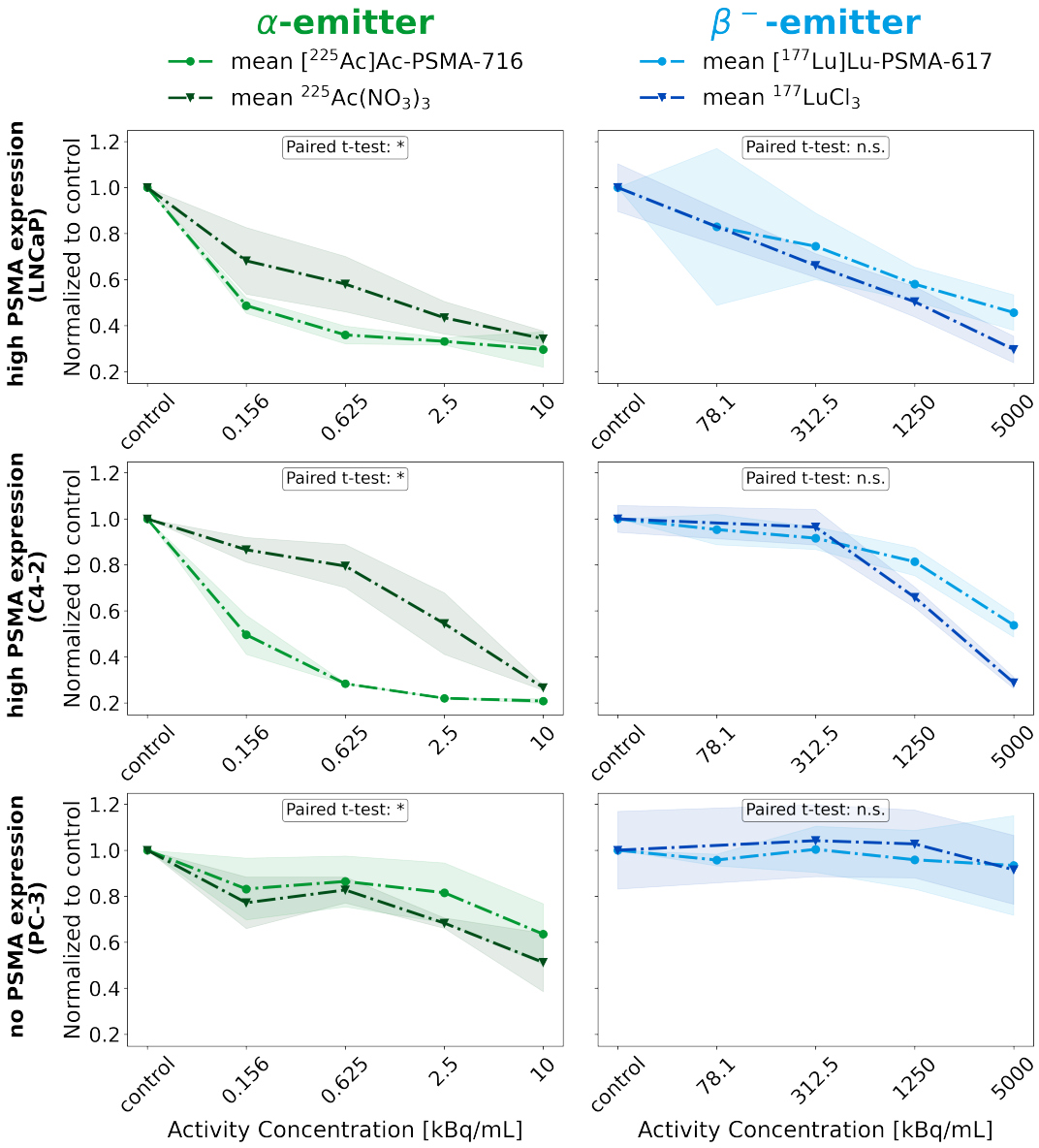

Figure 5.5: **Cell proliferation - comparison of PSMA-bound and non-complexed ^{225}Ac and ^{177}Lu:** mean values of repetitions are plotted as a dashed line, accompanied by a light transparent band representing the standard deviation. Significant intervals are denoted by: * = p < 0.05, ** = p < 0.01, *** = p < 0.001. Non-significant results (p > 0.05) are indicated as "n.s." (paired Student's t-test).

5.1.4 Impact of Activity

A comparison of the activities for each emitter type that yielded comparable numbers of γH2AX foci led to the conclusion that an activity level 100 times higher is required for the β^--emitter ^{177}Lu than for the α-emitter ^{225}Ac. This ratio was consistent across three activity levels of ^{225}Ac (1, 5 and 10 kBq) compared to ^{177}Lu (100,500 and 1000 kBq). A closer examination revealed that within this activity ra-

tio, the α-emitter is more effective than the β^--emitter in PSMA-targeted settings across all three cell lines ([^{225}Ac]Ac-PSMA-716/[^{177}Lu]Lu-PSMA-617 ratio: [1.2-1.6]). In contrast, when comparing the non-targeted treatment at the same activity ratio, $^{177}LuCl_3$ is more effective than $^{225}Ac(NO_3)_3$, with the $^{225}Ac(NO_3)_3/^{177}LuCl_3$ ratio: [0.7; 0.8] for PSMA-positive cell lines. For the PSMA-negative cell line, however, the ratio between both emitter types is 1.1, suggesting that this radioresistant cell line may be more sensitive to α-particles. A comprehensive overview of all individual computed ratios is provided in Table 5.3.

Table 5.3: **Direct comparison of α- and β^--emitters at similar activity ratio:** DNA damage assay results where the activity ratio between ^{225}Ac and ^{177}Lu is 1:100 were compared. The ratio of ^{225}Ac/^{177}Lu based on the number of γH2AX foci was calculated for all activities fulfilling this relation. For each cell line, the average ratio was computed across all individual ratios.

	Ratio 1:100			**Mean**
	^{225}Ac[kBq] /	1	5	10	
	^{177}Lu[kBq]	100	500	1000	
	PSMA-bound				
LNCaP		1.7	1.7	1.4	**1.6**
C4-2		1.4	1.2	1.0	**1.2**
PC-3		1.4	1.1	1.1	**1.2**
	non-targeted				
LNCaP		0.9	0.9	0.7	**0.8**
C4-2		0.8	0.7	0.7	**0.7**
PC-3		1.2	0.9	1.1	**1.1**

Furthermore, whereas the ratio between ^{225}Ac:^{177}Lu for comparable biological outcomes was set at 1:100, it had to be adjusted to 1:500 in the cell proliferation assay, which evaluated a later stage of cellular response. To compare the effectiveness of both emitter types in detail, the ratio of normalized percentages relative to the control was calculated (% ^{225}Ac/ % ^{177}Lu). For a more intuitive representation, the natural logarithm was applied to these values, resulting in negative values if α β^-, positive values if $\alpha < \beta^-$, and values close to zero if the effect was equal. The individual values for each cell line are displayed in Table 5.4.
Overall, at this later biological endpoint, the α-emitter demonstrated a stronger impact on cell proliferation across all cell lines, regardless of whether the treat-

ment was targeted or non-targeted (all ratios < 0). In the case of the targeted treatment, [^{225}Ac]Ac-PSMA-716 proved to be the more effective in both PSMA-positive cell lines (ratio: [-0.56; -1.02]), whereas in the non-targeted setting, the effect of the α-emitter was less pronounced (ratio: [-0.04; -0.15]). Notably, for the PSMA-negative cell line, the α-emitter produced a more significant effect in non-targeted treatment (ratio: -0.41) compared to targeted therapy (ratio: -0.21).

Table 5.4: **Direct comparison of α- and β^--emitters at similar activity ratio in cell proliferation:** for all applied activity concentrations the ratio of ^{225}Ac:^{177}Luis 1:500. To compare the effectiveness of ^{225}Ac to ^{177}Lu on the cell proliferation, the ratio of the normalized values (% ^{225}Ac/ % ^{177}Lu) was calculated. The natural logarithm was applied to the ratio, resulting in negative values if α β^-, positive values if α < β^-, and values close to zero if the effect was equal. Across all four activity pairs (I-IV) with the ratio 1:500, mean values are provided for each treatment and cell line.

	Ratio 1:500	**I**	**II**	**III**	**IV**	**Mean**
	^{225}Ac[kBq/ml] / ^{177}Lu[kBq/ml]	0.156 / 78.1	0.625 / 312.5	2.5 / 1250	10 / 5000	
	PSMA					
LNCaP		-0.53	-0.73	-0.56	-0.43	**-0.56**
C4-2		-0.65	-1.17	-1.31	-0.95	**-1.02**
PC-3		-0.14	-0.15	-0.16	-0.39	**-0.21**
	non-targeted					
LNCaP			-0.13	-0.15	0.15	**-0.04**
C4-2			-0.19	-0.19	-0.08	**-0.15**
PC-3			-0.23	-0.41	-0.58	**-0.41**

Moreover, an interesting comparison can be made by examining how an increase in activity affects the amount of induced DNA damage. The dataset included three different increase factors in activity: doubling (e.g., 5 $\rightarrow$ 10 kBq), fivefold (e.g., 1 $\rightarrow$ 5 kBq) and tenfold (e.g., 1 $\rightarrow$ 10 kBq). For each cell line and radionuclide, ratios of the γH2AX foci numbers were calculated for these three activity increase factors in both targeted and non-targeted treatments. The results are presented in Table 5.5.

Table 5.5: **Impact of increasing the activity of α- and β^--emitters on DNA damage induction:** the dataset included three different increase factors in activity (2, 5, and 10 times). For each cell line and radionuclide combination, the ratio of increase in γH2AX foci was calculated. PSMA-bound: [^{225}Ac]Ac-PSMA-716, [^{177}Lu]Lu-PSMA-617 and non-targeted: $^{225}Ac(NO_3)_3$, $^{177}LuCl_3$

Activity increase factor		**2**	**5**	**10**
^{225}Ac	5→10 kBq		1→5 kBq	1→10 kBq
PSMA-bound				
LNCaP		1.1	1.1	1.2
C4-2		1.0	1.2	1.2
PC-3		1.3	1.2	1.5
non-targeted				
LNCaP		1.1	1.6	1.8
C4-2		1.1	1.5	1.6
PC-3		0.9	1.3	1.2
^{177}Lu	500→1000 kBq		100→500 kBq	100→1000 kBq
PSMA-bound				
LNCaP		1.3	1.1	1.4
C4-2		1.3	1.4	1.8
PC-3		1.3	1.4	1.9
non-targeted				
LNCaP		1.5	1.5	2.3
C4-2		1.1	1.8	1.9
PC-3		0.7	1.8	1.3

In general, an increase in activity led to an increase in DNA damage, with all ratios exceeding one except for the doubling of activity in non-targeted treatment of the PC-3 cell line ($^{225}Ac(NO_3)_3$: 0.9 and $^{177}LuCl_3$: 0.7). However, the magnitude of DNA damage induction did not directly correlate with the magnitude of activity increase. For instance, a tenfold higher activity did not result in a tenfold higher DNA damage induction. The most pronounced increase in DNA damage induction was observed for the tenfold increase with $^{177}LuCl_3$ in LNCaP cells, with a ratio of 2.3. The long-range β^--emitter showed a greater enhancement in DNA damage from increased activity, particularly in PSMA-positive cell lines (LNCaP and C4-2). A tenfold increase in activity resulted in ratios of [1.4; 1.8] for [^{177}Lu]Lu-PSMA-617 versus [1.2; 1.2] for [^{225}Ac]Ac-PSMA-716. In non-targeted treatments, the difference

was even more pronounced, with ratios of tenfold increase [2.3; 1.9] for $^{177}LuCl_3$ and [1.8; 1.6] for $^{225}Ac(NO_3)_3$. In PSMA-negative PC-3 cells, increased activity equally led to a greater increase in DNA damage for ^{177}Lu, both [^{177}Lu]Lu-PSMA-617 (ratio: 1.9) and $^{177}LuCl_3$ (ratio: 1.3), compared to their respective counterparts [^{225}Ac]Ac-PSMA-716 (ratio: 1.5) and $^{225}Ac(NO_3)_3$ (ratio: 1.2). Notably, the benefit of increased activity was more pronounced in PSMA-bound activity for PC-3 cells, whereas the opposite was observed in PSMA-positive cell lines.

5.1.5 Impact of Exposure Time

To assess the impact of exposure time on DNA damage, samples were exposed to radionuclides for either 1 h or 4 h, followed by fixation at the end of the exposure period. To compare the effects of the exposure time within an equal time for biological processes, samples were given 3 h of recovery time after 1 h exposure, resulting in a total treatment observation time of 4 h. Since DNA repair occurs concurrently with DNA damage induction during radionuclide treatment, this consideration is crucial. The mean number of γH2AX foci detected in each sample is visualized in Figure 5.6. Comparing the 1 h time point to the 1 h (+ 3 h) time point, an increase in DNA damage is observed for both emitter types at the later time point with additional recovery time. This increase in DNA damage could be attributed to two effects. Firstly, delayed biological response in DNA damage repair signaling due to continuous exposure may lead to underestimation of DNA damage at the earlier time point compared to the later time point with recovery time. For instance, DNA damage occurring at the end of the 1 h exposure period, is not marked by γH2AX in directly fixated samples. Secondly, low amounts of residual activity, either membrane-bound or internalized, which was not fully removed by media change, could cause further DNA damage during the recovery period. In Table 5.6, the ratio of γH2AX foci numbers of 4 to 1 h is presented for each radionuclide treatment, activity, and cell line.

Table 5.6: **Influence of exposure time on DNA damage induction by α- and β^--emitters:** the ratio (4h : 1h) of detected number of γH2AX foci is calculated between the two exposure times for each activity. Mean ratios are computed across all cell lines as well as specifically within PSMA-positive cell lines (LNCaP and C4-2).

	Ratio (4h/1h)	LNCaP	C4-2	PC-3	Mean ratio	Mean ratio (PSMA+)
[^{225}Ac]Ac-PSMA-716	5kBq	1.55	1.45	1.5	**1.50**	**1.50**
	10kBq	1.31	1.17	1.26	**1.25**	**1.24**
[^{177}Lu]Lu-PSMA-617	500 kBq	1.15	1.71	1.93	**1.60**	**1.43**
	1000 kBq	2.07	1.96	1.96	**2.00**	**2.02**
$^{225}Ac(NO_3)_3$	5kBq	1.59	1.35	1.37	**1.44**	**1.47**
	10kBq	1.31	1.32	1.43	**1.35**	**1.32**
$^{177}LuCl_3$	500 kBq	1.22	1.89	2.19	**1.77**	**1.56**
	1000 kBq	2.02	1.63	1.66	**1.77**	**1.83**

Generally, longer exposure times resulted in increased levels of DNA damage across all cell lines. However, both parameters do not correlate linearly. Specifically, the fourfold increase in exposure time resulted in a maximum twofold increase in DNA damage (4h/1h ratio [^{177}Lu]Lu-PSMA-617: 2.02). For the α-emitter ^{225}Ac, the increased exposure time had a more pronounced effect at lower activities of 5 kBq (4h/1h ratio [^{225}Ac]Ac-PSMA-716: 1.50; $^{225}Ac(NO_3)_3$: 1.47). The higher activity of 10 kBq only led to a moderate increase (4h/1h ratio [^{225}Ac]Ac-PSMA-716: 1.24; $^{225}Ac(NO_3)_3$: 1.32). In contrast, the β^--emitter ^{177}Lu, exhibited a larger impact of the prolonged exposure time at higher activities of 1000 kBq (4h/1h ratio [^{177}Lu]Lu-PSMA-617: 2.02; $^{177}LuCl_3$: 1.83) compared to lower activities of 500 kBq (4h/1h ratio [^{177}Lu]Lu-PSMA-617: 1.43; $^{177}LuCl_3$: 1.56). Overall, prolonged exposure times amplified the induction of DNA damage more substantially for the β^--emitter than the α-emitter.

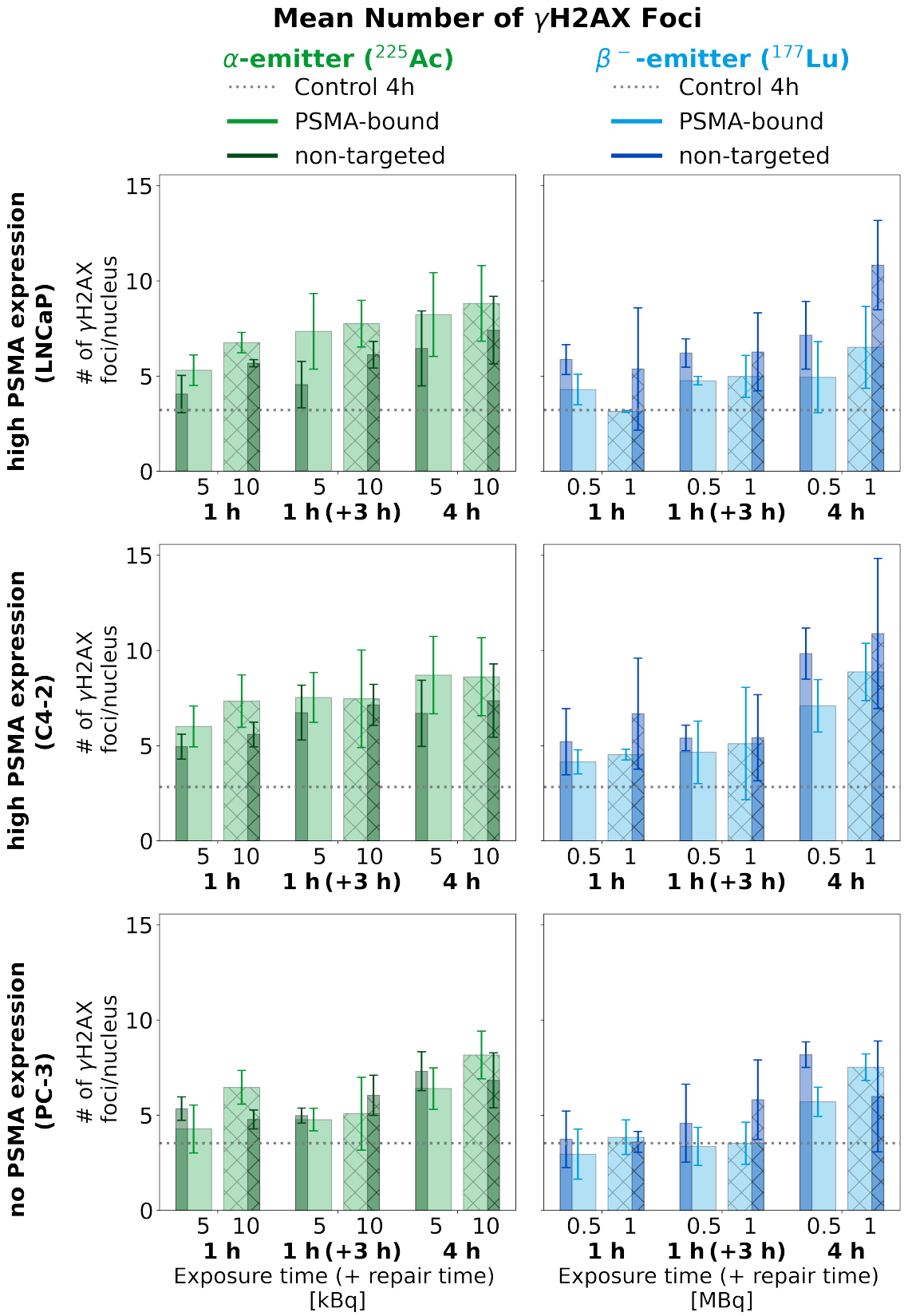

Figure 5.6: **Influence of exposure time on DNA damage induction by α- and β^--emitters:** the number of γH2AX foci detected is plotted in a bar chart against three observation time points: the two different exposure times 1 and 4 h as well as 1 h (+ 3 h recovery time) allowing for equal time for biological processes to initiate repair, comparable to the 4 h sample. Standard deviations are displayed as error bars on top of each bar.

5.2 Development of a Geant4-DNA Simulation for Single-Cell Dosimetry

In the preceding section, the impact of different activities and exposure times on the biological outcome was investigated. To induce a similar biological effectiveness with β^--emitters as with α-emitters, an increase in activity by a factor of 100 was necessary in the DNA damage assay and even a factor of 500 in the cell proliferation assay. Experiments using external photon irradiation as a gold standard revealed that the induced DNA damage falls within the range of 1.0 Gy to 2.5 Gy. However, directly comparing the biological effectiveness of different radiation types, various activities, and length of exposure time is complex due to their distinct characteristics. To facilitate a more comprehensive comparison, it would be advantageous to consider the deposited energy or absorbed dose as a common physical parameter for the induced effect. Unfortunately, experimental determination of this quantity is highly challenging in the context of TRT. Therefore, this section focuses on the development of a Monte Carlo simulation to estimate the deposited energy within the cell nucleus under various experimental conditions using a single-cell model.
Especially for the short-range α-emitters, the precise localization of radionuclides is a crucial factor in accurately simulating energy deposition within the nucleus as demonstrated by comparing the effects of targeted versus non-targeted α-emitters in Subsection 5.1.3. Consequently, to ensure simulation accuracy, it is essential to determine first the experimental radionuclide distribution, which will serve as input data. The results are presented in Subsection 5.2.1. The subsequent subsections then describe the design of a basic single-cell simulation (Subsection 5.2.2) and its further refinement (Subsection 5.2.3).

5.2.1 Experimental Determination of Radionuclide Distribution

To establish a baseline for the radionuclide distribution, which will serve as input for the initial simulation, cellular uptake assays were performed (methodology described in Subsection 4.2.3). The behavior of non-complexed activity $^{225}Ac(NO_3)_3$, complexed activity [^{225}Ac]Ac-DOTA and PSMA-bound activity [^{225}Ac]Ac-PSMA-I&T, was studied on receptor-expressing and non-expressing cell lines. Similar studies were conducted with ^{177}Lu, to compare [^{177}Lu]Lu-PSMA-617 and $^{177}LuCl_3$. Representative results from a cellular uptake assay with ^{225}Ac are shown in Figure 5.7.

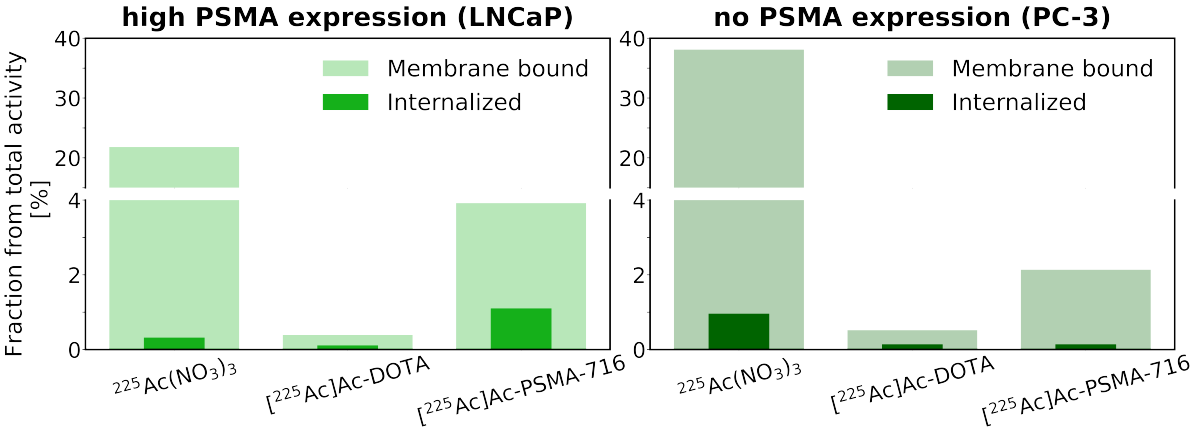

Figure 5.7: **Cellular uptake study with ^{225}Ac:** membrane-bound and internalized fraction of the PSMA-positive LNCaP and the PSMA-negative PC-3 cell line are depicted for non-complexed activity $^{225}Ac(NO_3)_3$, DOTA-chelated activity [^{225}Ac]Ac-DOTA, and PSMA-bound activity [^{225}Ac]Ac-PSMA-716. The percentage of fraction is calculated from the total activity applied during the assay (10 kBq per sample during 4 h incubation time).

A general trend observed in this study was increased internalization of PSMA-labeled compounds with longer incubation times in PSMA-positive cell lines (e.g., for [^{225}Ac]Ac-PSMA-716 1 h: 15.82% (0.49%) and 4 h: 21.92% (1.11%) internalization from total applied activity; values in brackets represent percentage relative to total bound activity). The most notable observation was the behavior of non-complexed activity, which exhibited a high degree of unspecific binding to the cellular membrane in all cell lines tested for both radionuclides, ^{225}Ac and ^{177}Lu. For instance, $^{225}Ac(NO_3)_3$ was reaching 21.81% of membrane-bound activity in LNCaP cells and 35.79% in PC-3 cells after 4 h incubation time. In particular, the unspecific membrane binding is much higher than the specific membrane binding to the PSMA receptor with labeled activity [^{225}Ac]Ac-PSMA-716, with a 5.5-fold difference between [^{225}Ac]Ac-PSMA-716 (3.94%) and $^{225}Ac(NO_3)_3$ (21.81%) at 4 h. Furthermore, non-complexed activity also exhibited some degree of internalization in PSMA-negative PC-3 cells, albeit at a relatively low level. Specifically, 0.9% of the applied activity was internalized after 4 h. However, by chelating the activity with the DOTA chelator the unspecific binding could be significantly reduced, thereby reducing the charge-mediated binding of free ions ($^{225}Ac^{3+}$): [^{225}Ac]Ac-DOTA, 0.39% (4 h, LNCaP), 0.52% (4 h, PC-3). Notably, similar behavior was observed for $^{177}LuCl_3$, suggesting that this phenomenon is not unique to non-complexed ^{225}Ac.

Suitable input for the single-cell simulation can be obtained by estimating the number of radionuclides per cell. The initial activity A_0 at the start of incubation can be related to the initial number of radionuclides N_0 : $A_0 = \lambda N_0$ using equa-

tion 2.5. An estimate of N_0 can be calculated based on the known total activity values, with the decay constants λ specific to each radionuclide being taken into account. The estimated number of cells per sample, derived from the seeding concentration, is then used to divide N_0, resulting in an approximation of the number of radionuclides per cell. Furthermore, the number of radionuclides located on the membrane and inside the cell are calculated by using the percentages of membrane-bound and internalized activity relative to total activity. Approximate values for these estimates are presented in Table 5.7.

Table 5.7: **Estimated number of radionuclides per single cell:** calculated numbers of total radionuclides (Tot.) based on total applied activity based from cellular uptake assay results. Exemplary values are provided for two scenarios: PSMA-bound activity, characterized by 4% membrane binding (Mem.) and 1.1% internalization (Int.), and non-targeted activity, which exhibited unspecific membrane binding of 35% and 0.9% internalization.

Nuclides per cell:	Tot.			
α**-emitter [**kBq]	**1**	**5**	**10**	**100**
^{225}Ac	26	129	258	2576
^{227}Th	49	243	486	4855
^{223}Ra	30	148	2968	
β^-**-emitter [**kBq]	**100**	**500**	**1000**	**5000**
^{177}Lu	1725	8627	17254	86271

Nuclides per cell:	Mem. (4%)	Int. (1.1%)	**PSMA-bound activity**					
α**-emitter [**kBq]	**1**		**5**		**10**		**100**	
^{225}Ac	1	0	5	1	10	3	103	28
^{227}Th	2	1	10	3	19	5	194	53
^{223}Ra	1	0	6	2	12	3	119	33
β^-**-emitter [**kBq]	**100**		**500**		**1000**		**5000**	
^{177}Lu	69	19	345	95	690	190	3451	949

Nuclides per cell:	Mem. (35%)	Int. (0.9%)	**non-targeted activity**					
α**-emitter [**kBq]	**1**		**5**		**10**		**100**	
^{225}Ac	9	0	45	1	90	2	902	23
^{227}Th	17	0	85	2	170	4	1699	44
^{223}Ra	10	0	52	1	104	3	1039	27
β^-**-emitter [**kBq]	**100**		**500**		**1000**		**5000**	
^{177}Lu	604	16	3019	78	6039	155	30195	776

5.2.2 Design of Single-Cell Simulation to Determine Deposited Energy in Nucleus

In the first step, a simplified single-cell model was developed using the *svalue* example provided in GEANT4 DNA. The example was modified by adapting the geometry to represent a single cell. Furthermore, the particle source was designed to produce particles that are randomly located in the cytoplasm or on the membrane surface. The source particles can be varied to resemble the properties of the used radionuclides, with α-particles for ^{225}Ac, ^{227}Th, ^{223}Ra and e^- for β^--emitter ^{177}Lu. The energy of the α-particles can also be varied to match the properties of specific radionuclides. As an approximation for the various α-particles in the decay chain of the different radionuclides, the energy can be set to the mean α-energy of 6.3 MeV to 6.9 MeV calculated in the Table 2.1.
The simulation geometry consists of two ellipsoid volumes: one representing the outer cellular dimensions, encompassing the cell membrane and cytoplasm, and the other representing the cell nucleus, positioned at the center of the cell volume. Currently, the dimensions are set to 14.0×2.5×14.0 µm for the cell volume (green) and 7.1×2.5×7.1 µm for the nucleus volume (blue). The dimensions are based on previous works from Jalalvand et al. who assessed early DNA damage induced by four different radionuclides ^{177}Lu, ^{90}Y, ^{125}I and ^{131}I in a single-cell model [110]. They can be easily adapted to match the specific cells used in experiments, which can be determined using microscopy techniques, e.g., confocal microscope [109]. A graphical representation of the simulation geometry is illustrated in Figure 5.8. The α-particle tracks were simulated for three distinct energy ranges: 0.1, 1 and 5 MeV. It is notable that the range of α-particles depends significantly on their energy. An α-particle with an energy of 5 MeV appears capable of reaching the nucleus even when located at the cell membrane and not internalized by the cell. Moreover, cross-irradiation to neighboring cells is feasible at this energy level. These findings highlight the clinical potential of the studied α-emitting radionuclides, which all emit α-particles with an energy around 5 MeV.

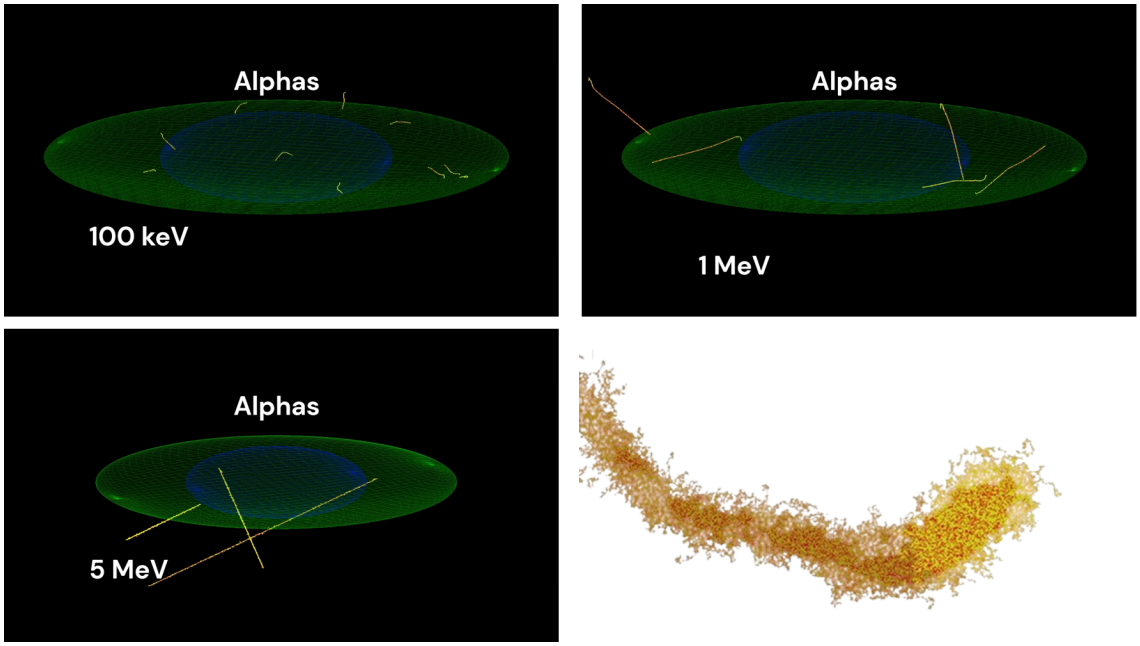

Figure 5.8: **Geometry of single-cell simulation:** geometry of a single cell is simplified as an ellipsoid with cytoplasm (green): 14.0×2.5×14.0 µm and nucleus (blue): 7.1×2.5×7.1 µm. The α-particle tracks (depicted in yellow) with different energies (0.1, 1 and 5 MeV) are simulated with a particle source localized randomly in the cytoplasm. In the right corner, a zoom-in of an α-particle track structure is shown. Tracks consist of many ionization events and cascade production of secondary particles, mainly electrons.

5.2.3 Further Modifications in the Single-Cell Simulation for Absorbed Dose

Accurate simulation of the absorbed dose under various experimental conditions can be achieved through several steps. The following sections provide an elaboration of four key modifications that are necessary for enhancing the simulation and aligning it with experimental observations.

- Track deposited energy in nucleus volume
- Tailor geometry dimensions to actual cell dimensions
- Replace particle source with radionuclide
- Adapt source distribution to experimental values

The next step in simulating the absorbed dose under different experimental conditions involves determining the deposited energy in the nucleus volume. For this purpose, a detector must be defined for the nucleus volume, which tracks

all deposited energy from particle interactions within that volume. To increase accuracy, the dimensions of the geometry should be tailored to match the actual dimensions of the cells used in the experimental setup.
Furthermore, a more accurate approach involves incorporating an actual radionuclide as the source into the simulation, rather than relying on an approximation of α-particles with mean energy. The Geant4 Radioactive Decay Module can be employed for this purpose, allowing a complete decay chain to be simulated within a specified sampling time window [118]. During this decay, emissions such as α-particles are generated and can then be used as input for the single-cell simulation. Promising results have been demonstrated with this approach in other simulation frameworks, such as the simulation of absorbed dose and DNA damage profile of the α-emitter ^{211}At [119].
Moreover, a more realistic representation of the experimental conditions determined by the cellular uptake assay can be achieved through modifications to the implementation of the primary particles generator (gun), which defines and injects particles with specified properties such as energy and momentum direction into the simulation. Currently, the gun position within the defined geometry changes randomly after each simulated particle to coordinates located in the cytoplasm. However, this implementation should be modified to enable the random simulation of the experimentally deduced radionuclide distribution, specifically by having a defined number of events (simulated particles) on the cell membrane, representing the membrane-bound activity, and another number situated within the cytoplasm, representing the internalized activity fraction. For instance, in the case of 5 kBq of [^{225}Ac]Ac-PSMA-716 , this would involve simulating five radionuclides that are randomly distributed at the membrane and one radionuclide that is randomly located within the cytoplasm. The current setup allows for only one particle to be simulated at any given time point.
Once all components have been properly set up, the simulation should be run with sufficient statistical power to capture the behavior of all relevant parameters, including different radionuclides and activities used in the experimental setting. This comprehensive approach will provide valuable insights into the distribution of deposited energy within different experimental conditions, paving the way for a detailed analysis of the effects of various emitter types. Furthermore, this comprehensive framework enables a more profound understanding of the effects exerted by radionuclide localization on the energy deposition and biological outcome.

5.3 DNA Damage Evolution at Late Time Points - Repair and Persistent DNA Damage

This section provides an in-depth analysis of the characteristics of γH2AX foci, such as size and intensity, which can offer insights into DNA damage structure and complexity. A comparison of the effects of different radiation types on γH2AX foci is presented Subsection 5.3.1. Furthermore, examining the γH2AX signal at later post-treatment time points (up to 24, 48, and 72 h) can provide valuable information on how cells respond to and repair induced DNA damage. Generally, simple DNA damage is expected to be repaired within 24 h, whereas more complex damage may require longer periods of time. If the number of γH2AX foci remains elevated even at later times, this suggests persistent DNA damage, which is likely to be complex and difficult to repair. Therefore, Subsection 5.3.2 presents a detailed analysis of the differences in the γH2AX signal between early and late time points.

5.3.1 γH2AX Foci Characteristics of Different Radiation Types

As a first step towards understanding the γH2AX signal, an examination of the specific properties and differences of the γH2AX foci induced by various types of radiation is conducted. The focus is initially placed on the early time point at 4 h post-radiation exposure to investigate the characteristics of the damage sites before they are altered by DNA repair processes. Figure 5.9 presents exemplary immunofluorescent microscopy images of the three radiation types at a specific activity/dose alongside a graphical representation of the γH2AX foci area (left y-axis) and foci intensity (right y-axis). Visually, the foci in the α-emitter samples are larger and brighter. In certain images (e.g., first picture, first row), the track of an α-particle can be identified by closely spaced γH2AX foci arranged along a straight line or curve. However, due to the experimental setup, where the activity was placed in the medium above the monolayer of cells and the microscopy provided a 2D projection of the cell layer, α-particle tracks are only visible in some cells when their trajectory happened to be parallel to the plane of observation. In contrast, the foci of β^--emitter and external photon irradiation resemble each other visually. They are smaller and less bright than the α-induced foci, but more numerous per nucleus. These observations are confirmed by the graphical representation, which shows that the γH2AX foci area of the α-induced damage sites damage sites exceeds the control line, while the area of foci induced by β^--particles or external photon irradiation falls below it. The intensity of foci induced by radionuclides

is found to be generally higher than that of foci from external photon irradiation. Additionally, it is observed that α-particle induced foci exhibit the highest intensity.

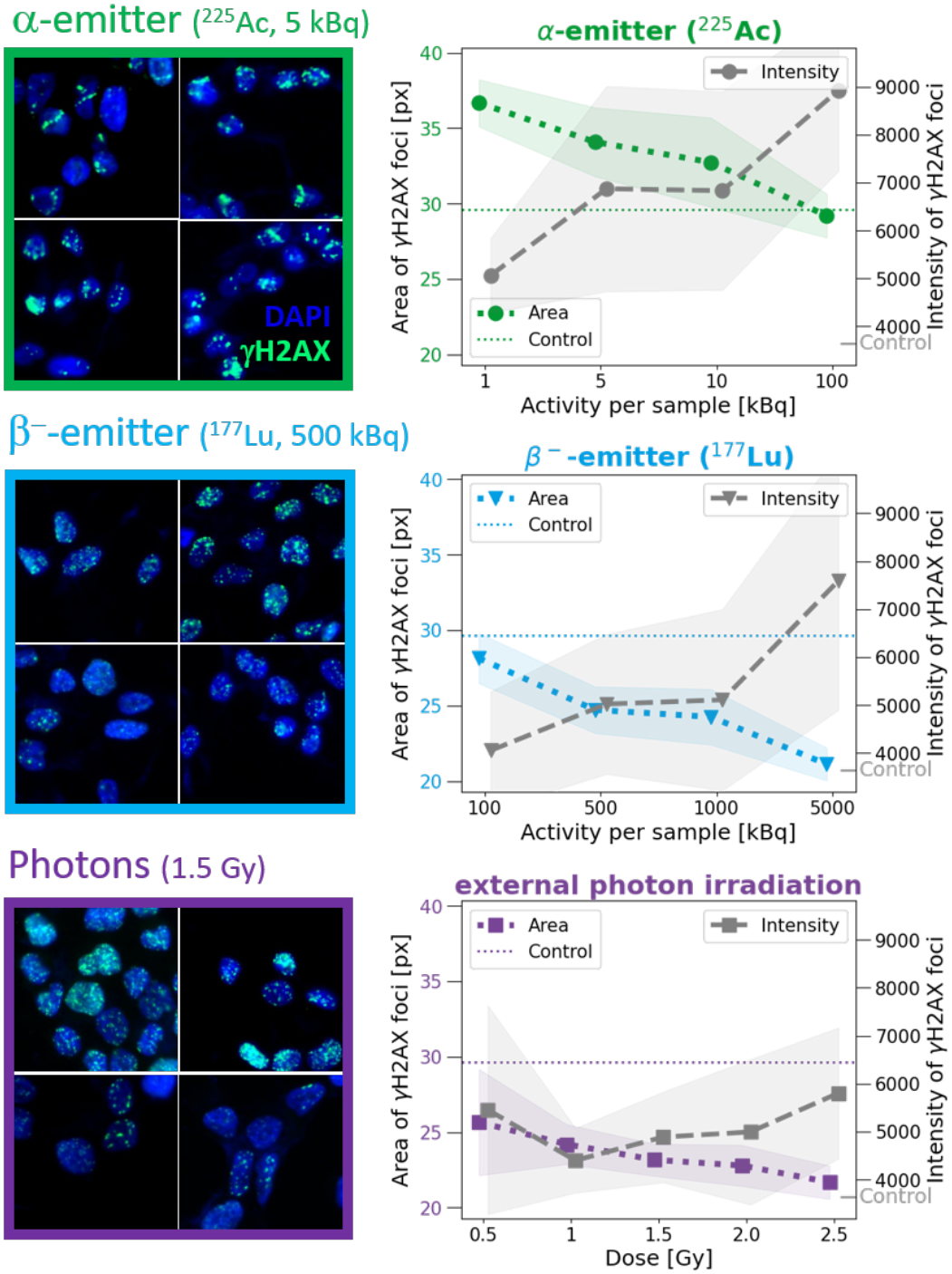

Figure 5.9: **Characteristics of γH2AX foci - area and intensity:** representative immunofluorescent microscope images for γH2AX foci characteristics for the different radiation types and graphical representation of foci area (left y-axis, colored curves) and foci intensity (right y-axis, gray curves) are displayed at the 4 h time point for TRT and 30 min for external photon irradiation (exemplified using cell line C4-2). The standard deviation, representing variability across multiple experimental repetitions, is illustrated by a transparent band surrounding the mean values of the dashed curves.

The average values across all the cell lines of γH2AX foci area and intensity for each radiation type, are presented in Table 5.8 and graphically for all cell lines individually in Figure 5.10. A general trend is observed across all radiation types, where the foci area decreases as activity or dose increases. Notably, while the foci area decreases with increasing dose in externally irradiated samples at the 30 min time point, it remains relatively constant across doses at the later 4 h for each cell line. Comparing the foci sizes induced by different radiation types reveals that those caused by external photon irradiation and β^--particles fall within a similar size range (21-27 px), which is smaller than the control samples (29 px). In contrast, foci induced by α-particles are larger than the control foci at lower activities (1 kBq to 10 kBq), with sizes ranging from (31-34 px). However, at the highest activity of 100 kBq, the size of α-particle-induced foci is comparable to that of the control samples (27-29 px).

Table 5.8: **Average γH2AX foci areas and intensities at 4 h time point:** ranges of mean foci area and intensity are provided across the three cell lines (LNCaP, C4-2, PC-3) for the three lower activities and all doses. The values for the highest activity are presented in a separate column. The area and intensity of the highest activity are given separately. The area of γH2AX foci induced by external photon irradiation at the later time point of 4 h was found to be constant across all doses, with minimal variation ($\pm$ 1), for each of the three cell lines (LNCaP/ C4-2/ PC-3) individually.

	Foci Area [px]	**Foci Intensity**
control	29	3400
^{225}Ac	31-34	4400-7000
^{225}Ac [100 kBq]	27-29	6500-9400
^{177}Lu	26-29	3600-4700
^{177}Lu [5 MBq]	21-23	5500-7500
photon [30 min]	21-27	4000-5800
photon [4 h]	24/26/28	3600-4500

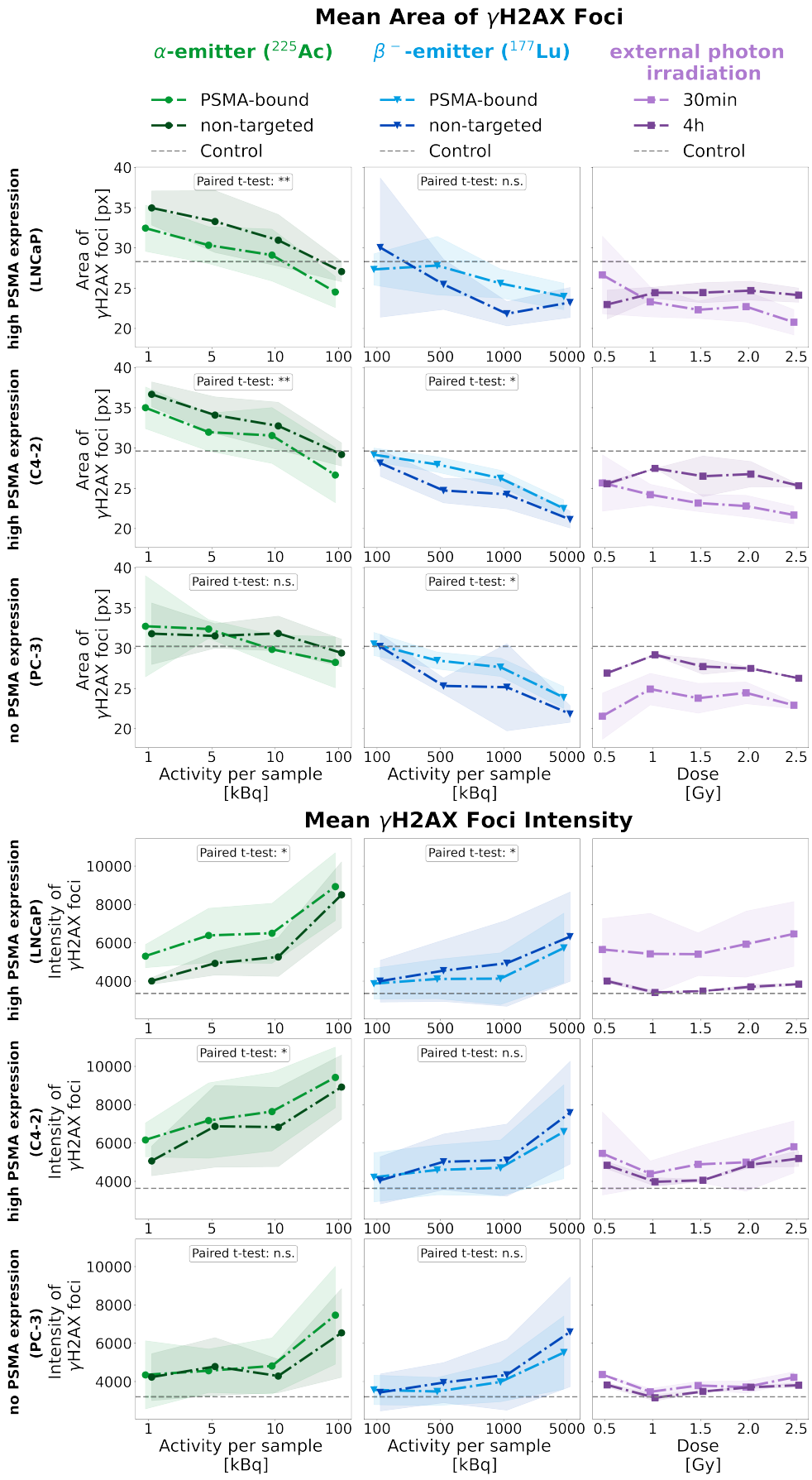

Figure 5.10: **Area and intensity of γH2AX foci at early time point:** the area of γH2AX foci at 4 h after exposure to radionuclides, as well as 30 min after external photon irradiation, is depicted in the upper graph. The corresponding γH2AX intensity is displayed in the lower graph. The standard deviation, representing variability across multiple experimental repetitions, is illustrated by a transparent band surrounding the mean values of the dashed curves.

In contrast to the foci area, the foci intensity exhibits an inverse behavior, generally increasing with rising activity or dose. Comparing the different radiation types, the intensity of the α-particle induced foci is the highest, followed by the β^--particles and external photon irradiation. While in the α-emitter treated samples, the targeted activity induced brighter foci than the non-targeted treatment, for the β^--emitter treated samples the opposite is true, with slightly more intense foci observed in the non-targeted treatment. Overall, the intensity of the foci induced by non-targeted treatment of α-emitters is in the same range as both treatments with the β^--emitter. For the external photon irradiation, the intensity is higher in the shorter time point at 30 min than in the 4 h time point, where it has already decreased nearly to control levels for some cell lines. Comparing the three cell lines, it is noticeable that the foci detected in the C4-2 cell line are the brightest, and the ones in the PC-3 cell line are the darkest. At the highest activities, the intensity has increased by a factor of 2.0-2.8 in ^{225}Ac treated samples and 1.6-2.2 for ^{177}Lu treated samples compared to the intensity level of the control.

5.3.2 γH2AX Signal at Later Time Points - DNA Damage Repair

To gain further insight into the differences in biological effectiveness of α- and β^--emitters, the γH2AX signal was examined at later time points after treatment (up to 72 h). This allowed cells to repair induced DNA damage and provided insights into the repair process. For external photon irradiation, which serves as a gold standard, it is known that most of the DNA damage induced by the moderate doses used in this experimental setup should be repaired within approximately 24 h. This was confirmed as well in the used prostate cancer cell lines, as depicted in Figure 5.11. While the number of induced foci remained constant at early time points (30 min and 4 h), it decreased to control levels in LNCaP and C4-2 for all doses. In contrast, a constant number of foci is observed across all doses at late time points in PC-3 cells, but with a slight increase compared to control levels (24 h: [3.4-6.8] and 48 h: [4.9-5.7]).

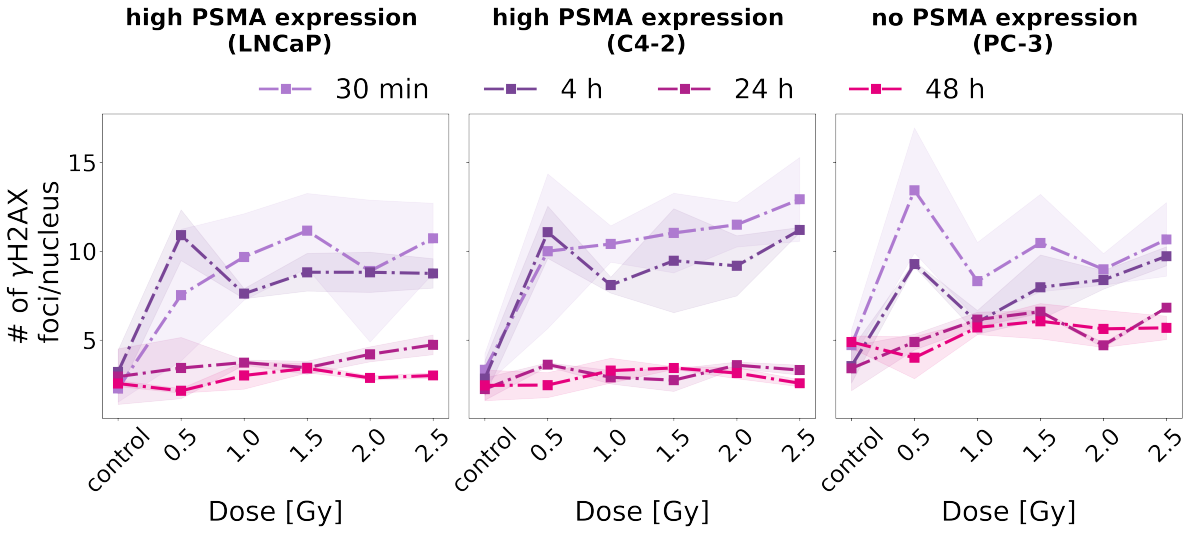

Figure 5.11: **γH2AX foci number at different time points after external photon irradiation treatment:** for all four time points, the foci number is depicted for the five doses and the untreated control. The standard deviation, representing variability across multiple experimental repetitions, is illustrated by a transparent band surrounding the mean values of the dashed curves.

The following analysis compares the three parameters - γH2AX foci number, foci area and foci intensity - between the three radiation types for all time points.

γH2AX Foci Number

In Figure 5.12 (α-emitter) and 5.13 (β^--emitter and external photon irradiation), the detected γH2AX foci number is normalized by subtracting the number of foci found in the corresponding control samples. The plotted values are absolute foci numbers per sample, subtracted by the number of foci in the corresponding control time point. This normalization enables visualization of whether the number of foci dropped back to the control level at later time points or if DNA damage persists. At first glance, it is evident that for neither exposure time (1 or 4 h), the number of γH2AX foci decreased in the samples treated with targeted α-emitters ([^{225}Ac]Ac-PSMA-716, light green). Even at the latest time point of 72 h, for both exposure times and two activities (5 or 10 kBq), the number of foci remained elevated, ranging from 7.7 - 9.7 total number foci/nuclei in PSMA-positive cells. The number of foci is slightly lower for the non-PSMA expressing cell line, PC-3, which lacks the additive effect of targeted treatment. Nonetheless, DNA damage persists at a constant level above baseline in this cell line as well at late time points (6.7-7.9 total number of foci/nuclei). In contrast, the behavior of non-targeted

activity ($^{225}Ac(NO_3)_3$) is less consistent, with DNA damage occasionally decreasing at some intermediate observation time points (such as 48 h) for lower activity and exposure time, only to increase again at the latest time point (72 h).
Upon examination of the results from β^--emitter treated samples, a pattern is emerging that exhibits similarities to the one observed in samples treated with external irradiation. By 24 h, DNA damage has decreased in all three cell lines. The decrease is less pronounced for the non-targeted treatment, which also corresponds to the overall higher number of DNA damage induced with the non-targeted activity ($^{177}LuCl_3$). The magnitude of DNA damage induced by the shorter exposure time of 1 h is lower compared to the longer exposure time of 4 h, resulting in a less pronounced decrease at later time points. Notably, the PC-3 cell line is the least affected by treatment, with DNA damage after 1 h exposure time yielding levels of DNA damage nearly equal to baseline of control at all time points.

γH2AX Foci Area

The foci area across all time points is depicted in Figure 5.14 for the α-emitter and in Figure 5.15 for β^--emitter and external photon irradiation. As discussed previously for the 4 h time point, it is observed that the area of foci induced by α-particles tends to be larger than the area induced by β^--particles and external photon radiation. Furthermore, the area of the α-particle-induced foci is found to be larger than that of control foci, whereas the area for β^--particles and external photon irradiation is smaller than that of the control foci (refer to Subsection 5.3.1).
Upon comparison of all samples, it is noticeable that the area of α-particle-induced foci is slightly larger after the shorter exposure time of 1 h compared to a longer exposure time of 4 h. Although, at the 4 h time point, the foci with the shorter exposure time but similar biological time are found to have reached a size similar to that of the 4 h exposure time and direct fixation. Examining the same time points for the β^--particle treated sample, the samples with shorter exposure time but equal biological time show a slightly larger area, for C4-2 and PC-3, while for LNCaP, the area is slightly decreased at shorter exposure time.
At the late time points, the foci area is found to stabilize around a value specific to each cell line (26/30/32 - LNCaP/C4-2/PC-3). In contrast, while for the external radiation-treated samples a stabilization of the foci area at the 4 h time point across all doses was observed (24/26/28 - LNCaP/C4-2/PC-3), the foci area

increased for the later time point of 48 h to 31/39/30 for all three cell lines. This behavior is contrary to the decrease in foci size observed in early time points (1 h to 4 h) and the decrease observed in foci area in radionuclide-treated samples.

γH2AX Foci Intensity

The results for the foci intensity are again normalized by the value of the control for all individual time points and displayed in Figure 5.16 for the α-emitter and in Figure 5.17 for the β^--emitter and external photon irradiation. For the foci induced by α-particles, which remained constantly high in number, a high level of foci intensity is maintained throughout all time points. In LNCaP cells, an increase in intensity to around 6000-7000 is observed at late time points, compared to intensity values around 4500 at early time points. The intensity for the C4-2 cell lines was already above 6000 at earlier time points and remained at that level for later time points as well. As previously noted, foci intensity was consistently found to be the lowest in PC-3 cells, a trend that continued at late time points. Nevertheless, the level remains significantly above the control level, around 4500.
In alignment with observations regarding the number of foci, a different behavior is observed for β^--emitter and external photon irradiated samples. Here, a decrease in foci intensity is seen at later time points. For almost all late time points and both types of irradiation, the foci intensity drops close to or below the control level.

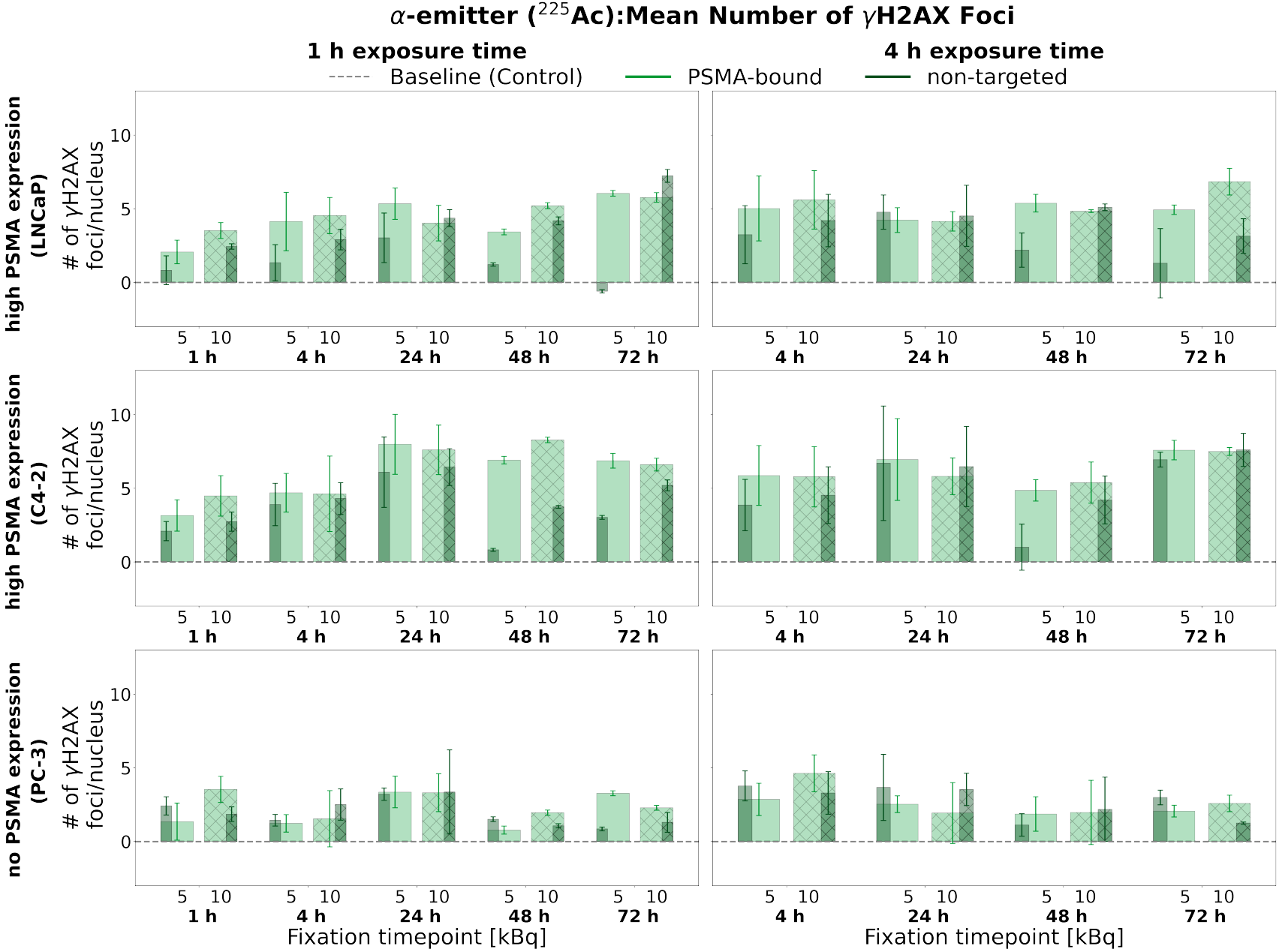

Figure 5.12: **DNA damage evolution over time by α-emitters - number of γH2AX foci:** the number of γH2AX foci detected at later fixation time points, normalized to control levels by subtracting the control value from the data, exhibits distinct trends. A consistently high level of γH2AX foci is maintained for cells treated with α-emitters. Standard deviations are displayed as error bars on top of each bar.

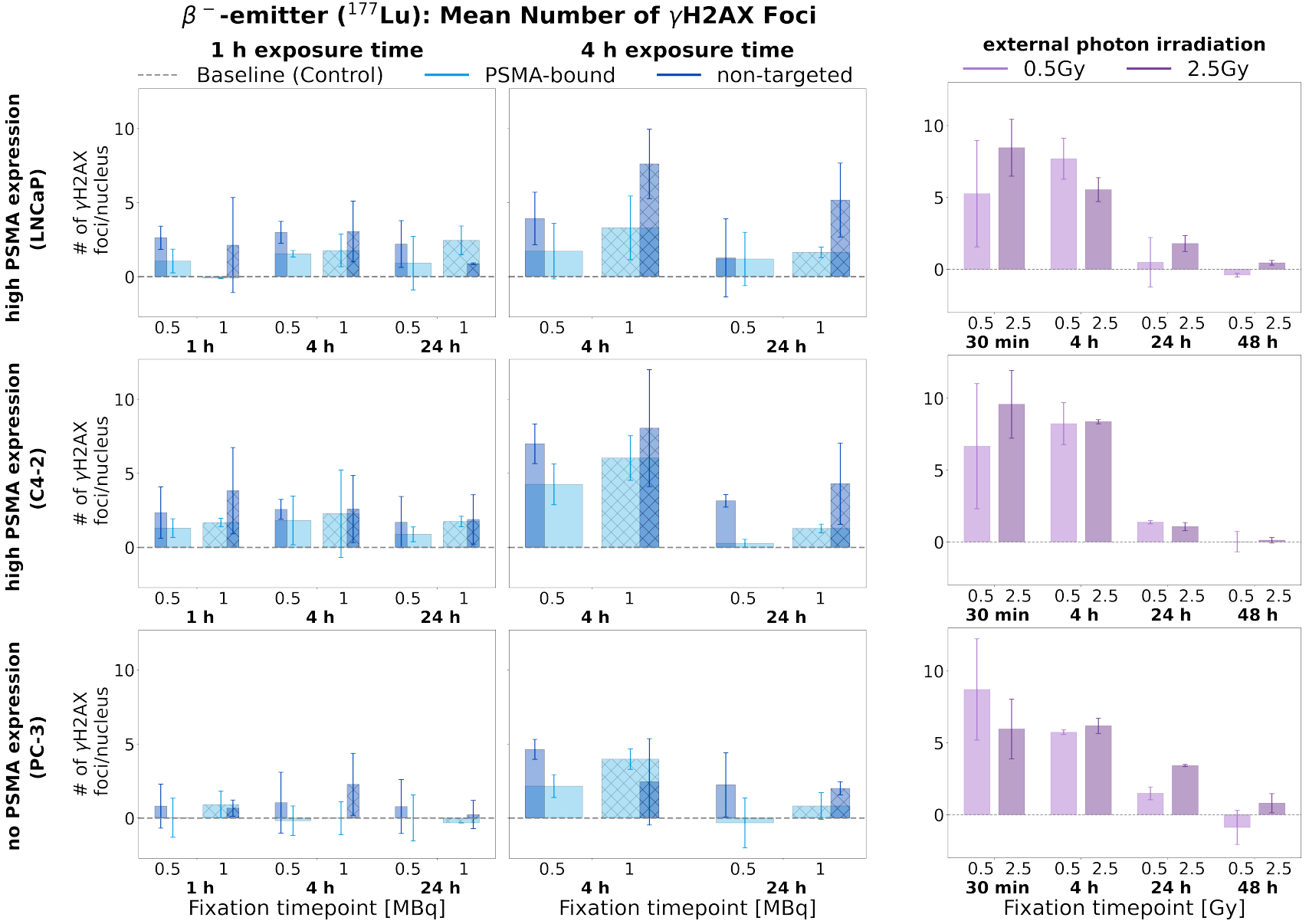

Figure 5.13: **DNA damage evolution over time by β^--emitters and external irradiation - number of γH2AX foci:** the number of γH2AX foci detected at later fixation time points, normalized to control levels by subtracting the control value from the data, exhibits distinct trends. A decline in the number of γH2AX foci is observed in samples treated with β^--emitters and external photon irradiation. Standard deviations are displayed as error bars on top of each bar.

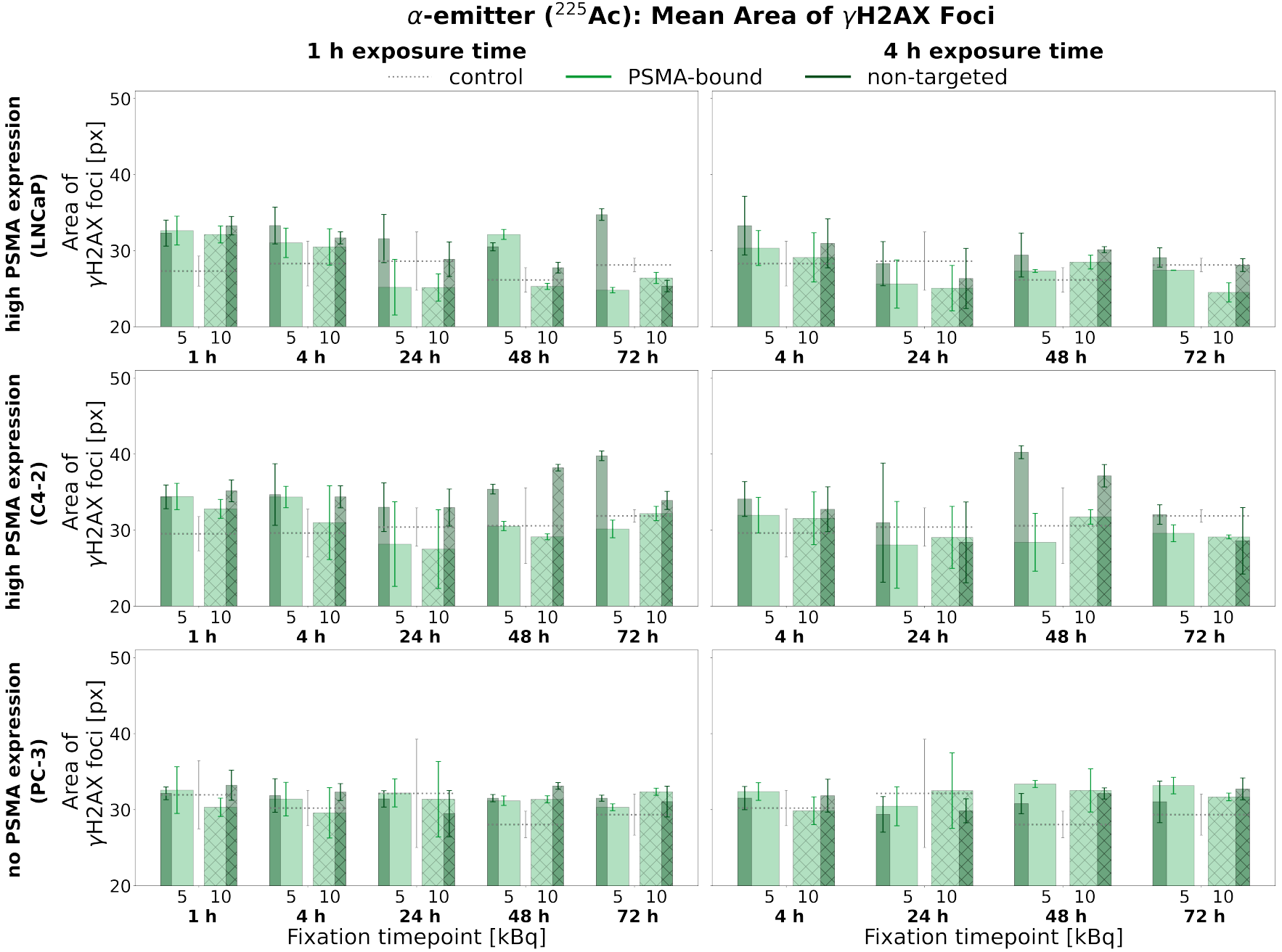

Figure 5.14: **DNA damage evolution over time by α-emitters - area of γH2AX foci:** the area of γH2AX foci detected in all samples is presented, with the foci area of control samples at each time point indicated by a gray dotted line. Standard deviations are displayed as error bars on top of each bar. The area of α-emitter induced foci is larger than the area of foci induced by β^--emitter or external photon irradiation.

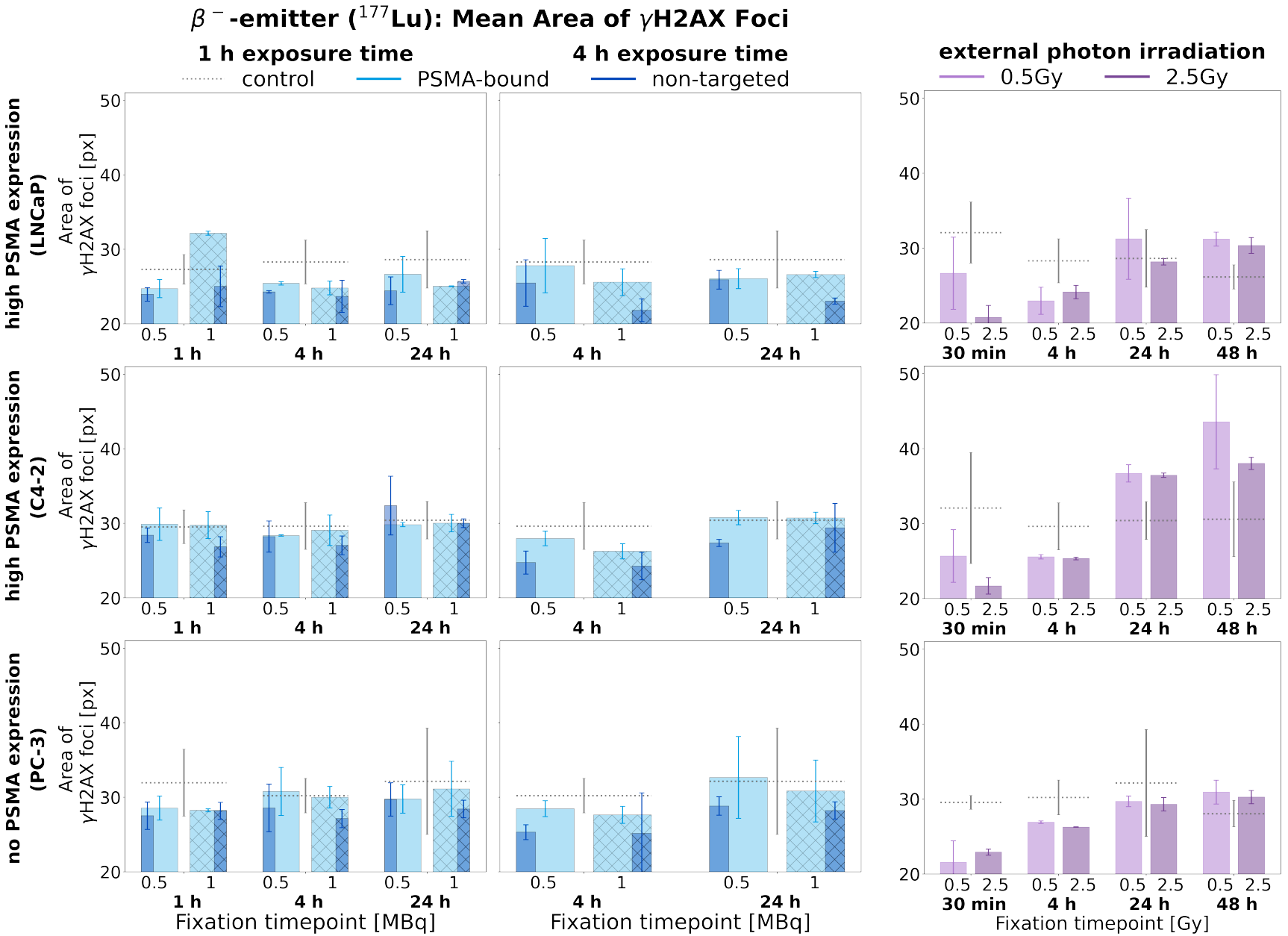

Figure 5.15: **DNA damage evolution over time by β^--emitters and external irradiation - area of γH2AX foci:** the area of γH2AX foci detected in all samples is presented, with the foci area of control samples at each time point indicated by a gray dotted line. Standard deviations are displayed as error bars on top of each bar. The area of TRT induced foci stabilizes at later time points while it increases to a size larger than control in the external irradiated samples.

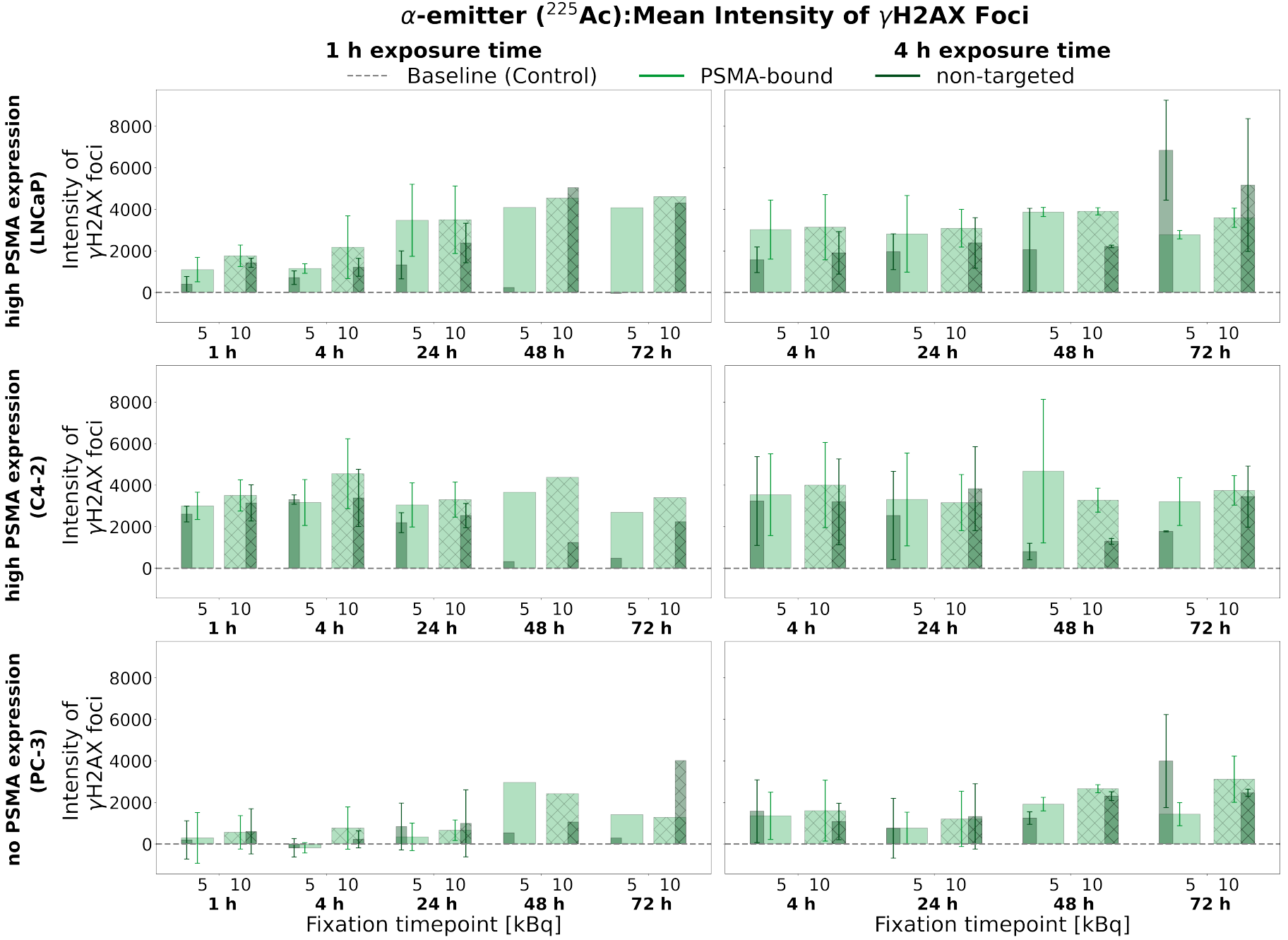

Figure 5.16: **DNA damage evolution over time by α-emitters - intensity of γH2AX foci:** the intensity of γH2AX foci is normalized to control levels by subtracting the intensity of control from the data. Standard deviations are displayed as error bars on top of each bar. For the α-emitter, the γH2AX foci intensity a high level of intensity is maintained across all time points.

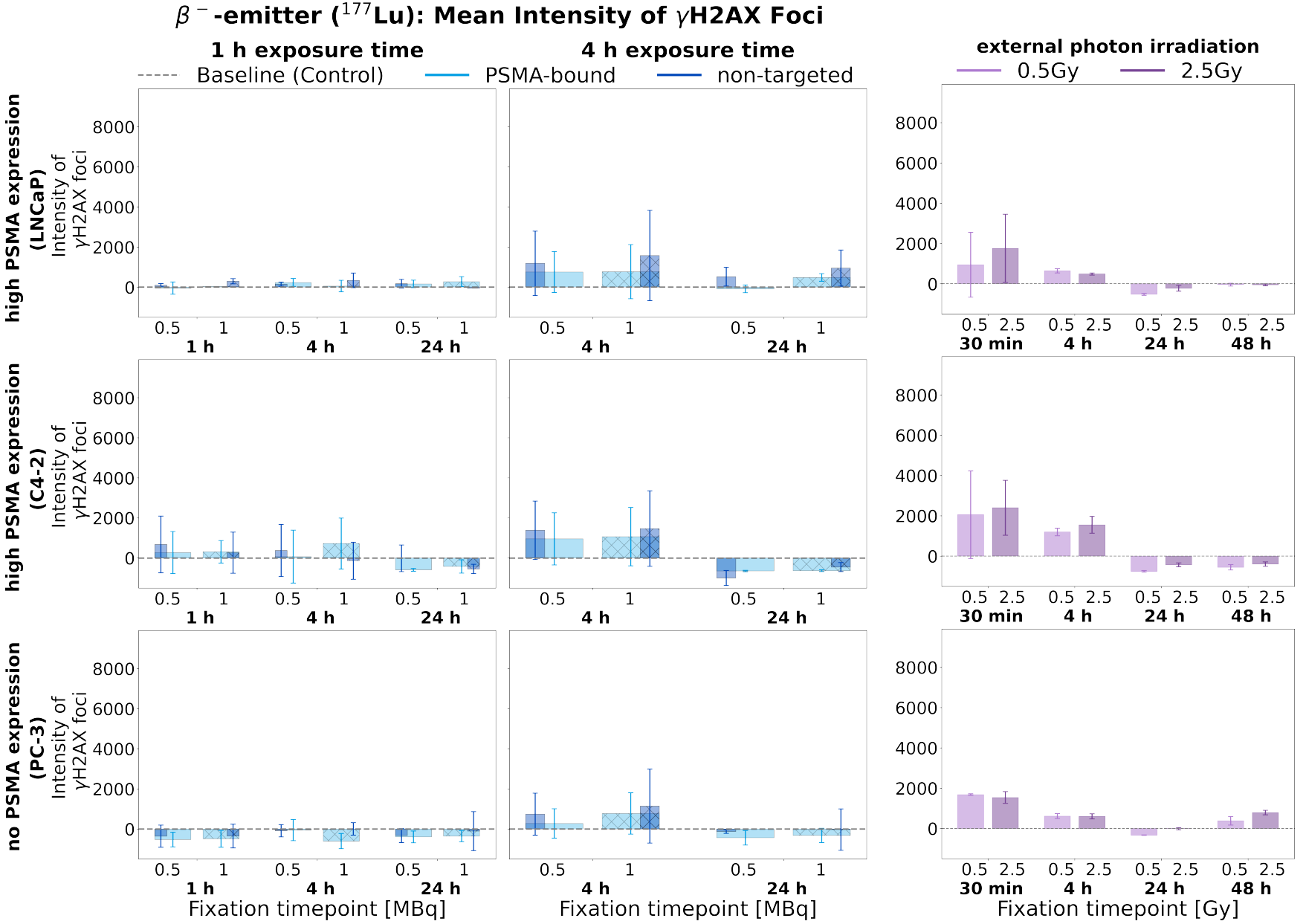

Figure 5.17: **DNA damage evolution over time by β^--emitters and external irradiation - intensity of γH2AX foci:** the intensity of γH2AX foci is normalized to control levels by subtracting the intensity of control from the data. Standard deviations are displayed as error bars on top of each bar. Intensity of γH2AX foci declines over time in samples treated with β^--emitter and external irradiation.

5.4 Combination Therapy with DNA Repair Inhibitor

In this section the efficacy of combining a DNA repair inhibitor with various radiation types is evaluated in the three prostate cancer cell lines (LNCaP, C4-2 and PC-3). The DNA-PKi Nedisertib® was selected as the DNA repair inhibitor due to its demonstrated potential in previous studies. The experimental setup was based on earlier work conducted at DKFZ by Emily Hellwich [120], which showed that Nedisertib® exhibits radiosensitization properties when combined with external photon irradiation (2 Gy to 4 Gy) in lung and pancreas cancer cell lines.
Following an initial trial using a similar setup to the studies of Hellwich Emily with external photon irradiation in prostate cancer cell lines (see Subsection 5.4.1), the combination therapy was extensively investigated with TRT (refer to Subsection 5.4.2). The radiopharmaceuticals [^{177}Lu]Lu-PSMA-617 and [^{225}Ac]Ac-PSMA-716 were employed at either a single activity concentration in combination with a concentration curve of Nedisertib®, or at two concentrations of Nedisertib® (0.1 and 1 µM) along with a concentration curve of the radiopharmaceuticals. The primary objective was to demonstrate the potential of combination therapy for TRT and identify an effective treatment regimen involving both compounds.

5.4.1 DNA Repair Inhibitor combined with External Photon Radiation

The efficacy of the combined treatment with the DNA-PKi Nedisertib® was investigated in prostate cancer cell lines using external radiation as the first step. These findings are presented in Figure 5.18. The results showed that the combination of 1.5 Gy of external photon irradiation and DNA-PKi Nedisertib® led to a significant improvement in outcome compared to treatment with Nedisertib® alone in radiosensitive cell lines, LNCaP (**p-value) and C4-2 (*p-value). In contrast, the combination therapy did not offer a significant advantage over Nedisertib® monotherapy in the PC-3 cell line, which exhibited less radiosensitive response in the previous studies. Notably, high concentrations of Nedisertib® (above 5 µM) induced substantial cytotoxicity in monotherapy, leading to drastic decreases in cell proliferation. Conversely, lower concentrations (1 µM and below) had a limited impact on reducing cell proliferation.

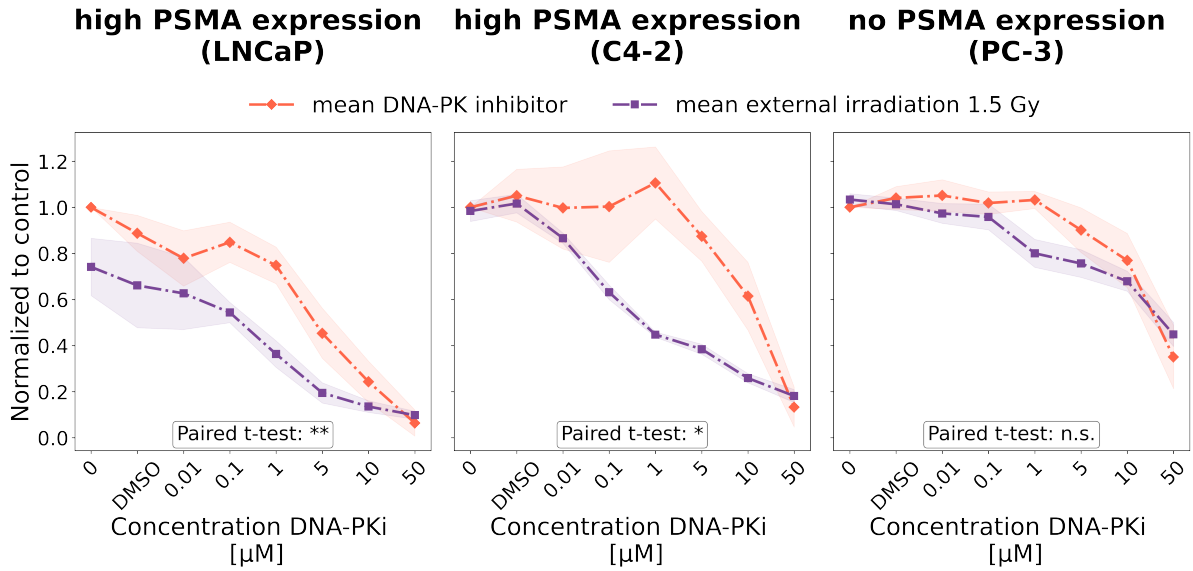

Figure 5.18: **Combination therapy of DNA-PKi with external photon irradiation:** mean values of repetitions are plotted as a dashed line, accompanied by a light transparent band representing the standard deviation. Significant intervals are denoted by: * = p < 0.05, ** = p < 0.01, *** = p < 0.001. Non-significant results (p > 0.05) are indicated as "n.s." (paired Student's t-test).

5.4.2 DNA Repair Inhibitor Combined with Targeted Radionuclide Therapy

In the next step, the combination therapy with TRT was evaluated. All three cells lines were pretreated with Nedisertib® in the previously tested concentration range for 24 h, followed by a 4 h exposure to either [^{177}Lu]Lu-PSMA-617 at 1.25 MBq/mL or [^{225}Ac]Ac-PSMA-716 at 2.5 kBq/mL. These concentrations were selected based on the ranges tested in monotherapy experiments of TRT (refer to Figure 5.5). Notably, all combination treatments with TRT demonstrated a significantly enhanced effect compared to monotherapy with the DNA-PKi Nedisertib® alone (p-values < 0.05). The α-emitter exhibited the most pronounced enhancement in reducing cell proliferation across all three cell lines, with highly significant differences observed (***p-values). In contrast, the β^--emitter showed a less pronounced effect, although still statistically significant. Interestingly, whereas the combination with external photon irradiation did not have a significant impact on cell proliferation in the PC-3 cell line, the combination with the β^--emitter yielded a statistically significant result (p-value *).

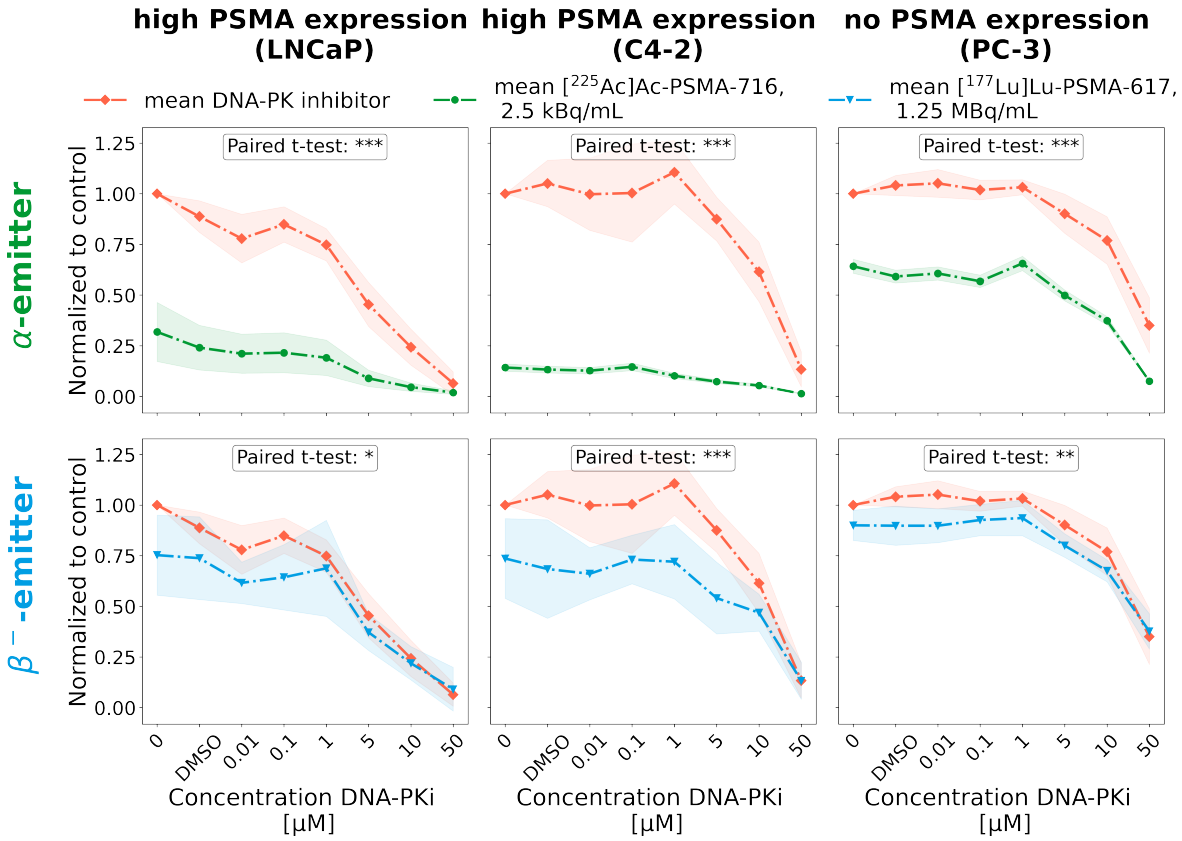

Figure 5.19: **Combination therapy of DNA-PKi with TRT:** mean values of repetitions are plotted as a dashed line, accompanied by a light transparent band representing the standard deviation. Significant intervals are denoted by: * = $p < 0.05$, ** = $p < 0.01$, *** = $p < 0.001$. Non-significant results ($p > 0.05$) are indicated as "n.s." (paired Student's t-test).

Furthermore, a comparison of the combination treatments with TRT to those with external irradiation (Figure 5.20) reveals distinct characteristics among the three radiation types (α, β^-, and external photon irradiation). In alignment with the observations in the DNA damage assay, where $\beta^-$and external photon irradiation exhibit similar features and induce comparable levels of DNA damage, similarities between these two radiation types are seen as well in the combined setting. In the overlay of the three combination treatments with the same concentration range of the DNA-PKi, the curves for [^{177}Lu]Lu-PSMA-617 (1.25 MBq/mL) and external irradiation (1.5 Gy) followed a similar trend across all three cell lines. The combination treatment with the α-emitter [^{225}Ac]Ac-PSMA-716 (2.5 kBq/mL) is the most effective in inhibiting cell proliferation in all three cell lines.

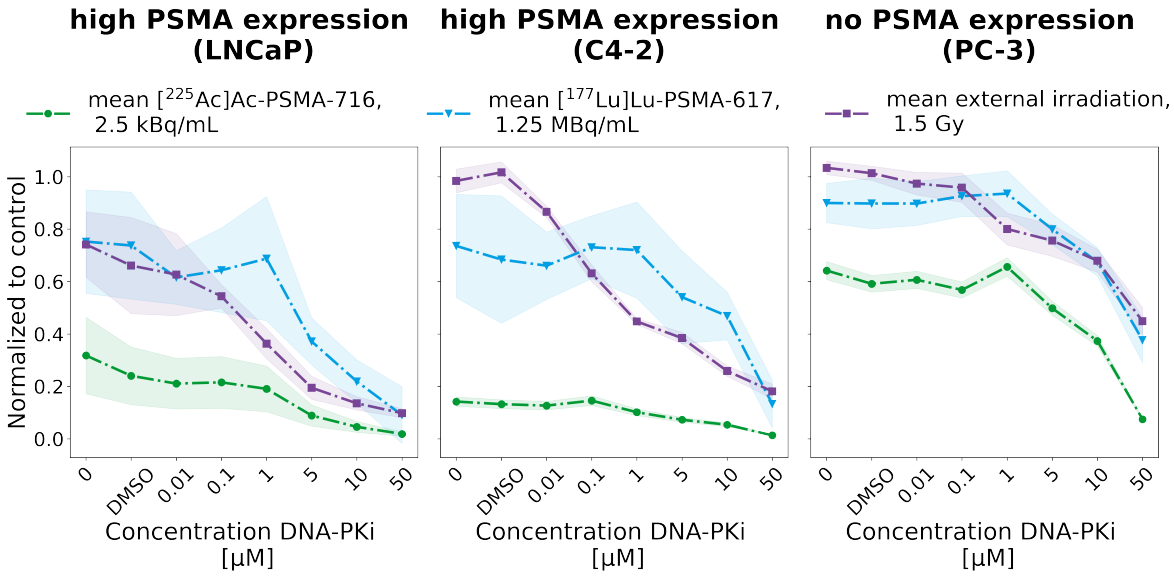

Figure 5.20: **Combination therapy of DNA-PKi with TRT comparison to external photon irradiation:** mean values of repetitions are plotted as a dashed line, accompanied by a light transparent band representing the standard deviation. Significant intervals are denoted by: * = p < 0.05, ** = p < 0.01, *** = p < 0.001. Non-significant results (p > 0.05) are indicated as "n.s." (paired Student's t-test).

The benefits of a combination therapy are most prominently demonstrated in Figure 5.21. To assess the potential of the combination therapy to enable a reduction in activity for Targeted Radionuclide Therapy (TRT), two low concentrations of the DNA-PKi (0.1 and 1 µM) were chosen. In the monotherapy, these two concentrations did not show a reduction in cell proliferation for C4-2 and PC3 (normalized values ≥ 1), and only a slight reduction for the most sensitive LNCaP (0.85 / 0.75).or TRT, the same concentration range used in monotherapy was employed (refer to Table 4.3).

When comparing the monotherapy of TRT to the combination therapy with low concentrations of the inhibitor, a significant drop in cell proliferation can be observed even for the lowest activity concentration of TRT (α: 0.156 kBq/mL and β^-: 78.1 kBq/mL). Notably, there is only a slight significant difference between the two inhibitor concentrations (0.1 µM and 1 µM), suggesting that DNA repair is already sufficiently disrupted by a low amount of DNA-PKi. For [^{177}Lu]Lu-PSMA-617, the combination treatment enhanced the effect of the lowest activity concentration significantly in PSMA-positive cell lines (C4-2 and LNCaP) compared to monotherapy with [^{177}Lu]Lu-PSMA-617.

Most interestingly, the combined treatment of DNA-PKi and [^{225}Ac]Ac-PSMA-716 affected even the cell proliferation of the PSMA-negative and most radioresistant

cell line PC3, significantly. Compared to the monotherapy with [^{225}Ac]Ac-PSMA-716, where only the highest concentration of 10 kBq/mL could reduce the cell proliferation to 0.51 compared to untreated control, the combination therapy with the lowest activity concentration 0.156 kBq/mL reduced the cell proliferation already similarly (0.1 µM: 0.49, 1 µM: 0.47).

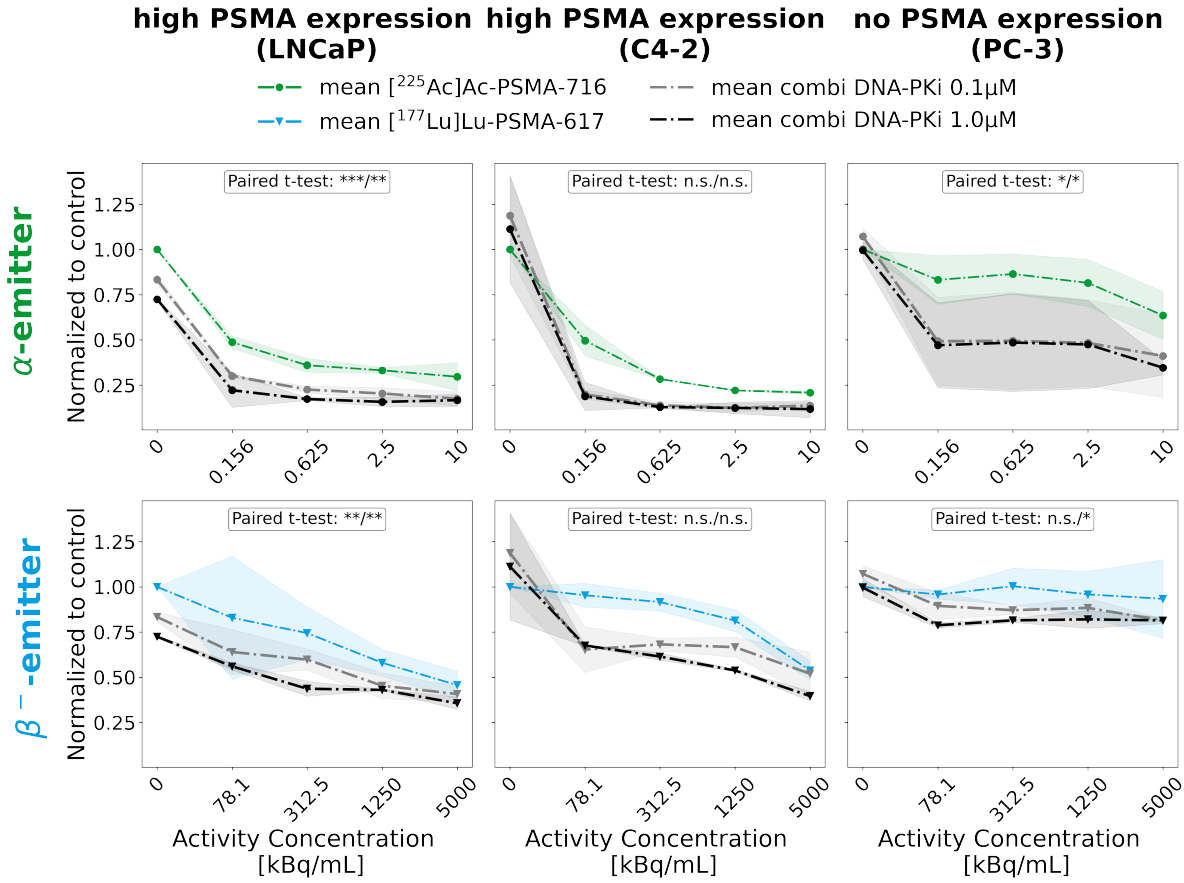

Figure 5.21: **Combination therapy of DNA-PKi (0.1 or 1 µM) with TRT:** mean values of repetitions are plotted as a dashed line, accompanied by a light transparent band representing the standard deviation. Significant intervals are denoted by: * = p < 0.05, ** = p < 0.01, *** = p < 0.001. Non-significant results (p > 0.05) are indicated as "n.s." (paired Student's t-test).

To further optimize the treatment protocol, different treatment schedules were tested qualitatively. For both radiopharmaceuticals, [^{177}Lu]Lu-PSMA-617 and [^{225}Ac]Ac-PSMA-716, a 24 h break was introduced between the administration of the DNA-PKi on Day 1 and the administration of TRT on Day 3. This modification was based on the observation that cellular uptake assays indicated slightly reduced uptake and internalization of the radionuclide immediately after pretreatment with the DNA-PKi, compared to untreated cells. It was hypothesized that the break would allow the cells to recover their receptor expression, thereby enhancing the effect of TRT due to improved internalization. However, when testing this treatment schedule, no improvement in the outcome of combined treatment with a break was observed compared to the usual treatment schedule for both radionuclides.

For [^{225}Ac]Ac-PSMA-716, two additional treatment schedules were also investigated. In one approach, parallel treatment with [^{225}Ac]Ac-PSMA-716 diluted in medium supplemented with DNA-PKi was applied for 4 h, followed by replacement of the medium with non-active, DNA-PKi-supplemented medium for an additional 20 h (Day 1). This procedure is resembling the combination with external photon irradiation, where the cells were pretreated for 1 h prior to irradiation followed by continued incubation with Nedisertib® up to 24 h in total. Therefore, the DNA-PKi was present during radiation exposure.

In another approach, an inverse treatment schedule was performed, where cells were treated with [^{225}Ac]Ac-PSMA-716 for 4 h, followed by a 24 h treatment with DNA-PKi. Neither of these alternative treatment schedules showed significant differences compared to the usual treatment schedule, which performed 24 h pretreatment with Nedisertib® directly followed by TRT treatment for 4 h.

6 Discussion

To optimize TRT, this thesis aims to bridge existing knowledge gaps in radiobiological effects of different radionuclides, dosimetry, and effective combination therapy strategies. This chapter provides an overview and discussion of the results from Chapter 5, placing them within the context of recent literature and biophysical mechanisms.

6.1 Physical Parameters Determining the Biological Effect

How do physical parameters such as activity concentration, emitter type, and exposure time impact the biological effectiveness of TRT?

- The activity ratio required for similar biological effectiveness is 1:100 for DNA damage and 1:500 for cell proliferation assays when comparing the used α- to β^--emitters, ^{225}Ac and ^{177}Lu;
- Long-range β^--emitters (1.5 mm to 1.7 mm) do not benefit from internalization induced by targeting, whereas internalization plays a crucial role for short-range α-emitters (47 µm to 85 µm);
- Increasing exposure time and activity provides benefits for treatment outcome for β^--emitters more than α-emitters.

To address the research question regarding how physical parameters - such as activity concentration, emitter type, and exposure time - impact the biological effectiveness of TRT, a comprehensive series of experiments was conducted. These experiments aimed to evaluate the interplay between these physical factors and their influence on biological outcomes. Since each radionuclide possesses unique physical characteristics, understanding these relationships is crucial for selecting the most appropriate radionuclide for specific therapeutic applications.

Overall, in evaluating various radionuclides, it became evident that the type of emitter (α- or β^--emitter) is the most critical factor influencing biological effectiveness. Experimental results demonstrated that the β^--emitter ^{177}Lu required 100 times higher activity in a DNA damage assay and up to 500 times higher in a cell proliferation assay to achieve similar biological effects as those induced by α-emitters. A previous study comparing [^{225}Ac]Ac- and [^{177}Lu]Lu-DOTATOC found that a 700-fold increase in activity was necessary to achieve similar biological effectiveness when assessing γH2AX foci formation [121]. The slightly higher ratio observed in this comparison may be attributed to the difference in radionuclide incubation time, which was notably shorter in experiments of this work (1 or 4 h) compared to the cited study (48 h). Depending on the emitter type, the relevance of other physical parameters varies.

For **short-range α-emitters**, cellular internalization through targeting was identified to be the most crucial parameter (refer to Table 5.2). In both PSMA-positive cell lines, PSMA-bound activity caused significantly (p-value > 0.05, Student's t-test) more DNA damage than non-targeted activity. To reach a similar level of DNA damage, non-targeted activity needed to be increased tenfold. Specifically, the number of γH2AX foci induced was comparable for 1 kBq of [^{225}Ac]Ac-PSMA-716 and 10 kBq of $^{225}Ac(NO_3)_3$. However, in the PSMA-negative cell line, PC-3, where the target is absent on the cell surface and no internalization occurs, both PSMA-targeted and non-targeted activities exhibited similar efficacy. No comparable study *in vitro* has been conducted, however, an *in silico* study simulating absorbed dose to the nucleus per decay for ^{225}Ac and ^{223}Ra, showed that absorbed increases when radionuclides are localized in the cytoplasm compared to membrane-bound, confirming that internalization is a critical parameter for α-emitters [122].
Further evaluation demonstrated that in targeted conditions where activity is internalized, increasing the activity or exposure time has minimal effect on the biological outcome. The reason for this limited effect is that even the lowest activity of [^{225}Ac]Ac-PSMA-716 induced significant DNA damage, which was only slightly increased by higher activities or longer exposure times. For 1 kBq, the ratio of PSMA-bound to non-targeted activity is 1.6-1.8. Increasing the activity led to a maximum ratio of 1.2 for targeted activity but 1.6-1.8 for non-targeted activity. Similarly, extending the exposure time resulted in a ratio of 1.3-1.5 for both modalities. For non-targeted activity localized at the cell membrane, increasing the activity level was the most critical parameter for enhancing DNA damage.
Furthermore, the α-emitter ^{225}Ac demonstrated potential to achieve overall activity reduction in an internalized setting, as even low amounts of targeted activity

induced similar effects as higher amounts. However, it is noteworthy that in a setting with heterogeneous expression, a combined approach utilizing both emitter types could be crucial, as the α-emitter is less effective when the target is not expressed (PC-3 cell line). While the α-emitter may struggle in areas with low target expression, the β^--emitter can still induce DNA damage through proximity to neighboring target-expressing cells. In conclusion, the dual-emitter treatment approach offers great promise for overcoming radioresistance and heterogeneity, thereby enabling optimized TRT that minimizes potential side effects. This approach is already tested in clinical settings, and has been shown to reduce the side effect xerostomia by reducing activity of ^{225}Ac [13]. Furthermore, retroperspective analysis of patients receiving the tandem therapy compared to monotherapy with [^{225}Ac]Ac-PSMA-716 concluded that the tandem therapy was better tolerated and had a median overall survival of 15 months compared to 9 months in monotherapy [123].
Additionally, when assessing the three different α-emitters (^{225}Ac, ^{227}Th, and ^{223}Ra), it was observed that variations in their decay chains, due to differing half-lifes, impacted the biological outcome the most. Notably, the radionuclides ^{225}Ac and ^{223}Ra, which exhibit short half-life times to their next α-decay (^{225}Ac$\rightarrow$ ^{221}Fr, $T_{1/2}$ = 4.8 min; ^{223}Ra$\rightarrow$^{219}Rn, $T_{1/2}$ = 4 s) induce slightly more DNA damage than ^{227}Th (^{227}Th$\rightarrow$ ^{223}Ra, $T_{1/2}$ = 11.4 d) [52] (refer to Table 5.1). These experimental findings are supported by *in silico* modeling of single cell dosimetry and DNA damage caused by different α-emitters (^{225}Ac, ^{223}Ra, ^{211}At and ^{212}Pb) [122]. Specifically, ^{225}Ac and ^{223}Ra, due to their longer decay chains and higher α-particle yields, delivered higher absorbed doses to the cell nucleus per decay event compared to ^{212}Pb and ^{211}At (for details refer to NuDat 3.0 database [52]).
To the best knowledge available, the effects of non-targeted activity, varying activity levels, and exposure times for α-emitters have not been systematically studied elsewhere. Therefore, direct comparison with existing literature is hindered by the limited availability of similar studies.

When considering the **long-range β^--emitter**, the scenario shifts, and the effect of internalized activity compared to non-targeted activity becomes negligible. Across all three cell lines, the ratio of PSMA-bound to non-targeted activity resulted in the value 0.9, indicating that non-targeted activity, characterized by high membrane binding, was found to be slightly more effective than PSMA-specific targeting with lower membrane binding. Concluding that for β^--emitters, a strong and specific binding interaction with the cell membrane becomes more important, even if internalization is lower in comparison. These characteristics were also

highlighted in the literature, where studies on agonists and antagonists provided further insights into optimal targeting strategies for β^--emitters [124]. Notably, no significant differences were found between the membrane-localized antagonist ([^{177}Lu]Lu-DOTA-LM3) and the cytoplasm-localized agonist ([^{177}Lu]Lu-DOTATOC). Consequently, further experiments conducted in this work demonstrated that high activity levels and prolonged exposure times improved the therapeutic efficacy of the β^-, whereas they had only a minor impact on the α-emitter. For the β^--emitter, a tenfold increase in activity resulted in a maximum increase in DNA damage of 1.4-1.9, while prolonged exposure time accounted for a factor of 1.4-2.0. Overall, increasing the exposure time had a more pronounced effect than increasing activity, suggesting that optimizing the biological half-life of radiopharmaceuticals employing β^--emitters may be a key factor in clinical settings.

Comparing **all radiation types**, it was remarkable that distinct characteristics of γH2AX foci were observed based on the prevalent mechanism of DNA damage induction. Specifically, β^--emitting radionuclides and external photon irradiation, which share common properties due to their indirect DNA damage induction mechanisms, exhibited different behaviors compared to α-emitters, which predominantly induce DNA damage directly. These observations are consistent with further findings in the literature comparing the three radiation types. A study comparing an α-emitter (^{241}Am), a β^--emitter (^{177}Lu), and γ-rays from a ^{137}Cs source, found no significant difference in surviving fractions between cells treated with β^--particle and γ-ray irradiation in the LNCaP and PC-3 cell lines [125]. In contrast, α-particle-treated samples showed a higher level of cell killing.
Furthermore, this work discovered as well differences in DNA damage response between TRT and external photon irradiation. Both radionuclides exhibited an increase in DNA damage with 1 h exposure time comparing 1 h to the 4 h (1 h + 3 h recovery time). DNA damage from external photon treatment decreased when comparing post-treatment times of 30 min to 4 h (refer to Figure 5.6). However, delayed repair was observed for external photon irradiation in the low-dose regime of 0.5 Gy, where DNA damage remained elevated at both early time points, 30 min and 4 h, before decreasing at 24 h (refer to Figure 5.11). The sustained increase in DNA damage during the recovery period of 3 h can be attributed to the unique properties of TRT, which can lead to delayed DNA repair signaling due to continuous DNA damage induction over a prolonged period. Additionally, residual internalized or membrane-bound activity can cause further DNA damage.

In summary, the findings in this work and the comparison with existing literature, underscore the importance of studying the impact of physical parameters on the biological outcome of TRT and understanding the differences between α- and β^--emitters and within various α-emitters. The study provided valuable insights into the impact of targeting on short- and long-range α- and β^--emitters, offering important considerations for designing radiopharmaceuticals tailored to these emitter types. In the clinical setting, targeting is essential for specifically reaching tumor cells. Based on the above discussed findings, the distinct **radiopharmaceutical targeting properties** should depend on the type of emitter used.
When developing a radiopharmaceutical with an **α-emitter, high internalization** rates are desirable to achieve maximum biological effect. Especially, when considering nanogenerators like ^{225}Ac, which undergo multiple decays, internalization is furthermore crucial to avoid free daughter nuclides in the bloodstream, which could lead to unwanted side effects [55]. While designing a radiopharmaceutical for a **β^--emitter, high membrane binding** should be favored over internalization. This is particularly relevant if the β^--emitter is additionally an Auger electron emitter, such as the radioisotope ^{161}Tb. ^{161}Tb is currently being evaluated in comparison to ^{177}Lu for a clinical alternative. Experiments suggest that, in addition to the hypothesis of bringing an Auger emitter close to the nucleus, the cellular membrane could be a more suitable and easier reachable target [124]. A 102-times increased efficacy to reduce cell viability *in vitro* was demonstrated by membrane-binding [^{161}Tb]Tb-DOTA-LM3 compared to [^{177}Lu]Lu-DOTA-LM3 [124].

The study design has both strengths and limitations. While the impact of physical parameters was investigated in two biological assays, further research is needed to understand the underlying mechanisms driving the observed behaviors. Additional to the study of cell proliferation and DNA damage, further biological parameters such as cell viability or apoptosis, could provide valuable insights into therapeutic efficacy. In addition, treatment outcome could be studied in clonogenic survival assay, which is the gold standard in radiation biology. Moreover, the study only evaluated specific, discrete measurement points for activity and exposure time, and the DNA damage assay is only sensitive within a particular time frame and treatment regime, as was demonstrated by the saturation at high activity levels (100 kBq α-emitter).
Furthermore, this investigation focused primarily on two radionuclides, ^{225}Ac (representative of α-emitters) and ^{177}Lu (for β^--emitters). While experiments with different α-emitters in this study and comparisons with literature for β^--emitter ^{177}Lu and ^{161} revealed that biological effectiveness differs among radionuclides, even

within similar emitter types, it is challenging to cover this variety in one experimental setup. This challenge arises due to limited availability of certain radionuclides and infrastructure constraints such as handling permissions. This is generally a huge challenge for exploring the radiobiology of TRT, as most working groups typically specialize in specific radionuclides, making it rare that even multiple radionuclides are investigated in one identical setting. Similarly, the study required selecting a specific biological model, chosen as PSMA-positive prostate cancer.
Although the findings are attained within this specific model and radionuclides, the qualitative insights - such as the impact of internalization, activity levels, and exposure time - can be extrapolated to other models. However, quantitative results may vary based on factors like cell line characteristics, radiosensitivity, radiopharmaceutical targeting, and radionuclide properties. Specifically, certain key principles underlined in this work remain consistent: for α-emitters, internalization is critical, while higher activity levels are generally required for β^--emitters in comparison.

6.2 Development of a Geant4-DNA Simulation for Single-Cell Dosimetry

How can a single-cell simulation be designed to estimate absorbed dose as a function of subcellular radionuclide localization and to model DNA damage induction?

- The distribution of radionuclides differs between targeted and non-targeted activities, with non-targeted activity binding unspecifically to the cell membrane;
- A simplified single-cell model with random particle source placement within the cell (either at the membrane or in the cytoplasm) was realized;
- Extending the simulation to include radionuclide as sources and measuring deposited energy within the nucleus volume is essential for accurate absorbed dose determination.

One of the most significant research gaps in TRT is dosimetry, which is hindered by the complex interplay between physical and biological mechanisms operating across multiple biological scales, from sub-cellular to microscopic single-cell levels up to macroscopic multi-cell levels and whole-body systems in patient dosimetry. Additionally, as demonstrated above, the different physical characteristics of radionuclides require different activity ranges to achieve comparable biological effects. A major challenge in this field is the inconsistent reporting of dosimetry in *in vitro* studies. Specifically, the quantification of the total activity delivered over the incubation period is often unclear, as some studies report only the administered activity or activity concentration, sometimes without specifying the applied volume [8, 126]. This inconsistency makes it challenging, if not impossible, to compare results across different studies and determine radiobiological effects. However, standardizing a physical parameter such as total absorbed dose for each assay would significantly enhance comparability and enable quantitative comparisons between studies. Therefore, this work aimed to contribute a crucial piece to the puzzle of achieving consistent dosimetry in *in vitro* studies by developing a simplified single-cell simulation framework. The approach included the combination of experimentally determined radionuclide distribution as initial input for the model.

Distinct behavior between non-targeted radioactivity and PSMA-bound activity has been revealed through **cellular uptake** experiments. For both radionuclides, ^{177}Lu and ^{225}Ac, high unspecific membrane binding for the non-targeted radionuclides has been observed (20-35% of total applied activity). Remarkably, a magnitude lower, receptor-specific membrane binding (4%) was determined for the PSMA-bound activity. A study that performed cellular binding assays with [^{111}In]$InCl_3$, [^{68}Ga]$GaCl_3$ and $^{177}LuCl_3$ reported similar results [127]. Raitanen et al. observed high membrane binding of $^{177}LuCl_3$ (25%) compared to targeted [^{177}Lu]Lu-PSMA-I&T (3%). Notably, this phenomenon was not observed for [^{111}In]$InCl_3$ and [^{68}Ga]$GaCl_3$. No other *in vitro* study has been performed on the cellular binding of non-complexed ^{225}Ac, making the high unspecific membrane binding of $^{225}Ac(NO_3)_3$ similar to $^{177}LuCl_3$ reported for the first time in this work. Typically, research focuses solely on the cellular binding of targeted activity, making these findings unique and highlighting the need for further investigation into this phenomenon. These results underscore the importance of radiochemical purity, as impurities of non-targeted activity after radiolabelling could lead to false estimations of the uptake behavior of a radiopharmaceutical.

The calculated numbers of estimated radionuclide distribution (detailed in Table 5.7) reveal that the impact of unspecific binding on total absorbed dose should not be neglected, particularly for long-range β^--emitters. As the similar DNA damage induction between non-targeted and PSMA-bound activity has shown, β^--particles can cause DNA damage even when not internalized, and higher membrane binding could contribute to equal DNA damage compared to the targeted compound. To determine the influence of the radionuclide distribution and unspecific membrane binding on the absorbed dose, a simulation is essential.
As previous single-cell studies using α-emitters have demonstrated, simulations can offer valuable insights into the relationship between radionuclide localization and absorbed dose [122]. To control radionuclide localization in experimental assays is very challenging, thus simulation-based studies are crucial to complement experimental findings and hypotheses. Overall, the integration of simulation results with experimental data offers a more comprehensive understanding of how radionuclide properties impact biological effects and holds potential for identifying specific radionuclide characteristics relevant to treatment efficacy, particularly in terms of localization.

Regarding the **basic single-cell model** developed in this work, an important next step is adjusting its geometry to match the measurements of the cell lines used in experiments. This modification is crucial to ensure that the results accurately represent the behavior of the specific cell lines being studied. A study investigating the S-values of different radionuclides confirmed the importance of this modification to gain accurate results [128]. They determined significant changes in S-values with increasing cell and nucleus size.
Another adaptation required is changing to the full simulation of the radionuclide decay chain instead of using mean α-energies as a source. The above-cited study, which evaluated the impact of different α-radionuclides, also performed a simulation using isotropic discrete α-energies as sources rather than simulating the full decay chain [122]. In contrast to the simulation employing the full decay chain, which showed significant differences in the number of DNA damages induced by different radionuclides, using only the α-energies showed no significant difference anymore between the different radionuclides. This highlights the critical importance of accurately modeling the decay chain to capture the full biological impact, particularly when comparing different radionuclides.

Following the implementation of all modifications to measure absorbed dose, the next step would be to extend the single-cell simulation model to incorporate the **simulation of induced DNA damage and repair**, analogous to the cited publication above. To simulate induced DNA damage, the geometry and source modifications applied to the single-cell model should be integrated into the GEANT4 DNA example *moleculardna*. A detailed description of the model and its applications can be found in the relevant literature [105, 110, 111, 129]. This model simulates early direct and indirect DNA damage, allowing for discrimination between single-strand breaks, double-strand breaks, and complex double-strand breaks. The simulation of this model demands substantial computing power due to the complex nature of DNA geometries and interactions involved.
The ultimate objective is to validate the model by comparing its predictions with experimentally determined DNA damage. Since experimental determination of DNA damage is resource-intensive, an established and validated simulation can be used to explore additional parameters (e.g., varying activities) *in silico*, identifying promising scenarios for subsequent experimental verification. This approach optimizes resource use and streamlines research. For instance, a study demonstrated the potential of this method in conducting *in silico* clonogenic cell survival assays [128].

Furthermore, while DNA damage occurs at the molecular level due to radiation, accurate simulations must account for cross-irradiation effects that affect neighboring cells on a larger spatial scale and contribute to overall biological effectivenes as emphasized in this thesis. Long-range β^--emitters are particularly known for crossfire effects, which enhance their ability to treat heterogeneous and larger cell clusters by increasing the absorbed dose in cell clusters. This underscores the necessity of moving beyond single-cell simulations and incorporating **multicell monolayer** models to more accurately represent experimental conditions.
With this approach, complex interactions of radionuclides on cell clusters can be studied. For instance, Tamborino et al. employed a simulation framework featuring a planar cellular cluster to study DNA damage caused by [^{177}Lu]Lu-DOTA-TATE, taking into account different distributions of the radionuclide (internalization in cytoplasm or golgi apparatus) [109]. Another example is the comparison of deposited doses from the β^--emitters ^{177}Lu and ^{161}Tb, which analyzed the impact of cell cluster size, ratio of labeled cells within the cluster, and the subcellular localization of radioactivity on dose delivery [91]. Notably, these simulation studies revealed that ^{161}Tb can achieve similar deposited doses with smaller activities.

Finally, in contrast to simulations involving external radiation sources, the dose distribution in internal radiation therapy is highly heterogeneous, posing significant challenges for modeling. While simulations can estimate deposited energies and DNA strand breaks, predicting cell survival remains impossible with these parameters alone. This limitation arises because additional biological effects, such as the bystander effect, cannot be captured by simulating physical particle-matter interactions. Furthermore, cell survival rates exhibit significant variability depending on the specific cell line, with some cells displaying greater radioresistance than others, particularly in cancer cells. These differences are often linked to modifications in DNA repair pathways, which can be difficult to incorporate into simulations due to their complexity and variability. Consequently, extensive experimental investigation of these differences is essential before they can be used as input for simulations. Therefore, simulation results must be interpreted cautiously and validated against experimental data to ensure their accuracy and reliability.

6.3 DNA Damage Evolution at Late Time Points - Repair and Persistent DNA Damage

What biological differences exist in the induction (e.g., size, structure) and long-term repair of DNA damage caused by α- and β^--emitters?

- α-particles induce larger, more complex DNA damage sites compared to the smaller damage sites caused by β^--particles and external photon irradiation;
- DNA damage persists in cells treated with α-emitters up to 72 hours, while it is repaired (reduced to near-control levels) after 48 hours in cells exposed to β^--emitters and external photon irradiation;
- Differences in DNA damage pattern and biological effect between α-emitters and common findings of external photon irradiation and β^--emitters align with the prevalent mechanism in DNA damage induction (direct vs. indirect).

To optimize monotherapy strategies and develop effective combination therapies, understanding the underlying mechanisms of DNA repair after TRT is critical. Current knowledge on DNA repair primarily stems from studies using external photon

irradiation. However, as previously shown in Section 6.1, the distinct biological response between TRT and external photon irradiation in DNA damage across short time points (comparing DNA damage from 1 h to 4 h after equal exposure time), suggests differing DNA repair response. Specifically, DNA damage increased for TRT during this period, while it decreased for external photon irradiation. This is further supported by studies demonstrating a non-linear correlation in radiosensitivity between ^{177}Lu-based treatments and external photon radiation across multiple cell lines [130, 131]. Additionally, this work demonstrated that the initial extent of DNA damage alone does not fully predict biological outcomes. Despite comparable levels of DNA damage induction across all radiation types (with adjusted activity levels), the long-term proliferation assay revealed that the α-emitter outperformed the β^--emitter even at adjusted activity levels. Therefore, to address this gap and evaluate these discrepancies further, the number and characteristics of γH2AX foci (including size and intensity) were examined at early (up to 4 h) and late time points (up to 72 h), following treatment with three distinct radiation types: α- and β^--emitters, and external photon irradiation.

As a reference point, **external photon irradiation** was used as the gold standard of radiobiology. Notably, a return of DNA damage levels to control values by 48 h after irradiation exposure was observed across all doses [0.5 Gy to 2.5 Gy]. This aligns with current knowledge, as in a study comparing external photon irradiation to carbon ions, a drop of γH2AX foci to the control level at 48 h after exposure to external photon irradiation of 1 Gy is reported [117]. Furthermore, the peak in γH2AX foci number at 30 min after radiation exposure is consistent with previous studies as well that have reported maximum increases in γH2AX foci within 15 min - 1 h after 2 Gy [131].
Although the number of γH2AX foci has decreased to control levels at 48 h, the characteristics of the remaining foci, however, were distinct from those at control levels. In particular, an increase in foci area at late time points was observed, which may be attributed to persistent or challenging-to-repair DNA damage. This can lead to opened chromatin structures that facilitate the repair process and larger damage sites. Consistently, larger areas of γH2AX foci were also reported at 48 h in the aforementioned publication.
A striking observation was the higher number of γH2AX foci detected in the PC-3 cell line even at the late time point of 48 h. This behaviour contrasts with its radioresistant behavior observed in the separate cell proliferation assay, where the cell line showed only minimal response to a dose of 1.5 Gy. However, the γH2AX assay demonstrated that DNA damage was indeed induced and not fully repaired

at later time points. This discrepancy between the two assays may suggest that the PC-3 cell line employs an escape mechanism to disregard DNA damage and continue proliferating. Indeed, PC-3 cells are reported in multiple studies as less radiosensitive. RNA-seq analysis identified contrasting regulation of a DNA repair and replication pathway in PC-3 versus LNCaP cells [132]. In response to radiotherapy, the radiosensitive LNCaP cells showed decreased expression of DNA repair and replication genes, whereas the radioresistant PC-3 cells increased the expression of these genes to enhance survival. Another study exploring the inherent radiation resistance of PC-3 cells concluded that these cells exhibit a deficiency in the DNA repair regulator protein p53, while LNCaP cells possess functional p53 [133]. Notably, delayed repair of DNA damage is reported in other studies for cell lines deficient in p53 [134].

Regarding the γH2AX foci characteristics after **TRT at short time points**, the β^--emitter induced similar DNA damage patterns in size as external photon irradiation. The similarities between foci induced by β^--emitters and external photon irradiation are also congruent with the dominant mechanism of DNA damage induction shared by these two radiation types. Specifically, both primarily induce DNA damage through an indirect mechanism, involving ionization of water molecules and subsequent production of ROS.
In contrast, treatment with α-emitters at early time points up to 4 h revealed characteristic track structures and larger, more intense DNA damage sites. These distinct DNA patterns are typically associated with α-particles and heavy ions, and are related to the direct and complex DNA damage induced by these particles. The observations are consistent with previous reports in the literature for the α-emitter ^{223}Ra, which attributed cell killing efficacy to the induced clustered DNA damage sites [135, 136]. Similarly, Lopez Perez et al. reported that carbon ion radiation induced larger γH2AX foci compared to photon radiation [117].

The assessment of γH2AX foci at **late time points** (up to 72 h) for **all radiation types** revealed that, similar to samples treated with external photon irradiation, γH2AX foci levels dropped for β^--emitters at the late time point at 24 h. Studies evaluating the effect of 5 MBq [^{177}Lu]Lu-DOTA-TATE for a 4 h incubation period, concluded that common radiobiological mechanisms are induced by the β^--emitter and external irradiation of 2 Gy [131]. Interestingly, these studies observed slightly different kinetics, e.g., in γH2AX foci pattern over time, with no pronounced peak in the γH2AX signal at early time points for β^--treatment, but instead a constant yet small increase.

Regarding the α-emitters, the experiments indicated that their higher biological effectiveness is strongly correlated with their potential to induce persistent DNA damage. While at earlier time point, the DNA damage across the three radiation types was comparable (for 4 h exposure time to TRT, compare Figure 5.1), it was mostly repaired at 24 h for treatment with ^{177}Lu and external photon irradiation. In contrast, the DNA damage induced by the α-emitter remained consistently high throughout all investigated time points. Notably, the two activity levels (5 and 10 kBq) did not exhibit large differences in overall behavior, giving further evidence that the amount of activity is not the primary determinant of biological effect. While, in alignment with observations at early time points, a comparison between targeted and non-targeted treatments revealed that targeted treatment is also essential for inducing consistent and maximal biological effects. Specifically, some samples receiving non-targeted treatment exhibited a slight reduction in DNA damage (refer to Figure 5.12 and 5.13).

Although no study could be found analyzing the late DNA damage after TαT in an identical setup, the overall results share common observations with findings in the **literature**. An increase in DNA damage over time (up to 24 h) was observed as well after treatment with ^{223}Ra in ovarian cancer cell lines [136]. However, ^{223}Ra (1.3 kBq/cm²) was not put in direct cell contact by incubation in the medium, but placed as an external source, which might have limited the efficacy due to a lack of internalization. The finding of an increasing number of nuclei without foci at the late time point could be related to this study design. A different study assessed the effect of DNA damage in peripheral blood mononuclear cells after internal *ex vivo* irradiation with [^{223}Ra]$RaCl_2$ (absorbed dose to the blood from 0.2 - 6.5 kBq) [137]. They observed a decrease in α-track frequency after 24 h, but overall, the number of α-tracks was still significantly increased compared to control samples. One study measured DNA damage induced by ^{225}Ac at different time points [138]. DNA damage was assessed by staining for 53BP1 foci as a marker for DSBs. Prostate cancer cell line (PSMA-positive, PC-3 PIP) were exposed for 3 h to 0.555 kBq of [^{225}Ac]Ac-PSMA-I&T or 600 kBq [^{177}Lu]Lu-PSMA-I&T. They observed an increase in DNA damage at earlier time points for both radionuclides. For the β^--emitter, the DNA damage then decreased to a level slightly above pretreatment levels at 24 h and remained constant at this level to 96 h. Comparable to findings in this work, the DNA damage induced by the α-emitter remained at a higher level but decreased as well to a level slightly above pretreatment at the 72 h observation point. However, the lower activities in this assay might have led to the slight difference in the observations in this work.

Overall, these findings underline the knowledge gaps of late DNA repair after TαT and highlight the importance of this work. These findings indicate that further investigation of later time points for the β^--emitter is necessary, as studies suggest a small amount of persistent DNA damage in contrast to treatment with external photon irradiation, despite similarities in DNA damage pattern at earlier time points. Additionally, observing DNA damage induction and repair in a live-cell imaging system would enhance deeper understanding, particularly for long-term time points. Furthermore, the staining for γH2AX does not allow differentiation between the two major repair pathways, NHEJ and HR. Therefore, to investigate these pathways specifically, it would be beneficial to use markers that are indicative of each pathway. The different radiosensitivities observed between ^{177}Lu and external photon radiation imply that different biological mechanisms may be involved [130]. Furthermore, an assessment of ROS levels after 4 h treatment with [^{177}Lu]Lu-DOTATATE and external irradiation, surprisingly revealed elevated ROS levels in only two out of six cell lines for ^{177}Lu, while four out of six cell lines displayed significantly elevated ROS levels after exposure to external irradiation [131]. This challenges the hypothesis that DNA damage caused by β^--particles is primarily mediated via the indirect effects of ROS. Therefore, the question remains as to whether the biological mechanisms of β^--emitters and external radiation are distinct or common.

6.4 Combination Therapy with DNA Repair Inhibitor

Can combination therapy with a DNA repair inhibitor improve treatment outcomes by enhancing efficacy, reducing required activities, and potentially overcoming radioresistance?

- Combination therapy with a DNA-PKi outperforms monotherapy with all irradiation types but is more effective with TRT, particularly when using α-emitters;
- In combination therapy, α-emitters exhibit a greater potential for activity reduction compared to β^--emitters;
- Even in radioresistant and non-PSMA-expressing PC-3 cells, combination therapy with α-emitters demonstrates a strong response, whereas external irradiation and β^--emitters show little to no effect.

Despite the overall success of TRT, 30–40% of patients remain unresponsive to TRT [88]. Switching from a β^--emitter like ^{177}Lu, to a more potent α-emitter can sometimes overcome therapy resistances. This was reported for neuroendocrine tumours treated with the α-emitter [^{213}Bi]Bi-DOTATOC after disease progression under [^{177}Lu]Lu-DOTATOC [139]. Similarly, patients changing to [^{225}Ac]Ac-PSMA-617 after non-responding to conventional [^{177}Lu]Lu-PSMA-617, have shown improved outcomes [140]. Unfortunately, patients receiving TαT also display treatment resistances, with 20-30% of patients poor or no response to [^{225}Ac]Ac-PSMA-617 [14, 141]. The study of Kratochwil et al. revealed uncovered mutations in genes involved in DNA damage repair and checkpoint mechanisms in biopsies from non-responsive patients [14, 141]. These patients could potentially benefit from a combination therapy of TαT and a DNA repair inhibitor to overcome treatment resistances.

Furthermore, a common side effect reported in treatment with [^{225}Ac]Ac-PSMA-617 is severe xerostomia, which can even lead to discontinuation of the therapy in 10% of patients [141]. Lowering the activity of ^{225}Ac in tandem therapy with [^{177}Lu]Lu-PSMA-617 has been shown to reduce xerostomia severity while maintaining disease control [13, 123].

Recent reviews have highlighted the potential of combining a DNA-PKi with TRT to overcome limitations associated with TRT, such as radioresistance [142]. However, this combination approach has primarily been investigated in conjunction with external irradiation, such as external beam radiation therapy (EBRT) [31]. In that study, the combination of the DNA-PKi Nedisertib®, which was also used in the scope of this work, has shown a statistically significant tumor growth inhibition in combination therapy with 2 Gy of external irradiation in a xenograft mouse model. Only two publications have explored the potential of a DNA-PKi combined with either TαT using ^{227}Th in PSMA-positive prostate cancer or TRT using ^{177}Lu in neuroendocrine tumors *in vitro* and *in vivo* [143, 144]. In both studies, the combination therapy increased antitumor efficacy compared to the corresponding monotherapy and was well tolerated without severe side effects in the mouse model.

These studies highlight the potential for combination therapies but also reveal a research gap in this area. Consequently, the primary objective of this work was to evaluate the therapeutic potential of combining the commercially available DNA-PKi Nedisertib® with two clinically relevant and established radionuclides, ^{177}Lu and ^{225}Ac, using radiopharmaceuticals targeting the PSMA in prostate

cancer, namely [^{177}Lu]Lu-PSMA-617 and [^{225}Ac]Ac-PSMA-716, in comparison to external photon irradiation. Additionally, the focus was on assessing the potential of radiosensitization and dose reduction.

The combination performed with 1.5 Gy **external irradiation** as the first trial, proved to be more effective than the monotherapy, effectively lowering cell proliferation in PSMA-positive cell lines, LNCaP and C4-2, to 36- 44% for moderate concentration of Nedisertib® (up to 1 µM), compared to control. The combination treatment still overcame the monotherapy for the PSMA-negative PC-3 cell line, but was less effective with a reduction to only 80%.
For **TRT**, with both radionuclides, the combination therapy demonstrated greater effectiveness than monotherapy with either DNA-PKi or TRT. While the combination (up to 1 µM) with 1.25 MBq/mL of β^--emitter achieved a lower reduction in cell proliferation compared to external photon irradiation (69-72%), 2.5 kBq/mL of the α-emitter demonstrated the greatest effect of all combination therapies (10-19%). Notably, even a low concentration of the DNA-PKi (0.1 µM), combined with the lowest concentration of TαT ([^{225}Ac]Ac-PSMA-716 0.156 kBq/mL), was sufficient to achieve a response comparable to that of the highest dose of TαT alone, indicating potential for dose reduction.

Comparing the characteristics of **different radiation types**, α, β^-, and external photon irradiation, it was observed that β^--emitters share similar features with external photon irradiation, similar to findings for monotherapies. In contrast, combination therapy with α-emitter yielded distinct results and demonstrated an overall higher biological effectiveness. Furthermore, the combination of [^{225}Ac]Ac-PSMA-716 and DNA-PKi had a profound impact on the most radioresistant cell line, PC-3, compared to monotherapy with ^{225}Ac, which only achieved a significant reduction in cell proliferation at the highest concentration of ^{225}Ac (51%). The reduction to 49% of cell proliferation in the combined setting is even more remarkable as the PSMA-negative cell line does not benefit from the potentiating effect internalization has for the α-emitter. This finding demonstrates that the combination therapy could also be beneficial in heterogeneous target expression environments, suggesting that this combination therapy holds promise for overcoming radioresistance associated with TαT.
As previous mentioned combination studies utilized different DNA-PKi and radiopharmaceuticals, direct comparisons to these are challenging. Furthermore, this

study is the first to directly compare the three different radiation types, α, β^- and external photon irradiation, in one setup, which allows for quantitatively distinguishing their biological effectiveness in the combined setting.

The importance of the findings presented in this work, is underscored by comparison to another recently emerged class of DNA repair inhibitors, the PARPi. Since the first FDA approval in 2014 of olaparib (Lynparza®, Astra Zeneca, Cambridge, UK), six PARPi have been approved as single agents, but despite multiple clinical trials exploring their combination with radiotherapy, none have progressed to be a successful combination therapy [145]. Moreover, preclinical evaluation of three PARPi (veliparib, olaparib or talazoparib) with TRT ([^{177}Lu]Lu-PSMA-I&T) in prostate cancer models (PC3-PIP and LNCaP) failed to demonstrate a synergistic effect on either clonogenic survival or cell viability, nor on improved tumor control compared to monotherapy in the *in vivo* model [146]. In contrast to this study, which demonstrated that combining with TRT with a DNA-PKi enhanced treatment efficacy across all three prostate cancer cell lines examined.

When establishing a combination therapy, it is crucial to consider not only the individual effects of each treatment but also potential interactions and interferences. This includes evaluating how one therapy might influence the efficacy or uptake of another and identifying synergies or antagonisms that could affect therapeutic outcomes [147]. Optimizing dose, fractionation, and scheduling is essential to avoid suboptimal efficacy or increased toxicity.
While the initial **exploration of treatment schedules** did not reveal significant differences between alternating and parallel treatments with recovery time in-between, further investigation into optimal treatment regimens and schedules is crucial for successful combination therapy, as emphasized above. For instance, one finding in this study illustrates a possible interaction in the tested combination therapy: cellular uptake assays indicated that pretreatment with the DNA-PKi may hinder the binding and internalization of TRT, suggesting that receptor expression could be affected by the pretreatment. A more detailed examination of this effect is essential to determine the optimal time interval between treatments and to ensure that the combination therapy is delivered in a manner that maximizes its therapeutic potential.

While this study provides valuable insights into the potential of combination therapy of TRT with Nedisertib® in prostate cancer, it is essential to acknowledge certain limitations that may influence the broader applicability of these findings.

Since conventional 2D cell cultures do not accurately replicate biological conditions, *in vitro* experiments using 3D spheroids provide a valuable intermediate model for gaining insights before progressing to *in vivo* studies. To evaluate the detailed mechanism of the combination therapy, further biological assays like DNA damage assessment would be helpful. Moreover, additional *in vitro* and *in vivo* studies should be conducted to refine the understanding of the therapeutic potential of this combination and optimize treatment schedule. Notably, as demonstrated by the experiments with the PARPi the specific findings regarding p53 expression in the prostate cancer cell lines utilized,the treatment outcome of combination therapy depends strongly on the biological model used. Therefore, its efficacy needs to be determined specifically for each model, making translation challenging. Furthermore, interactions in an *in vivo* model are more complex and therefore results can differ from *in vitro* experiments.

In conclusion, this study provides evidence for an enhancement of treatment efficacy when combining TRT and DNA-PKi Nedisertib®, and demonstrates potential for activity reduction, particularly in combination with α-emitters. Furthermore, the treatment outcomes observed in the PSMA-negative and radioresistant PC-3 cell line suggest that this combination therapy may help overcome radioresistance. Building on the success of this proof-of-concept study, further investigations are necessary to elucidate the additive or synergistic effects of combination therapy and optimize treatment conditions. Since both therapies have been previously evaluated as monotherapies in preclinical models, this facilitates the design and implementation of studies aimed at translating the combination approach into an *in vivo* setting. Additionally, one clinical trial (Phase 1/Phase 2) is currently investigating the combination of [^{223}Ra]$RaCl_2$ (Xofigo®) with Nedisertib® in patients with mCRPC (NCT04071236).

7 Closing

7.1 Key Findings and Impact

This work aimed to bridge the knowledge gap in radiobiology of TRT. This knowledge is indispensable for optimizing TRT to meet the specific needs of each patient case, enabling informed decision-making that leads to effective treatment while utilizing the limited amount of radionuclides efficiently. Furthermore, a precise understanding of radiobiological mechanisms and biological effectiveness is crucial for increasing treatment efficacy and managing side effects, e.g., by lowering the administered activity. Particularly in combination treatments, which represent the next steps in advancing TRT in clinical applications, it is imperative to gain detailed insights into the radiobiology of TRT. This knowledge will also facilitate the selection of the most beneficial and promising candidates for combination therapy, allowing for the alignment of treatment regimens and schedules.

The study identified key differences between the α-emitter ^{225}Ac and the β^--emitter ^{177}Lu. While cellular internalization was found to be the most critical parameter determining biological effectiveness for the short-range α-emitter, activity and exposure time were deemed more relevant for the long-range β^--emitter, with internalization playing a relatively minor role. These findings have important implications for the future development of radiopharmaceuticals tailored to the specific characteristics of the desired radionuclide. Furthermore, internalization properties should be carefully considered in a clinical setting when transitioning from one emitter type to another, such as switching from [^{177}Lu]Lu-PSMA-617 to [^{225}Ac]Ac-PSMA-617. Specifically, the α-emitter can only lead to improved clinical outcomes if adequate internalization of the radiopharmaceutical is ensured.
Moreover, observations of DNA damage at later time points (up to 72 h) revealed valuable insights into biological repair mechanisms which differ distinctly for α- and β^--emitters. The severity of α-induced DNA damage was prominent in the persistent DNA damage across all time points, whereas β^--induced DNA damage regressed over time. While results in DNA damage and cell proliferation assays

suggested that common features are shared between β^--emitters and external photon irradiation, further literature research indicated potential differences in the underlying biological response, as evidenced by distinct radiosensitivities to both radiation types in different cell lines and unexpectedly low ROS levels in β^--treated cell lines [130, 131]. This underscores the importance of studying DNA damage over time and other biological endpoints, such as cell proliferation. Understanding the differences in biological response is crucial for identifying suitable targets for combination therapy and designing effective treatment schedules.
Furthermore, the combination therapy of TRT and the DNA repair inhibitor Nedisertib® demonstrated the potential benefits of a combined treatment approach for dose reduction (thereby minimizing side effects) and overcoming radioresistances (expanding the therapeutic range to additional patients). Given that studies thoroughly investigating combination therapies with TRT are scarce, and combination therapy with PARPi has not shown the desired effect [146], further strategies are urgently needed. The results of this work provide evidence for this approach, and experiments should be expanded to fully explore its potential.
Lastly, research on designing a single-cell simulation to estimate absorbed dose as a function of subcellular radionuclide localization revealed the challenges and complexity inherent in this field, but also highlighted the need and relevance for such a simulation. In particular, the finding of high unspecific binding of non-targeted activity is highly relevant for the community, as it can be a confounding factor in accurately determining the uptake behavior of a radiopharmaceutical. Neglecting the effect of impurities on radiochemical yield when designing experiments could lead to biased and unreliable results.
In summary, this work provided valuable insights into the radiobiological mechanisms of TRT, with direct implications for the development of radiopharmaceuticals and promising strategies for combination therapies aimed at optimizing TRT. By systematically evaluation of TRT using both α- and β^--emitters within a consistent experimental framework, this study enables quantitative comparisons between these radiation types, as well as against external photon irradiation, the gold standard in radiobiology. Therefore, this study stands out among previous work. Additionally, by assessing non-targeted radiation effects as a baseline, a factor often overlooked, this research highlighted the critical importance of targeting and internalization for each emitter type, along with the necessity of radiochemical purity. The long-term observation of DNA damage and additional endpoint of cell proliferation complemented each other, offering a comprehensive understanding of biological mechanisms and repair dynamics. Finally, this study represents

the first successful implementation of combination therapy involving TRT and a DNA-PKi in prostate cancer cell lines. These findings lay the groundwork for further investigations into this therapeutic approach both *in vitro* and *in vivo*, paving the way for future advancements in TRT.

In the long-term perspective, these findings will hopefully contribute to better-tolerated and more effective cancer treatments. The ultimate goal is to shift the perception of cancer from an uncertain, life-threatening, and frightening disease to a severe but effectively manageable condition. As fear of the unknown often prevents people from taking advantage of early screening and prevention programs, a less fearful picture of cancer could motivate individuals to participate in screening programs more readily. This could lead to overall earlier detection of cancer and improve the chances of successful therapy.

7.2 Future Directions

Based on the key findings of this work discussed previously and the comparison with reports in the literature, the next logical steps are outlined in the following.

Considering the DNA damage assessment, further investigation into DNA repair dynamics at late time points (up to 72 h) for the β^--emitter ^{177}Lu could provide more clarity on the biological mechanisms compared to external photon irradiation. Moreover, after thorough evaluation of different concentrations of activity of TRT and DNA-PKi compound via the cell proliferation assays, assessing DNA damage for the most promising combinations in comparison to monotherapy could provide valuable insights into the underlying mechanism leading to the improved treatment outcomes observed. Performing the DNA damage assay with a low and moderate concentration of activity (1-10 kBq) and low concentration of DNA-PKi (0.1 and 1 µM) and could also further illuminate the potential for activity reduction while maintaining treatment efficacy. Especially, observations of DNA damage at late time points (up to 72 h) should be taken into account.
While this work has given the first evidence of the benefits in treatment outcome of a combined treatment of TRT and DNA-PKi, further experiments should be conducted to gain evidence on the additive or synergistic effect of this combination. Moreover, as emphasized by the literature, studies should be carried out to determine the most effective treatment schedule. The experiments in this work evaluated the optimal treatment regime for activity concentrations and DNA-PKi con-

centrations. Therefore, the next step is to investigate the sequence of treatment and the potential effect of recovery time between treatments. A question remaining after initial experiments on treatment schedule is the impact of preincubation with DNA-PKi on internalization of radiopharmaceutical, a mechanism which proved crucial for the α-emitters. Additionally, evaluating first-line treatment with TRT followed by incubation of DNA-PKi was not feasible due to laboratory organization and equipment constraints. Therefore, the effect of this treatment order should be assessed in future studies.

While results on the radioresistant PC-3 cell line have shown potential for the combined treatment to overcome radioresistance, further evaluation in this direction should be conducted. Potentially, the combination therapy could be expanded to other cell lines reported to be radioresistant as well. To further investigate radioresistance, alternative approaches should incorporate 3D cell cultures or spheroid models, which replicate the tumor microenvironment more accurately. Studies have indicated that the tumor microenvironment plays a decisive role in the mechanisms underlying radioresistance. For instance, increased antioxidative activity induced by the tumor microenvironment has been proposed as a mechanism of resistance in both preclinical and clinical studies of neuroendocrine tumors treated with [^{177}Lu]Lu-DOTATATE [148]. This enhanced antioxidative response helps to neutralize ROS produced by radiation, thereby reducing DNA damage in cancer cells.

In vitro evaluation of the most effective treatment regime is especially relevant for follow-up *in vivo* studies and determining ideal conditions. To translate the combination therapy into clinics, *in vivo* studies are essential. Furthermore, these studies will also be necessary to assess potential side effects of the combined treatment, which are critical to judge the translation potential of this therapy.

Regarding the simulation framework, whose development was initiated, the outlined modifications should be implemented in the model. Estimation of the deposited energy and absorbed dose would be most interesting, as it allows for further comparison with other studies. Furthermore, the expansion to a multi-cell model should be prioritized, as only a multi-cell model fits the needs of a long-range β^--emitter and can determine the influence of the crossfire effect. Moreover, the unspecific binding of non-targeted radionuclides is not understood yet and requires further investigation. Experiments performed with chelated activity, which did not express the unspecific binding, led to the hypothesis of unspecific binding related to a charge effect of charged ions and the bipolar cell membrane. Additionally, literature research revealed that the effect is not consistent for each ra-

dionuclide, as the phenomenon was not observed for [^{111}In]$InCl_3$ and [^{68}Ga]$GaCl_3$ [127]. Therefore, conducting similar assays with other radionuclides and potentially with chelators that alter the overall charge of the system differently could be highly relevant for unraveling the mechanism behind this effect.

Finally, following these concrete experiments that extend the current studies, additional ideas for future experiments - beyond the scope of this project - have emerged. A study performed on U2O2 cells reported significant changes in DNA damage characteristics and dynamics, when α-radiation was combined with external photon irradiation [149]. Foci observed in this combined treatment were larger, and their movement was strongly attenuated in this treatment regime. In contrast, foci induced by a pretreatment with external irradiation followed by α-exposure, declined quickly. Therefore, evaluating an interaction between the different radiation types is proposed as a promising combination therapy as well. Furthermore, *in vitro* studies combining α- and β^--emitters could provide valuable insights and contribute to optimizing dual TRT treatment modalities, which are currently evaluated in clinical trials. Moreover, live-cell imaging of γH2AX foci could provide deeper insights into the repair dynamics between the different radiation types.

In summary, this work provided fundamental knowledge that contributes essential pieces to the puzzle of unraveling the radiobiological mechanisms behind TRT. However, it also reveals more questions about the unique mechanisms underlying TRT. The puzzle is not solved yet, but its complete picture will eventually emerge through the collective efforts of many researchers, driven by creativity and collaboration - as exemplified by the interdisciplinary approaches and vivid scientific discussion and inter-institutional exchange which have guided and shaped this thesis.

Appendices

A Protocol DNA Damage Induction and Repair via Immunofluorescent Microscopy

- Cell lines: LNCaP, C4-2, PC-3

- Cell culture (from PAN Biotech): phosphate-buffered saline (PBS; pH 7.4, #P04-36500), Roswell Park Memorial Institute 1640 medium (RPMI-1640 #P04-16500) supplemented with 10% fetal calf serum (FCS, #P40-37500) and 1% L-glutamine (L-GLN, #P04-82100) and 0.05% trypsin (#P10-023100) for cell detachment

- Neubauer cell counting slide (#4668323, Th. Geyer), cell culture insert with 0.4 µm transparent PET membrane (sterile, #353095) and 24-well TC treated companion plate (sterile, #353504, Falcon®)

- Treatment: compounds PSMA-617 and analogue PSMA-macropa; radionuclides ^{225}Ac, ^{223}Ra, ^{227}Th, ^{177}Lu in solution, buffers for radiolabeling and rp-TLC for labeling control (TLC Silica gel 60 RP-18 F_{254}s, #1055600001, Merck, Darmstadt, Germany); liquid phase Na citrate 0.1 M, pH 5.5

- Fixation and permabilization: fixation solution 3% paraformaldehyde (PFA) in PBS (non supplemented w/o Calcium, Magnesium); permeabilization 0.5% Triton X-100 in dPBS; for wash dPBS (non sterile)

- Immunofluorescent staining: primary γH2AX antibody (#BLD-613402, Biozol), secondary AlexaFluor™ 488-labeled antibody (#AB_2534088, Thermo Fisher Scientific), cell nucleus staining with DAPI (4',6-Diamidin-2-phenylindol, #D1306, Thermo Fischer Scientific), Image-iT FX signal enhancer (#I36933, Thermo Fischer Scientific), mounting medium Fluoromount G (#SBA-0100-01, Biozol Diagnostica), coverslips (round, 12 mm) and microscopy slides (76 x 26 mm). Washing solution: 0.5% BSA (Bovine Serum Albumin, # A2153, Sigma-Aldrich) in dPBS; Blocking solution: 3% BSA in dPBS with 0.3% Triton X-100; Solution for antibody dilution 3% BSA in dPBS

A.1 Procedure

Cell Culture - One Day Prior to Treatment

- Remove medium from flask, wash with PBS, and trypsinize. Stop trypsinization with medium and centrifuge cells 5 min at 200 rcf. Remove the remaining medium and resuspend the pellet in medium. Count the cells via a Neubauer cell counting slide.

- For each cell line (LNCaP, C4-2, PC3) prepare a solution of $1.6 \cdot 10^5$ cells mL^{-1} in supplemented RPMI-1640.

- Seed cells with total volume of 300 µL of cell solution and incubated until experiment next day (37 °C, 5% CO_2).

Treatment with Radioactivity

- Perform radiolabeling under the defined conditions (Table 4.1) and check via rp-TLC that radiochemical yield is above 99% for ^{177}Lu and 96% for ^{225}Ac.

- For both, radiopharmaceuticals and free radionuclides, prepare solutions with specified activities (Table 4.2) in supplemented RPMI-1640 (total activity per solution depends on the number of samples; calculate 300 µL per sample plus safety margin of 10% of total volume)

- Remove medium in inserts and replace with 300 µL per insert of prepared activity solutions. Incubate cells for 4 h at 37 °C, 5% CO_2. During incubation time, you may distribute inserts with spatial distance on multiple companion plates to limit cross-irradiation (especially relevant for samples with total activity of 100 kBq).

- After 4 h, remove active medium and replace with usual, supplemented medium. Depending on the planned experiment, start directly with sample fixation and permeabilization or reincubate samples until a defined fixation time point.

Fixation and Permeabilization

- Prepare solutions for fixation and permeabilization ahead of the experiment. Fixation solution (3% PFA/PBS) can be stored aliquoted at −20 °C (avoid re-freezing), permeabilization should be prepared on experimental day or one day prior.
- Discard medium and wash once with 200 µL of dPBS per insert.
- Fixate cells with 200 µL of 3% PFA/PBS per insert for 15 min at room temperature.
- Discard fixation and wash once with 200 µL of dPBS per insert.
- Permeabilize with 200 µL of 0.5% Triton X-100/PBS per insert for 30 min at room temperature.
- Discard permeabilization and add 200 µL of PBS per insert. Store parafilm-covered 24-well plates in fridge at 4 °C until immunofluorescent staining (maximum one week).

Immunofluorescent Staining for γH2AX

- Prepare solutions for washing, blocking, and antibody solution freshly before starting with the staining procedure and store at 4 °C during the different steps of the staining procedure

Primary antibody staining

- Discard PBS and incubate each insert with one droplet of Image-iT FX Signal Enhancer for 30 min at room temperature.
- Discard signal enhancer and wash three times with 200 µL per insert of washing solution (0.5% BSA/PBS) for 5 min.
- Incubate with 200 µL of blocking solution (3% BSA/PBS + 0.3% Triton X-100) per insert for 30 min at room temperature.
- Incubate samples overnight at 4 °C with 50 µL per samples of primary γH2AX antibody diluted 1:2000 in 3% BSA/PBS. Cover plates with parafilm to prevent drying of samples.

Secondary Antibody Staining

- Remove primary antibody and wash three times with 200 µL per insert of washing solution (0.5% BSA/PBS) for 5 min.
- Incubate samples for 1 h in the dark at room temperature with 50 µL per samples of secondary AlexaFluor488 labeled antibody diluted 1:250 in 3% BSA/PBS. Cover plates with parafilm to prevent drying of samples.

DAPI Staining and Embedding

- Remove secondary antibody and wash three times with 200 µL per insert of washing solution (0.5% BSA/PBS) for 5 min.
- Wash once with 200 µL per insert with deionized H_2O (milliQ).
- Incubate each sample for 15 min in the dark at room temperature with 50 µL of 1 µg mL^{-1} DAPI in H_2O.
- Rinse again with deionized H_2O. Cut out the membrane with a sharp scalpel and mount the sample with Fluoromount G on a glass slide with a coverslip.
- Let samples dry at least overnight at room temperature in the dark before microscopy. Store samples until further processing at 4 °C.

A.2 Parameters MATLAB processing

Table A.1: **Parameters for the nuclei segmentation:** list of the parameter settings used in the analysis performed with the script `selectNuclei_v1` for segmenting nuclei in DAPI-stained images. Each parameter is accompanied by its corresponding value and a brief description.

Parameter	Value	Description
Image Input		
imgType	0	Single field of view
Preprocessing		
removeNuclearStainBG	1 (true)	Apply top-hat filter to remove background from nuclear image
removeNoise	1 (true)	Apply median filter before segmenting nuclei to get smoother edges
sharpenNimg	1 (true)	Sharpen image to improve edge detection
Segmentation		
intTHsteps	1	Number of intensity threshold steps
Segmentation - intTHsteps options		
intTHmode	[4 0 0]	Use local thresholding based on average filter and offset defined in `localTHoffset`; efficient 1-step strategy without background removal or edge refinement
intTH	[1500 1100 700]	Minimum absolute DAPI intensity. Only used if `intTHmode == 0` or 5
localTHoffset	0.05	Offset for local thresholding; should be between 0 and 1
refineEdges	1 (true)	Enable border refinement of nuclei
refineEdgeTH	0.1	Edge threshold used during border refinement
separateTouchingNuclei	1	Try to separate touching nuclei regardless of size; works even if object fails area filters

Parameter	Value	Description
Segmentation – further parameters		
useEdgeDetection	0 (false)	Edge detection is disabled
maxGapLength	25	Not relevant because `useEdgeDetection` is disabled
minNucleusArea	800	Minimum area of detected nucleus [px]
maxNucleusArea	5000	Maximum area of detected nucleus [px]
maxAspectRatio	2.5	Ratio of major axis length to minor axis length
minCompactness	0.5	Nucleus area divided by bounding box area
minCircularity	0.8	1 = perfect circle
minSolidity	0.8	Area divided by convex hull area (1 = convex object)
maxIrregularity	100	Maximum ratio of missing pixels compared to elliptic fit
maxConcavityDepth	14	Maximum minimal distance between contour and convex hull
maxIntegralConcavityDepth	1.5	Normalized sum of all concavity depths around contour
maxEllipticDeviation	0.25	Non-overlapping area with equivalent ellipse / overlapping area
maxEccentricty	0.5	0 = circle, 1 = line
minSharpness	150	Minimum sharpness index; helps remove out-of-focus nuclei
maxSharpness	700	Maximum sharpness index; helps remove mitotic or overly sharp nuclei
frqTh	0.1	Possibly a frequency threshold (context not fully specified)
borderExtensionBG	10	Border extension applied to exclude signals from background [px]
Marker-specific Analysis		
markerSpecificAnalysis	0 (false)	No additional staining used; disables marker-based analysis

Parameter	Value	Description
Background Signal Analysis		
bgFilterMode	[1, 0, 0]	Switch for defining max allowed background intensity. 0: use `maxBG` and `maxHighBGfrq`, 1: use estimated median $\times$ `maxBGfactor`
maxBG	[4000, 3000, 3000]	Maximum allowed background intensity for each signal channel (excluding DAPI). Used if `bgFilterMode == 0`
maxHighBGfrq	[0.2, 0.2, 0.2]	Max frequency of pixels exceeding `maxBG` relative to non-zero pixels in background region
maxBGfactor	[2.5, 1.3, 1.4[	Factor applied to global median background intensity. Used if `bgFilterMode == 1`

Table A.2: **Parameters for γH2AX foci segmentation:** Configuration settings for the `AnalyzeFoci_v1_1C.m` script used for segmenting of γH2AX foci. Each parameter is listed with its value and a short description.

Parameter	Value	Description
General Foci Segmentation Parameters		
removeBG	3	Local background subtraction using a Gaussian filter. The blurred image is subtracted from the original, and the result is rescaled to the original maximum intensity.
equalizeFociInt	0	No equalization of foci intensities applied.
equalizeFociOpt	[ ]	No additional options specified for intensity equalization.
segMethod	2	Seed-based segmentation with local signal-to-noise filtering for foci validation.
intTH	30	Intensity threshold for foci detection (meaning depends on `THmethod`).
THmethod	3	`intTH` is interpreted as a percentage of the maximum intensity of each individual image. Higher values reduce foci detection.

Parameter	Value	Description
Intensity Threshold-Based Segmentation		
histoPmaxLevel	10	Upper histogram level used in thresholding.
maxScale	10	Maximum intensity scaling factor (in %) to enhance dim foci.
satPx	200	Maximum number of saturated pixels allowed when scaling, limiting oversaturation that would impair segmentation of bright foci.
Seed-Based Segmentation Parameters		
HmaxTH	5	H-maxima transform threshold to identify seed regions. Higher values yield larger seeds.
seedsTH	0.01	Threshold for expanding seeds to approximate full foci size. Higher values enlarge masks but may reduce separation quality.
minSNratio	1.3	Minimum signal-to-noise ratio: average seed intensity must be 1.3× higher than average pannuclear intensity.
Post-processing and Size Filtering		
ws	1	Enable watershed segmentation to separate overlapping foci. Applicable to all segmentation methods.
minSize	8	Minimum number of pixels for an object to be counted as a focus.
maxSize	120	Maximum number of pixels for an object to be counted as a focus.

B Protocol Cellular Uptake Assay

B.1 Material

- Cell lines: LNCaP, C4-2, PC-3
- Cell culture (from PAN Biotech): phosphate-buffered saline (PBS; pH 7.4, #P04-36500), Roswell Park Memorial Institute 1640 medium (RPMI-1640 #P04-16500) supplemented with 10% fetal calf serum (FCS, #P40-37500) and 1% L-glutamine (L-GLN, #P04-82100) and 0.05% trypsin (#P10-023100) for cell detachment
- Neubauer cell counting slide (#4668323, Th. Geyer), 24-well culture treated plate
- Poly-L-Lysin-hydrobromid (#P6282, Merck)
- Treatment: compounds PSMA-617 and analogue PSMA-macropa; radionuclides ^{225}Ac, ^{223}Ra, ^{227}Th, ^{177}Lu in solution, buffers for radiolabeling and rp-TLC for labeling control (TLC Silica gel 60 RP-18 F_{254}s, #1055600001, Merck, Darmstadt, Germany); liquid phase Na citrate 0.1 M, pH 5.5.
- Glycin buffer (50 mM); pH 2.8; NaOH (0.3 M; pH 14); dPBS (non sterile)

B.2 Procedure

Cell Culture - One Day Prior to Treatment

- Coat each well of 24-well plate with 500 µL of Poly-L-Lysin (5 mg dissolved in 50 mL of sterile H_2O). Leave Poly-L-Lysin for 30 min, then wash once with sterile PBS and cover plates with PBS until seeding.
- Remove medium from flask, wash with PBS and trypsinize. Stop trypsinization with medium and centrifuge cells 5 min at 200 rcf. Remove the remaining medium and resuspend the pellet in medium. Count the cells via a Neubauer cell counting slide.
- Prepare a solution of $1 \cdot 10^5$ cells mL^{-1} in supplemented RPMI-1640 for C4-2 and PC-3, $2 \cdot 10^5$ cells mL^{-1} for LNCaP

- Seed cells with total volume of 1 mL of cell solution and incubated until experiment next day (37 °C, 5% CO_2).

Treatment with Radioactivity

- Perform radiolabeling under the defined conditions (Table 4.1) and check via rp-TLC that radiochemical yield is above 99% for ^{177}Lu and 96% for ^{225}Ac.
- For both, radiopharmaceuticals and unlabeled radionuclides, prepare solutions with specified activities (calculate 250 µL per sample plus a safety margin of 10% of the total volume) with supplemented RPMI-1640.
- Remove medium in well and incubate cells with 250 µL per well with activity solution for specific time (1- 4 h) at 37 °C, 5% CO_2.

Cellular Uptake Assay

- Prepare Glycin buffer and NAOH shortly before assay (either during incubation or one day before)
- Remove active medium and wash three times with 500 µL ice-cold dPBS.
- Collect membrane-bound fraction in two 5 min washes with 500 µL Glycin buffer, place fraction into gamma counter tubes.
- Wash once with 500 µL ice-cold dPBS.
- Collect internalized fraction by lysation of cells with 500 µL NaOH. Pipette the fraction up and down several times to rinse the bottom of the well to collect the complete lysate. Place the collected fraction again in gamma counter tubes.
- Measure fractions and standards of incubation solution in the gamma counter.

C Protocol Effect of Mono- and Combination Therapy on Cell Proliferation

C.1 Material

- Cell lines: LNCaP, C4-2, PC-3
- Cell culture (from PAN Biotech): phosphate-buffered saline (PBS; pH 7.4, #P04-36500), Roswell Park Memorial Institute 1640 medium (RPMI-1640 #P04-16500) supplemented with 10% fetal calf serum (FCS, #P40-37500) and 1% L-glutamine (L-GLN, #P04-82100) and 0.05% trypsin (#P10-023100) for cell detachment
- Neubauer cell counting slide (#4668323, Th. Geyer), 96-well flat bottom plates (sterile cell culture plate with flat bottom, color: black with transparent bottom, #644090, Kisker Biotech).
- Treatment: compounds PSMA-617 and analogue PSMA-macropa; radionuclides ^{225}Ac, ^{223}Ra, ^{227}Th, ^{177}Lu in solution, buffers for radiolabeling and rp-TLC for labeling control (TLC Silica gel 60 RP-18 F_{254}s, #1055600001, Merck, Darmstadt, Germany); liquid phase Na citrate 0.1 M, pH 5.5;
  DNA-PKi Nedisertib (M3814, Peposertib, MSC2490484; #S8586, Selleckchem)
- Resazurin sodium salt (#10053737, Th. Geyer)

C.2 Procedure

Cell Culture - One Day Prior to Treatment

- Remove medium from flask, wash with PBS, and trypsinize. Stop trypsinization with medium and centrifuge cells 5 min at 200 rcf. Remove the remaining medium and resuspend the pellet in medium. Count the cells via a Neubauer cell counting slide.
- For each cell line (LNCaP, C4-2, PC3) prepare a solution of desired density in supplemented RPMI-1640 (LNCaP: 1750 cell per well, $1.17 \cdot 10^4$ cells mL^{-1}, C4-2: 1300 cell per well, $8.67 \cdot 10^3$ cells mL^{-1}, PC-3: 1000 cell per well, $6.67 \cdot 10^3$ cells mL^{-1}).

- Seed cells with total volume of 150 µL of cell solution and incubated until experiment next day (37 °C, 5% CO_2).
- For statistical purpose, seed at least triplicates for each experiment condition

Mono- and Combination Treatments

Different treatments were performed at various time points (either Day 1 or Day 2 after seeding). Details of how the various treatments were prepared and carried out are given below.

External ohoton irradiation

- Place plates at Shelf 4 of the Multirad225-X-ray Faxitron and irradiate at the referred times for specific doses (refer to Table 4.3).
- Reincubate plates directly after irradiation, no change of medium.

DNA repair inhibitor (DNA-PKi Nedisertib)

- Prepare initial stock according to manufacturer instructions, the stock solution of 1000 µM is prepared with DMSO (Dimethylsulfoxid) (5 mg in 1.038 mL DMSO, molecular weight Nedisertib 481.91 g mol^{-1})
- From stock prepare dilution with supplemented RPMI-1640 for concentrations used in the experiments (refer to Table 4.3). Prepare a DMSO control, whose concentration is equal to the DMSO concentration of the highest concentration used in the experiment
- For the total volume of concentration solutions, calculate with 150 µL for each sample per concentration and add a safety margin of 10% of the total volume.
- For treatment, remove medium and replace by 150 µL per well of DNA-PKi concentrations. Incubate cells for 24 h at 37 °C, 5% CO_2. After 24 h, remove DNA-PKi-supplemented medium and replace it with the usual, supplemented medium. Depending on the experimental design, continue with additional treatment or reincubate cells until the experimental endpoint.

Targeted radionuclide therapy

- Perform radiolabeling under the defined conditions (Table 4.1) and check via rp-TLC that radiochemical yield is above 99% for ^{177}Lu and 96% for ^{225}Ac.
- For both, radiopharmaceuticals and free radionuclides, prepare solutions with specified activities (Table 4.3) in supplemented RPMI-1640 (total activity per solution depends on the number of samples; calculate 150 µL per sample plus a safety margin of 10% of the total volume)
- Remove medium and replace with 150 µL per well of prepared activity solution. Incubate cells for 4 h at 37 °C, 5% CO_2. After 4 h, remove the active medium and replace it with the usual, supplemented medium. Reincubate plates until the endpoint of the experiment.

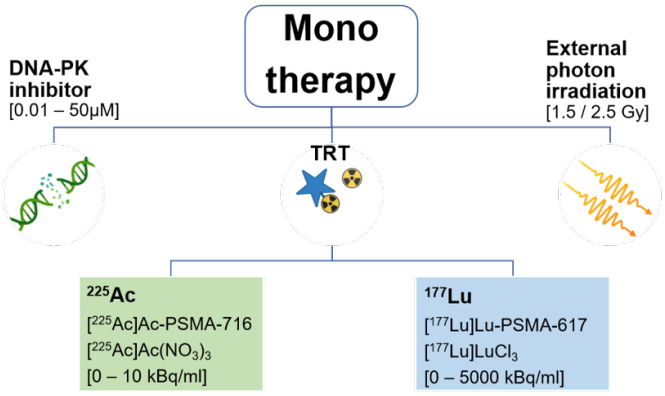

(a) Monotherapy treatments

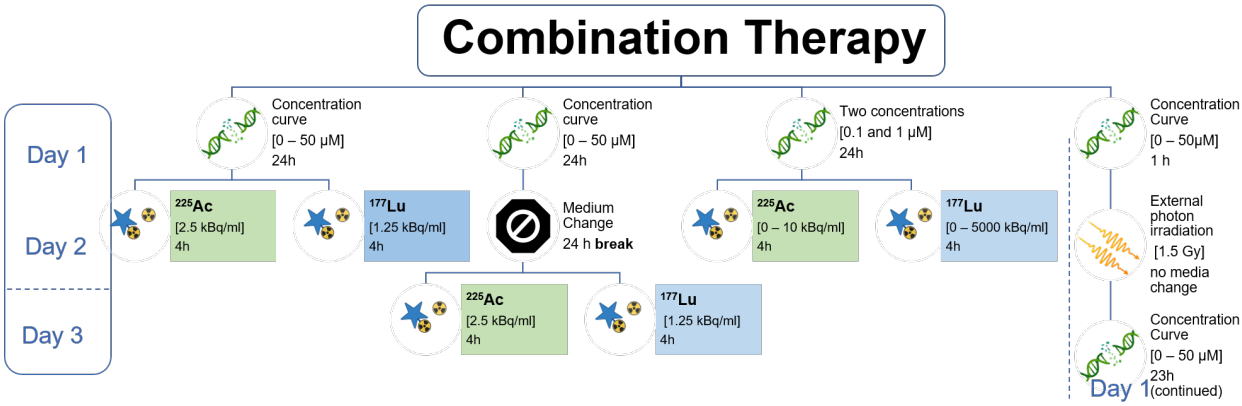

(b) Combination therapy treatments

Figure C.1: **Cell proliferation - overview of treatment procedures:** Monotherapy (a) and Combination Therapy (b) are depicted with used concentrations. Treatment with radionuclides involdes treatment with targeted compounds as well as non-complexed radionuclides

Resazurin Assay

- Prepare a stock solution of resazurin. Dissolve 15 mg of resazurin powder in 100 mL of PBS (pH 7.4). Filter sterilized solution and store in aliquots at −20 °C.
- For measurement of cell proliferation, prepare a solution of supplemented RPMI-1640 with 10% of resazurin stock solution (calculate with 150 µL of medium and 15 µL of resazurin, thus in total 165 µL per sample for total volume).
- Remove medium and replace with 165 µL of resazurin dilution. Incubate plates at 37 °C, 5% CO_2 for 2.5 h.
- After 2.5 h measure fluorescence signal of plates in plate reader (excitation: 530 nm and emission: 590 nm). Measure each plate five time for statistical purpose.

List of Figures

List of Tables

Scientific Publications

The following lists journal publications and conference proceedings that were published during this PhD project. The work of the journal publications is not part of this thesis. The content of the following conference proceedings is included in this thesis.

Journal Publications

R. C. Winter, M. Amghar, A. S. Wacker, G. Bakos, H. Taş, M. Roscher, J. M. Kelly and M. Benešová-Schäfer, “Future Treatment Strategies for Cancer Patients Combining Targeted Alpha Therapy with Pillars of Cancer Treatment: External Beam Radiation Therapy, Checkpoint Inhibition Immunotherapy, Cytostatic Chemotherapy, and Brachytherapy", Pharmaceuticals **17**, 10.3390/PH17081031 (2024).

U. Bauder-Wüst, M. Schäfer, R. Winter, Y. Remde, M. Roscher, H. Breyl, T. Poethko, C. Tömböly and M. Benešová-Schäfer, “Synthesis of tritium-labeled Lu-PSMA-617: Alternative tool for biological evaluation of radiometal-based pharmaceuticals", Applied Radiation and Isotopes **197**, 10.1016/J.APRADISO.2023.110819 (2023).

Conference Contributions

R. C. Winter, U. Bauder-Wüst, M. Schäfer, Y. Remde, M. Roscher, S. V. Selivanova, R. L. Perez and M. Benešová-Schäfer, “P-167: DNA Damage in 225Ac- and 177Lu-based Targeted Radionuclide Therapy: A Comparison of Targeted and Non-Complexed Radionuclide Delivery", In Proceedings of the 26th International Symposium on Radiopharmaceutical Sciences iSRS May 11-15 **Poster** (2025).

R. C. Winter, U. Bauder-Wüst, M. Schäfer, Y. Remde, M. Roscher, R. L. Perez and M. Benešová-Schäfer, “EP-0002: In Vitro Study on DNA Damage Induction by Targeted Radionuclide and External Radiotherapy compared to DNA Damage Simulation using GEANT4 DNA", In Proceedings of the EANM’23 Abstract Book Congress Oct 19-23 **Poster** (2024).

R. C. Winter, U. Bauder-Wüst, M. Schäfer, Y. Remde, M. Roscher, R. L. Perez and M. Benešová-Schäfer, “In Vitro DNA Damage Induction in Targeted Radionuclide and External Radiotherapy", In Proceedings of the 30. AGRR, 2. grpw e.V. Jahrestagung 19-21.9 **Talk** (2024).

R. C. Winter, U. Bauder-Wüst, M. Schäfer, M. Roscher, R. L. Perez and M. Benešová-Schäfer, “EPS-210: In Vitro Evaluation of Radiation-induced DNA Damage and Repair within Targeted Radionuclide Therapies in Comparison to External Radiation", In Proceedings of the EANM’23 Abstract Book Congress Sep 9-13 **Poster** (2023).

R. C. Winter, U. Bauder-Wüst, M. Schäfer, M. Roscher, R. L. Perez and M. Benešová-Schäfer, “P-114: Radiation-induced DNA Damage and Repair in Targeted Radionuclide Therapies in Comparison to External Beam Radiation", In Proceedings of the 25th International Symposium on Radiopharmaceutical Sciences iSRS May 22-26 **Poster** (2023).

Bibliography

[1] "Angst vor Krankheiten 2024", https://caas.content.dak.de/caas/v1/media/86256/data/1ec9f4841b483e1a204ebe7688457db6/241202-download-forsa-angst-vor-krankheiten.pdf (visited on 21/07/2025).

[2] "Todesursachen in Deutschland - Statistisches Bundesamt", https://www.destatis.de/DE/Themen/Gesellschaft-Umwelt/Gesundheit/Todesursachen/%7B%5C_%7Dinhalt.html (visited on 21/07/2025).

[3] "Global cancer burden growing, amidst mounting need for services", https://www.who.int/news/item/01-02-2024-global-cancer-burden-growing--amidst-mounting-need-for-services (visited on 21/07/2025).

[4] "Cancer Tomorrow", https://gco.iarc.who.int/tomorrow/en/dataviz/trends?multiple%7B%5C_%7Dpopulations=1 (visited on 21/07/2025).

[5] "Cancer care 2025: an overview of cancer outcomes data across Europe", https://www.efpia.eu/news-events/the-efpia-view/statements-press-releases/ihe-cancer-comparator-report-2025/ (visited on 21/07/2025).

[6] M. S. Hofman et al., "[177Lu]-PSMA-617 radionuclide treatment in patients with metastatic castration-resistant prostate cancer (LuPSMA trial): a single-centre, single-arm, phase 2 study", The Lancet Oncology **19**, 10.1016/S1470-2045(18)30198-0 (2018).

[7] C. Kratochwil, F. Bruchertseifer, H. Rathke, M. Hohenfellner, F. L. Giesel, U. Haberkorn and A. Morgenstern, "Targeted α-Therapy of Metastatic Castration-Resistant Prostate Cancer with 225Ac-PSMA-617: Swimmer-Plot Analysis Suggests Efficacy Regarding Duration of Tumor Control", Journal of Nuclear Medicine **59**, 10.2967/JNUMED.117.203539 (2018).

[8] F. Mendes, S. Y. Terry, D. Spiegelberg, B. Cornelissen, J. Bolcaen and J. Nonnekens, "Recommendations for reporting preclinical radiobiological studies in targeted radionuclide therapy", European Journal of Nuclear Medicine and Molecular Imaging, 10.1007/S00259-025-07152-Y (2025).

[9] C. Stokke, M. Kvassheim and J. Blakkisrud, "Radionuclides for Targeted Therapy: Physical Properties", Molecules **27**, 10.3390/MOLECULES27175429/S1 (2022).

[10] H. Dadgar et al., "Targeted radioligand therapy: physics and biology, internal dosimetry and other practical aspects during 177Lu/225Ac treatment in neuroendocrine tumors and metastatic prostate cancer", Theranostics **15**, 10.7150/THNO.107963 (2025).

[11] M. Grzmil, P. Boersema, A. Sharma, A. Blanc, S. Imobersteg, M. Pruschy, P. Picotti, R. Schibli and M. Behe, "Comparative analysis of cancer cell responses to targeted radionuclide therapy (TRT) and external beam radiotherapy (EBRT)", Journal of Hematology and Oncology **15**, 10.1186/S13045-022-01343-Y, (2022).

[12] M. P. Yadav, S. Ballal, C. Bal, R. K. Sahoo, N. A. Damle, M. Tripathi and A. Seth, "Efficacy and Safety of 177Lu-PSMA-617 Radioligand Therapy in Metastatic Castration-Resistant Prostate Cancer Patients", Clinical Nuclear Medicine **45**, 10.1097/RLU.0000000000002833 (2020).

[13] F. Khreish, N. Ebert, M. Ries, S. Maus, F. Rosar, H. Bohnenberger, T. Stemler, M. Saar, M. Bartholomä and S. Ezziddin, "225Ac-PSMA-617/177Lu-PSMA-617 tandem therapy of metastatic castration-resistant prostate cancer: pilot experience", European Journal of Nuclear Medicine and Molecular Imaging **47**, 10.1007/S00259-019-04612-0 (2020).

[14] C. Kratochwil et al., "Patients Resistant Against PSMA-Targeting α-Radiation Therapy Often Harbor Mutations in DNA Damage-Repair–Associated Genes", Journal of Nuclear Medicine **61**, 10.2967/JNUMED.119.234559 (2020).

[15] B. Alberts, "Molecular biology of the cell", edited by B. Alberts, 6. ed., Garland Science New York, NY [u.a.] (2015).

[16] Bingbongboing, "Cell-organelles-labeled.png", https://upload.wikimedia.org/wikipedia/commons/4/4b/Cell-organelles-labeled.png%20https://creativecommons.org/licenses/by/4.0/.

[17] Genomics Education Programme, "The cell cycle (13083554653).jpg", https://commons.wikimedia.org/wiki/File:The%7B%5C_%7Dcell%7B%5C_%7Dcycle%7B%5C_%7D(13083554653).jpg%20https://creativecommons.org/licenses/by/2.0.

[18] J. Watson and F. Crick, "Molecular Structure of Nucleic Acids: A Structure for Deoxyribose Nucleic Acid", Nature **171**, 10.1038/171737a0 (1953).

[19] J. Witkowski, "The forgotten scientists who paved the way to the double helix", Nature **568**, 10.1038/D41586-019-01176-9 (2019).

[20]H. Holliday, L. A. Baker, S. R. Junankar, S. J. Clark and A. Swarbrick, “Epigenomics of mammary gland development", Breast Cancer Research 2018 20:1 **20**, 10.1186/S13058-018-1031-X (2018).

[21]E. P. Rogakou, D. R. Pilch, A. H. Orr, V. S. Ivanova and W. M. Bonner, “DNA double-stranded breaks induce histone H2AX phosphorylation on serine 139", Journal of Biological Chemistry **273** (1998).

[22]L. J. Kou and L.-X. Yang, “γ-H2AX - A Novel Biomarker for DNA Double-strand Breaks", In Vivo **22** (2008).

[23]K. Rothkamm, “Different Means to an End: DNA Double-Strand Break Repair", Life Sciences and Radiation, 10.1007/978-3-642-18687-5_15 (2004).

[24]A. Shibata and P. A. Jeggo, “ATM’s Role in the Repair of DNA Double-Strand Breaks", Genes 2021, Vol. 12, Page 1370 **12**, 10.3390/GENES12091370 (2021).

[25]Z. Mao, M. Bozzella, A. Seluanov and V. Gorbunova, “Comparison of nonhomologous end joining and homologous recombination in human cells", DNA Repair **7**, 10.1016/J.DNAREP.2008.06.018 (2008).

[26]T. M. Pawlik and K. Keyomarsi, “Role of cell cycle in mediating sensitivity to radiotherapy", International Journal of Radiation Oncology - Biology - Physics **59**, 10.1016/J.IJROBP.2004.03.005 (2004).

[27]F. Pagliari, J. Jansen, J. Knoll, R. Hanley, J. Seco and L. Tirinato, “Cancer radioresistance is characterized by a differential lipid droplet content along the cell cycle", Cell Division **19**, 10.1186/S13008-024-00116-Y (2024).

[28]H. H. Chang, N. R. Pannunzio, N. Adachi and M. R. Lieber, “Non-homologous DNA end joining and alternative pathways to double-strand break repair", Nature Reviews Molecular Cell Biology **18**, 10.1038/nrm.2017.48 (2017).

[29]A. J. Davis, B. P. Chen and D. J. Chen, “DNA-PK: a dynamic enzyme in a versatile DSB repair pathway", DNA repair **17**, 10.1016/J.DNAREP.2014.02.020 (2014).

[30]R. X. Huang and P. K. Zhou, “DNA damage response signaling pathways and targets for radiotherapy sensitization in cancer", Signal Transduction and Targeted Therapy **5**, 10.1038/S41392-020-0150-X (2020).

[31]L. Damstrup, A. Zimmerman, C. Sirrenberg, F. Zenke and L. Vassilev, “M3814, a DNA-dependent Protein Kinase Inhibitor (DNA-PKi), Potentiates the Effect of Ionizing Radiation (IR) in Xenotransplanted Tumors in Nude Mice", International Journal of Radiation Oncology - Biology - Physics **94**, 10.1016/j.ijrobp.2015.12.268 (2016).

[32]BioRender, "Mechanism of Non-Homologous End-Joining of Double-Strand Breaks", (2025), https://app.biorender.com/biorender-templates/details/t-6422fe3c4d88d05320187825-mechanism-of-non-homologous-end-joining-of-double-strand-bre.

[33]"What Is Cancer? - National Cancer Institute", (2021), https://www.cancer.gov/about-cancer/understanding/what-is-cancer (visited on 05/09/2021).

[34]D. Hanahan and R. A. Weinberg, "Hallmarks of cancer: The next generation", Cell **144**, 10.1016/j.cell.2011.02.013 (2011).

[35]D. Hanahan, "Hallmarks of Cancer: New Dimensions", Cancer Discovery **12**, 10.1158/2159-8290.CD-21-1059 (2022).

[36]D. Hanahan and R. A. Weinberg, "The hallmarks of cancer", Cell **100**, 10.1016/s0092-8674(00)81683-9 (2000).

[37]S. Minner et al., "High level PSMA expression is associated with early psa recurrence in surgically treated prostate cancer", Prostate **71**, 10.1002/pros.21241 (2011).

[38]A. K. Rajasekaran, G. Anilkumar and J. J. Christiansen, "Is prostate-specific membrane antigen a multifunctional protein?", American Journal of Physiology - Cell Physiology **288**, 10.1152/AJPCELL.00506.2004, (2005).

[39]D. S. O'Keefe, D. J. Bacich, S. S. Huang and W. D. Heston, "A Perspective on the Evolving Story of PSMA Biology, PSMA-Based Imaging, and Endoradiotherapeutic Strategies", Journal of Nuclear Medicine **59**, 10.2967/JNUMED.117.203877 (2018).

[40]P. Curie, M. Curie and H. Becquerel, "Sur une substance nouvelle radio-active, contenue dans la pechblende ", Comptes rendus hebdomadaires des séances de l'Académie des sciences **127** (1898).

[41]A. Allisy, "Henri Becquerel: The Discovery of Radioactivity", Radiation Protection Dosimetry **68**, 10.1093/OXFORDJOURNALS.RPD.A031848 (1996).

[42]P. Grammaticos, "Pioneers of nuclear medicine, Madame Curie - PubMed", Hell J Nucl Med **7(1)** (2004).

[43]A. H. Becquerel, "On radioactivity, a new property of matter", Nobel Lecture (1903).

[44]E. Sir Rutherford, "LI. Structure of the radioactive atom and origin of the α-rays", The London, Edinburgh, and Dublin Philosophical Magazine and Journal of Science **4**, 10.1080/14786440908564361 (1927).

[45]E. Rutherford, J. Chadwick and C. D. Ellis, “Radiations from radioactive substances", Cambridge University Press(1930).

[46]P. U. Villard, “Sur le rayonnement du radium", C. R. Acad. Sci. Paris **130** (1900).

[47]L. Gerward, “Paul Villard and his Discovery of Gamma Rays", Physics in Perspective **1**, 10.1007/S000160050028/METRICS (1999).

[48]J. Chadwick, “The Neutron and Its Properties", Nobel Lectures, Physics 1922-1941 (1935).

[49]W. C. Röntgen, “A Century of X-Rays and Radioactivity in Medicine: Discovery of X rays", 1st, 2, CRC Press(1993).

[50]P. Symonds, C. Deehan, J. A. Mills and C. Meredith, “Walter and Miller’s Textbook of Radiotherapy: Radiation Physics, Therapy and Oncology", 7th ed., Churchill Livingstone(2025).

[51]W. Demtröder, “Experimentalphysik 4", 5th ed., Springer-Lehrbuch, Springer Berlin Heidelberg(2017).

[52]“NuDat 3", https://www.nndc.bnl.gov/nudat3/ (visited on 16/09/2025).

[53]A. Beiser, “Chapter 12: Nuclear Transformations. In Concepts of Modern Physics ", 6th ed., McGraw-Hill Higher Education(2003).

[54]A. V. Chalyi, “Physical Principles of Radiation Medicine. In: What is Medicine?", Springer, Cham(2024).

[55]M. Roscher, G. Bakos and M. Benešová, “Atomic Nanogenerators in Targeted Alpha Therapies: Curie’s Legacy in Modern Cancer Management", Pharmaceuticals **13**, 10.3390/PH13040076 (2020).

[56]T. Friedrich, U. Scholz, T. Elsässer, M. Durante and M. Scholz, “Systematic analysis of RBE and related quantities using a database of cell survival experiments with ion beam irradiation", Journal of Radiation Research **54**, 10.1093/JRR/RRS114 (2013).

[57]M. Durante and J. S. Loeffler, “Charged particles in radiation oncology", Nature Reviews Clinical Oncology 2009 7:1 **7**, 10.1038/nrclinonc.2009.183 (2009).

[58]IARC Working Group on the Evaluation of Carcinogenic Risks to Humans. Radiation. Lyon (FR): International Agency for Research on Cancer; 2012, “(IARC Monographs on the Evaluation of Carcinogenic Risks to Humans, No. 100D.) X- AND γ-RADIATION", https://www.ncbi.nlm.nih.gov/books/NBK304365/ (visited on 08/09/2025).

[59]M. Joiner and A. van der Kogel, “Basic Clinical Radiobiology", Vol. 4, (2009).

[60]H. Nikjoo, D. Emfietzoglou, T. Liamsuwan, R. Taleei, D. Liljequist and S. Uehara, “Radiation track, DNA damage and response - A review", Reports on Progress in Physics **79**, 10.1088/0034-4885/79/11/116601 (2016).

[61]J. F. Ward, “Biochemistry of DNA Lesions", Radiation Research **104**, 10.2307/3576637 (1985).

[62]A. J. Chalmers and R. D. Carruthers, “Radiobiology Summaries: DNA Damage and Repair", Clinical Oncology **33**, 10.1016/J.CLON.2020.12.006 (2021).

[63]M. Unverricht-Yeboah, K. Holtmann and R. Kriehuber, “Comet Assay analysis of DNA strand breaks after exposure to the DNA-incorporated Auger Electron Emitter Iodine-125", International Journal of Radiation Biology **99**, 10.1080/09553002.2020.1851059 (2023).

[64]G. Iliakis, E. Mladenov and V. Mladenova, “Necessities in the Processing of DNA Double Strand Breaks and Their Effects on Genomic Instability and Cancer", Cancers **11**, 10.3390/CANCERS11111671 (2019).

[65]D. Goodhead and D. Charlton, “Analysis of High-LET Radiation Effects in Terms of LocalEnergy Deposition", Radiation Protection Dosimetry **13**, 10.1093/RPD/13.1-4.253 (1985).

[66]N. A. Franken, R. ten Cate, P. M. Krawczyk, J. Stap, J. Haveman, J. Aten and G. W. Barendsen, “Comparison of RBE values of high- LET α-particles for the induction of DNA-DSBs, chromosome aberrations and cell reproductive death", Radiation Oncology **6**, 10.1186/1748-717X-6-64, (2011).

[67]D. T. Goodhead, “Energy deposition stochastics and track structure: what about the target?", Radiation Protection Dosimetry **122**, 10.1093/RPD/NCL498 (2006).

[68]Z. Ahmadi Ganjeh, M. Eslami-Kalantari, M. Ebrahimi Loushab and A. A. Mowlavi, “Simulation of direct DNA damages caused by alpha particles versus protons", Nuclear Instruments and Methods in Physics Research Section B: Beam Interactions with Materials and Atoms **473**, 10.1016/J.NIMB.2020.04.011 (2020).

[69]R. J. Carter, C. M. Nickson, J. M. Thompson, A. Kacperek, M. A. Hill and J. L. Parsons, “Complex DNA Damage Induced by High Linear Energy Transfer Alpha-Particles and Protons Triggers a Specific Cellular DNA Damage Response", International Journal of Radiation Oncology - Biology - Physics **100**, 10.1016/J.IJROBP.2017.11.012 (2018).

[70]J. M. Thompson, A. Elliott, S. D'Abrantes, G. O. Sawakuchi and M. A. Hill, "Tracking down alpha-particles: the design, characterisation and testing of a shallow angled alpha-particle irradiator", Radiation Protection Dosimetry **183**, 10.1093/RPD/NCY300 (2019).

[71]F. Bartoli, W. C. Eckelman, M. Boyd, R. J. Mairs and P. A. Erba, "Principles of molecular targeting for radionuclide therapy. In Nuclear Oncology", 3rd ed., Springer International Publishing(2022).

[72]M. Schäfer, U. Bauder-Wüst, M. Roscher, L. Motlová, Z. Kutilová, Y. Remde, K. D. Klika, J. Graf, C. Bařinka and M. Benešová-Schäfer, "Structure-Activity Relationships and Biological Insights into PSMA-617 and Its Derivatives with Modified Lipophilic Linker Regions", ACS Omega **10**, 10.1021/acsomega.4c10142 (2025).

[73]M. Benesová, M. Schäfer, U. Bauder-Wüst, A. Afshar-Oromieh, C. Kratochwil, W. Mier, U. Haberkorn, K. Kopka and M. Eder, "Preclinical Evaluation of a Tailor-Made DOTA-Conjugated PSMA Inhibitor with Optimized Linker Moiety for Imaging and Endoradiotherapy of Prostate Cancer", Journal of Nuclear Medicine **56**, 10.2967/JNUMED.114.147413 (2015).

[74]M. Benešová, U. Bauder-Wüst, M. Schäfer, K. D. Klika, W. Mier, U. Haberkorn, K. Kopka and M. Eder, "Linker Modification Strategies to Control the Prostate-Specific Membrane Antigen (PSMA)-Targeting and Pharmacokinetic Properties of DOTA-Conjugated PSMA Inhibitors", Journal of Medicinal Chemistry **59**, 10.1021/acs.jmedchem.5b01210 (2016).

[75]M. S. Hofman et al., "TheraP: a randomized phase 2 trial of 177Lu-PSMA-617 theranostic treatment vs cabazitaxel in progressive metastatic castration-resistant prostate cancer (Clinical Trial Protocol ANZUP 1603)", BJU International **124**, 10.1111/BJU.14876, (2019).

[76]O. Sartor et al., "Lutetium-177-PSMA-617 for Metastatic Castration-Resistant Prostate Cancer", New England Journal of Medicine **385**, 10.1056/NEJMoa2107322 (2021).

[77]G. Luurtsema, V. Pichler, S. Bongarzone, Y. Seimbille, P. Elsinga, A. Gee and J. Vercouillie, "EANM guideline for harmonisation on molar activity or specific activity of radiopharmaceuticals: impact on safety and imaging quality", EJNMMI Radiopharmacy and Chemistry **6**, 10.1186/S41181-021-00149-6/TABLES/1 (2021).

[78]E. L. Hooijman, V. Radchenko, S. W. Ling, M. Konijnenberg, T. Brabander, S. L. Koolen and E. de Blois, "Implementing Ac-225 labelled radiopharmaceuticals: practical considerations and (pre-)clinical perspectives", EJNMMI Radiopharmacy and Chemistry **9**, 10.1186/S41181-024-00239-1 (2024).

[79]S. Hertz and A. Roberts, “Radioactive Iodine in the Study of Thyroid Physiology: VII. The Use of Radioactive Iodine Therapy in Hyperthyroidism", Journal of the American Medical Association **131**, 10.1001/JAMA.1946.02870190005002 (1946).

[80]S. Zhang, X. Wang, X. Gao, X. Chen, L. Li, G. Li, C. Liu, Y. Miao, R. Wang and K. Hu, “Radiopharmaceuticals and their applications in medicine", Signal Transduction and Targeted Therapy 2024 10:1 **10**, 10.1038/s41392-024-02041-6 (2025).

[81]“Bayer Receives U.S. FDA Approval for Xofigo® (radium Ra 223 dichloride) Injection as a New Treatment for Castration-Resistant Prostate Cancer with Bone Metastases", https://www.prnewswire.com/news-releases/bayer-receives-us-fda-approval-for-xofigo-radium-ra-223-dichloride-injection-as-a-new-treatment-for-castration-resistant-prostate-cancer-with-bone-metastases-207545191.html (visited on 04/09/2025).

[82]“FDA approves lutetium Lu 177 dotatate for treatment of GEP-NETS | FDA", https://www.fda.gov/drugs/resources-information-approved-drugs/fda-approves-lutetium-lu-177-dotatate-treatment-gep-nets (visited on 11/09/2025).

[83]“FDA approves Pluvicto for metastatic castration-resistant prostate cancer | FDA", https://www.fda.gov/drugs/resources-information-approved-drugs/fda-approves-pluvicto-metastatic-castration-resistant-prostate-cancer (visited on 11/09/2025).

[84]S. E. Lapi et al., “Recent advances and impending challenges for the radiopharmaceutical sciences in oncology", The Lancet Oncology **25**, 10.1016/S1470-2045(24)00030-5 (2024).

[85]“FDA approves lutetium Lu 177 dotatate for pediatric patients 12 years and older with GEP-NETS | FDA", https://www.fda.gov/drugs/resources-information-approved-drugs/fda-approves-lutetium-lu-177-dotatate-pediatric-patients-12-years-and-older-gep-nets (visited on 04/09/2025).

[86]“FDA approves Novartis radioligand therapy Pluvicto® for earlier use before chemotherapy in PSMA-positive metastatic castration-resistant prostate cancer | Novartis", https://www.novartis.com/news/media-releases/fda-approves-novartis-radioligand-therapy-pluvicto-earlier-use-chemotherapy-psma-positive-metastatic-castration-resistant-prostate-cancer (visited on 03/09/2025).

[87]R. Khanna, P. M. Gape, K. Grayson, M. Patel and S. Y. Terry, “The Power of Precision: Unravelling the radiobiology of targeted radionuclide therapy", Clinical Oncology, 10.1016/J.CLON.2025.103923 (2025).

[88]G. Ferro-Flores, E. Azorín-Vega, B. Ocampo-García, M. Luna-Gutiérrez, P. Cruz-Nova and L. Meléndez-Alafort, "Effects of Targeted Radionuclide Therapy on Cancer Cells Beyond the Ablative Radiation Dose", International Journal of Molecular Sciences 2025, Vol. 26, Page 6968 **26**, 10.3390/IJMS26146968 (2025).

[89]N. Lepareur, B. Ramée, M. Mougin-Degraef and M. Bourgeois, "Clinical Advances and Perspectives in Targeted Radionuclide Therapy", Pharmaceutics **15**, 10.3390/PHARMACEUTICS15061733 (2023).

[90]B. S. Canter, C. N. Leung, J. Christopher Fritton, T. Bäck, D. Rajon, E. I. Azzam and R. W. Howell, "Radium-223-induced bystander effects cause DNA damage and apoptosis in disseminated tumor cells in bone marrow", Molecular cancer research **19**, 10.1158/1541-7786.MCR-21-0005 (2021).

[91]L. De Nardo, S. Santi, A. Dalla Pietà, G. Ferro-Flores, E. Azorín-Vega, E. Nascimbene, V. Barbieri, A. Zorz, A. Rosato and L. Meléndez-Alafort, "Comparison of the dosimetry and cell survival effect of 177Lu and 161Tb somatostatin analog radiopharmaceuticals in cancer cell clusters and micrometastases", EJNMMI Physics **11**, 10.1186/S40658-024-00696-2/FIGURES/12 (2024).

[92]D. Klokov, S. M. MacPhail, J. P. Banáth, J. P. Byrne and P. L. Olive, "Phosphorylated histone H2AX in relation to cell survival in tumor cells and xenografts exposed to single and fractionated doses of X-rays", Radiotherapy and Oncology **80**, 10.1016/J.RADONC.2006.07.026 (2006).

[93]"LNCaP clone FGC - CRL-1740 | ATCC", https://www.atcc.org/products/crl-1740 (visited on 28/07/2025).

[94]"C4-2 - CRL-3314 | ATCC", https://www.atcc.org/products/crl-3314 (visited on 28/07/2025).

[95]"PC-3 - CRL-1435 | ATCC", https://www.atcc.org/products/crl-1435 (visited on 28/07/2025).

[96]"Xofigo® | Bayer Vital GmbH Deutschland", https://produktinformation.bayer.de/xofigo (visited on 28/07/2025).

[97]"MultiRad225 I X-Ray Irradiation | Precision X-Ray", https://precisionxray.com/system/multirad225/ (visited on 28/07/2025).

[98]"Dose Calibrator ISOMED 2010 – Nuclear System", https://www.nuclearsystem.com/product/dose-calibrator-isomed-2010/ (visited on 28/07/2025).

[99]"ECLIPSE Ti2 Serie | Inverse Mikroskope | Produkte für die Mikroskopie | Nikon Europe B.V.", https://www.microscope.healthcare.nikon.com/de%7B%5C_%7DEU/products/inverted-microscopes/eclipse-ti2-series (visited on 28/07/2025).

[100]E. B. Community, "Jupyter Book", 10.5281/ZENODO.4539666.

[101]S. Agostinelli et al., "GEANT4 - A simulation toolkit", Nuclear Instruments and Methods in Physics Research, Section A: Accelerators, Spectrometers, Detectors and Associated Equipment **506**, 10.1016/S0168-9002(03)01368-8 (2003).

[102]"Geant4", https://geant4.web.cern.ch/ (visited on 31/07/2025).

[103]S. Incerti et al., "Geant4-DNA example applications for track structure simulations in liquid water: A report from the Geant4-DNA Project", Medical Physics **45**, 10.1002/MP.13048 (2018).

[104]H. N. Tran et al., "Review of chemical models and applications in Geant4-DNA: Report from the ESA BioRad III Project", Medical Physics, 10.1002/MP.17256 (2024).

[105]K. P. Chatzipapas et al., "Simulation of DNA damage using Geant4-DNA: an overview of the "molecularDNA" example application", Precision Radiation Oncology **7**, 10.1002/pro6.1186 (2023).

[106]S. Incerti et al., "The Geant4-DNA project", https://doi.org/10.1142/S1793962310000122 **1**, 10.1142/S1793962310000122 (2012).

[107]"Geant4-DNA", https://geant4-dna.in2p3.fr/ (visited on 31/07/2025).

[108]I. Kyriakou et al., "Review of the Geant4-DNA Simulation Toolkit for Radiobiological Applications at the Cellular and DNA Level", Cancers **14**, 10.3390/CANCERS14010035 (2021).

[109]G. Tamborino, Y. Perrot, M. De Saint-Hubert, L. Struelens, J. Nonnekens, M. De Jong, M. W. Konijnenberg and C. Villagrasa, "Modeling Early Radiation DNA Damage Occurring During 177Lu-DOTATATE Radionuclide Therapy", Journal of nuclear medicine **63**, 10.2967/JNUMED.121.262610 (2022).

[110]Z. Jalalvand, P. Zobdeh and V. Esmaeili Sani, "Assessment of early DNA damage induced in human fibroblasts by four therapeutic radionuclides using Geant4-DNA", Radiation Physics and Chemistry **219**, 10.1016/j.radphyschem.2024.111670 (2024).

[111]L. Ballisat, C. De Sio, L. Beck, S. Guatelli, D. Sakata, Y. Shi, J. Duan, J. Velthuis and A. Rosenfeld, “Dose and DNA damage modelling of diffusing alpha-emitters radiation therapy using Geant4", Physica Medica **121**, 10.1016/j.ejmp.2024.103367 (2024).

[112]K. Präbst, H. Engelhardt, S. Ringgeler and H. Hübner, “Basic colorimetric proliferation assays: MTT, WST, and resazurin", Methods in Molecular Biology **1601**, 10.1007/978-1-4939-6960-9_1 (2017).

[113]D. Lavogina et al., “Revisiting the Resazurin-Based Sensing of Cellular Viability: Widening the Application Horizon", Biosensors **12**, 10.3390/BIOS12040196/S1 (2022).

[114]J. Petiti, L. Revel and C. Divieto, “Standard Operating Procedure to Optimize Resazurin-Based Viability Assays", Biosensors **14**, 10.3390/BIOS14040156/S1 (2024).

[115]M. Mau-Sorensen et al., “Safety, clinical activity and pharmacological biomarker evaluation of the DNA-dependent protein kinase (DNA-PK) inhibitor M3814: Results from two phase I trials", Annals of Oncology **29**, 10.1093/annonc/mdy303.015 (2018).

[116]Q. Sun, Y. Guo, X. Liu, F. Czauderna, M. I. Carr, F. T. Zenke, A. Blaukat and L. T. Vassilev, “Therapeutic implications of p53 status on cancer cell fate following exposure to ionizing radiation and the DNA-PK inhibitor M3814", Molecular Cancer Research **17**, 10.1158/1541-7786.MCR-19-0362 (2019).

[117]R. Lopez Perez, N. H. Nicolay, J. C. Wolf, M. Frister, P. Schmezer, K. J. Weber and P. E. Huber, “DNA damage response of clinical carbon ion versus photon radiation in human glioblastoma cells", Radiotherapy and Oncology **133**, 10.1016/J.RADONC.2018.12.028 (2019).

[118]S. Bakr et al., “A benchmarking study of Geant4 for Auger electrons emitted by medical radioisotopes", Applied Radiation and Isotopes **174**, 10.1016/J.APRADISO.2021.109777 (2021).

[119]C. De Sio, L. Ballisat, L. Beck, S. Guatelli, D. Sakata, Y. Shi, J. Duan, L. A. Sabah, J. Velthuis and A. Rosenfeld, “Targeted alpha therapies using 211At: A Geant4 simulation of dose and DNA damage", Physica Medica **129**, 10.1016/J.EJMP.2024.104860 (2025).

[120]Hellwich Emily, “DNA damage repair inhibition and radiation therapy for lung, pancreas and HNSSC spheroids", Englisch, PhD thesis (2022).

[121]F. Graf et al., “DNA Double Strand Breaks as Predictor of Efficacy of the Alpha-Particle Emitter Ac-225 and the Electron Emitter Lu-177 for Somatostatin Receptor Targeted Radiotherapy", PLOS ONE **9**, 10.1371/JOURNAL.PONE.0088239 (2014).

[122]A. L. Jolly and A. L. Fielding, “Modelling single cell dosimetry and DNA damage of targeted alpha therapy using Monte-Carlo techniques", Physical and Engineering Sciences in Medicine, 10.1007/S13246-025-01605-2/FIGURES/6 (2025).

[123]H. Rathke, E. Winter, F. Bruchertseifer, M. Röhrich, F. L. Giesel, U. Haberkorn, A. Morgenstern and C. Kratochwil, “Deescalated 225Ac-PSMA-617 Versus 177Lu/225Ac-PSMA-617 Cocktail Therapy: A Single-Center Retrospective Analysis of 233 Patients", Journal of Nuclear Medicine **65**, 10.2967/JNUMED.123.267206 (2024).

[124]F. Borgna, S. Haller, J. M. Rodriguez, M. Ginj, P. V. Grundler, J. R. Zeevaart, U. Köster, R. Schibli, N. P. van der Meulen and C. Müller, “Combination of terbium-161 with somatostatin receptor antagonists—a potential paradigm shift for the treatment of neuroendocrine neoplasms", European Journal of Nuclear Medicine and Molecular Imaging **49**, 10.1007/S00259-021-05564-0 (2021).

[125]J. Elgqvist, O. V. Timmermand, E. Larsson and S.-E. Strand, “Radiosensitivity of Prostate Cancer Cell Lines for Irradiation from Beta Particle-emitting Radionuclide 177Lu Compared to Alpha Particles and Gamma Rays", Anticancer Research **36** (2016).

[126]K. Spoormans, M. Crabbé, L. Struelens, M. De Saint-Hubert and M. Koole, “A Review on Tumor Control Probability (TCP) and Preclinical Dosimetry in Targeted Radionuclide Therapy (TRT)", Pharmaceutics **14**, 10.3390/PHARMACEUTICS14102007 (2022).

[127]J. Raitanen, L. Palm, M. Hacker, T. Balber and M. Mitterhauser, “The importance of radiochemical purity: Cellular binding and internalization of different radiometal chlorides in prostate cancer cells", Nuclear Medicine and Biology **138-139**, 10.1016/j.nucmedbio.2024.108949 (2024).

[128]A. Lim, M. Andriotty, T. Yusufaly, G. Agasthya, B. Lee and C. Wang, “A fast Monte Carlo cell-by-cell simulation for radiobiological effects in targeted radionuclide therapy using pre-calculated single-particle-track standard DNA damage data", Frontiers in Nuclear Medicine **3**, 10.3389/fnume.2023.1284558 (2023).

[129]S. Meylan, S. Incerti, M. Karamitros, N. Tang, M. Bueno, I. Clairand and C. Villagrasa, “Simulation of early DNA damage after the irradiation of a fibroblast cell nucleus using Geant4-DNA", Scientific Reports 2017 7:1 **7**, 10.1038/s41598-017-11851-4 (2017).

[130]E. O'Neill et al., "Imaging DNA Damage Repair In Vivo After 177Lu-DOTATATE Therapy", Journal of Nuclear Medicine **61**, 10.2967/JNUMED.119.232934 (2020).

[131]W. Delbart, J. Karabet, G. Marin, S. Penninckx, J. Derrien, G. E. Ghanem, P. Flamen and Z. Wimana, "Understanding the Radiobiological Mechanisms Induced by 177Lu-DOTATATE in Comparison to External Beam Radiation Therapy", International Journal of Molecular Sciences **23**, 10.3390/IJMS232012369/S1 (2022).

[132]A. Young, R. Berry, A. F. Holloway, N. B. Blackburn, J. L. Dickinson, M. Skala, J. L. Phillips and K. H. Brettingham-Moore, "RNA-seq profiling of a radiation resistant and radiation sensitive prostate cancer cell line highlights opposing regulation of DNA repair and targets for radiosensitization", BMC Cancer **14**, 10.1186/1471-2407-14-808, (2014).

[133]S. Josson, Y. Xu, F. Fang, S. K. Dhar, D. K. St Clair and W. H. St. Clair, "RelB regulates manganese superoxide dismutase gene and resistance to ionizing radiation of prostate cancer cells.", Oncogene **25**, 10.1038/SJ.ONC.1209186 (2006).

[134]B. Van Oorschot, A. L. Oei, A. C. Nuijens, H. Rodermond, R. Hoeben, J. Stap, L. J. Stalpers and N. A. Franken, "Decay of γ-H2AX foci correlates with potentially lethal damage repair and P53 status in human colorectal carcinoma cells", Cellular and Molecular Biology Letters **19**, 10.2478/S11658-013-0113-0/METRICS (2014).

[135]A. Abramenkovs, M. Hariri, D. Spiegelberg, S. Nilsson and B. Stenerlöw, "Ra-223 induces clustered DNA damage and inhibits cell survival in several prostate cancer cell lines", Translational Oncology **26**, 10.1016/J.TRANON.2022.101543 (2022).

[136]K. Bannik, B. Madas, M. Jarzombek, A. Sutter, G. Siemeister, D. Mumberg and S. Zitzmann-Kolbe, "Radiobiological effects of the alpha emitter Ra-223 on tumor cells", Scientific Reports 2019 9:1 **9**, 10.1038/s41598-019-54884-7 (2019).

[137]L. Göring, S. Schumann, J. Müller, A. K. Buck, M. Port, M. Lassmann, H. Scherthan and U. Eberlein, "Repair of α-particle-induced DNA damage in peripheral blood mononuclear cells after internal ex vivo irradiation with", European Journal of Nuclear Medicine and Molecular Imaging, 10.1007/s00259-022-05860-3.

[138]E. A. Ruigrok, G. Tamborino, E. de Blois, S. J. Roobol, N. Verkaik, M. De Saint-Hubert, M. W. Konijnenberg, W. M. van Weerden, M. de Jong and J. Nonnekens, "In vitro dose effect relationships of actinium-225- and lutetium-177-labeled PSMA-I&T", European Journal of Nuclear Medicine and Molecular Imaging **49**, 10.1007/S00259-022-05821-W/FIGURES/4 (2022).

[139]C. Kratochwil, F. L. Giesel, F. Bruchertseifer, W. Mier, C. Apostolidis, R. Boll, K. Murphy, U. Haberkorn and A. Morgenstern, “213Bi-DOTATOC receptor-targeted alpha-radionuclide therapy induces remission in neuroendocrine tumours refractory to beta radiation: a first-in-human experience", European Journal of Nuclear Medicine and Molecular Imaging **41**, 10.1007/S00259-014-2857-9, (2014).

[140]C. Kratochwil, F. Bruchertseifer, F. L. Giesel, M. Weis, F. A. Verburg, F. Mottaghy, K. Kopka, C. Apostolidis, U. Haberkorn and A. Morgenstern, “225Ac-PSMA-617 for PSMA-Targeted α-Radiation Therapy of Metastatic Castration-Resistant Prostate Cancer", Journal of Nuclear Medicine **57**, 10.2967/JNUMED.116.178673 (2016).

[141]I. O. Lawal et al., “Hematologic toxicity profile and efficacy of [225Ac]Ac-PSMA-617 α-radioligand therapy of patients with extensive skeletal metastases of castration-resistant prostate cancer", European Journal of Nuclear Medicine and Molecular Imaging **49**, 10.1007/S00259-022-05778-W, (2022).

[142]H. Obata, M. Ogawa and M. R. Zalutsky, “DNA Repair Inhibitors: Potential Targets and Partners for Targeted Radionuclide Therapy", Pharmaceutics **15**, 10.3390/pharmaceutics15071926 (2023).

[143]M. Berger et al., “BAY-8400: A Novel Potent and Selective DNA-PK Inhibitor which Shows Synergistic Efficacy in Combination with Targeted Alpha Therapies", Journal of Medicinal Chemistry **64**, 10.1021/acs.jmedchem.1c00762 (2021).

[144]T. G. Reuvers, N. S. Verkaik, D. Stuurman, C. De Ridder, M. C. Clahsen-Van Groningen, E. De Blois and J. Nonnekens, “DNA-PKcs inhibitors sensitize neuroendocrine tumor cells to peptide receptor radionuclide therapy in vitro and in vivo", Theranostics **13**, 10.7150/THNO.82963 (2023).

[145]Y. Drew, F. T. Zenke and N. J. Curtin, “DNA damage response inhibitors in cancer therapy: lessons from the past, current status and future implications", Nature Reviews Drug Discovery 2024 24:1 **24**, 10.1038/s41573-024-01060-w (2024).

[146]E. A. Ruigrok, N. S. Verkaik, E. de Blois, C. de Ridder, D. Stuurman, S. J. Roobol, D. C. Van Gent, M. de Jong, W. M. Van Weerden and J. Nonnekens, “Preclinical Assessment of the Combination of PSMA-Targeting Radionuclide Therapy with PARP Inhibitors for Prostate Cancer Treatment", International Journal of Molecular Sciences **23**, 10.3390/IJMS23148037/S1 (2022).

[147] P. G. Prasanna, M. M. Ahmed, J. A. Hong and C. N. Coleman, “Best practices and novel approaches for the preclinical development of drug–radiotherapy combinations for cancer treatment", The Lancet Oncology **25**, 10.1016/S1470-2045(24)00199-2 (2024).

[148] K. McClellan et al., “Therapy Resistant Gastroenteropancreatic Neuroendocrine Tumors", Cancers 2022, Vol. 14, Page 4769 **14**, 10.3390/CANCERS14194769 (2022).

[149] A. Tartas Id, L. Lundholm, H. Scherthan, A. Wojcik and B. Brzozowska, “The order of sequential exposure of U2OS cells to gamma and alpha radiation influences the formation and decay dynamics of NBS1 foci", PLOS ONE **18**, 10.1371/JOURNAL.PONE.0286902 (2023).

[150] M. Williams, “It takes a community to raise a scientist | Plant Science Today", (2015), https://blog.aspb.org/it-takes-a-community-to-raise-a-scientist/ (visited on 14/09/2025).

Acknowledgments

"It takes a community to raise a scientist" (Mary Williams, [150])

This quote reflects my feelings and thoughts closely. Many people have accompanied me and made an important contribution to my journey towards this milestone. They gave me roots, helping me feel grounded and confident, and wings to be curious and explore new ideas. Thanks to the support of colleagues, mentors, and friends, I have been able to grow both personally and scientifically during this time. I am truly grateful to everyone who accompanied me and shared a part of this journey.

To my working group - thank you for welcoming me with open arms. Each of you has played a part in this PhD: from traveling to Berlin to support intense experiments, to introducing me to the wonders of (radio)chemistry and peptide synthesis with passion and patience. You made long days enjoyable with baked goods (sweet and salty!), legendary picnics, and shared laughs. You gave valuable feedback on abstracts and posters, and most importantly, you shared the ups and downs of PhD life. It is the small things that made the biggest difference, and I am truly grateful for this wonderful community that became like a family along the way.

I owe special gratitude and appreciation to my direct supervisor and mentor, Martina, who believed in my potential from the very beginning and helped me grow, giving me wings both figuratively and literally (especially when it came to conferences in Hawaii and Australia, and research stays in Bordeaux and Canada). You have always supported me - even at the bench, pipette in hand - and encouraged me to pursue my own ideas. Thank you for the freedom, trust, and confidence you gave me to shape my own scientific path.

To my co-supervisor, Ramon - thank you for your encouraging support throughout this entire project, especially on the biological side. I am truly grateful for all the time you spent introducing me to new methods, discussing results, and generously sharing your expertise along the way.

I would like to express my sincere gratitude to Prof. Dr. Mark Ladd for his guidance as my first supervisor and for his steady support throughout all phases of this work.
I am also deeply grateful to Prof. Dr. Leif Schröder for kindly taking on the role of second reviewer. My sincere thanks go as well to Prof. Dr. Loredana Gastaldo and Priv.-Doz. Dr. Zoltán Harman for accepting the invitation to take part in the examination committee. Your time and commitment are truly appreciated.
My heartfelt thanks go to Prof. Dr. Michael Hausmann for serving as a valued member of my Thesis Advisory Committee and for contributing to the success of this project with his expertise and thoughtful feedback.

Furthermore, this work would not have been possible without collaboration and the openness of colleagues to share their lab spaces, as the experiments were conducted in multiple labs across different buildings and even cities, for some time. I would like to thank everybody who supported the experimental part of this project by granting me access to their lab spaces and equipment, such as microscopes, and providing valuable guidance, while always being open and supportive in finding reasonable solutions to challenges. Special thanks to Rosemarie, who was very helpful whenever there were any issues with the microscope. Additionally, I would particularly like to thank Barbara from the Department of Radiation Protection, who accompanied a large part of this project and made some experiments possible in the first place. Thank you for your valuable trust, optimism, and support.
Moreover, this project was shaped by two international research collaborations whose members welcomed me with open minds and open arms. Thank you very much, Svetlana, for giving me an unforgettable experience and valuable insights at the CNL in Canada. I am truly grateful for this opportunity and for all the memories I collected during that month. Likewise, I would like to thank Prof. Incerti and Dr. Tran for inviting me to visit the Laboratoire de Physique des Deux Infinis (LP2i) at Bordeaux and for supporting me in this project by providing knowledge and assistance for the Geant4 DNA simulation framework.

Lastly, I would like to express my warmest and most heartfelt thanks to the people who shared the everyday moments with me during this time, and whose support and advice I could always rely on.
To my PhD colleagues and trusted companions, Mariam and Julian. Throughout this journey, it was incredibly helpful to have someone to relate to who was going through similar struggles and could offer advice or simply a supportive ear. This

PhD experience would not have been the same without our coffee breaks and unforgettable, laughter-filled cooking evenings.
To my family and friends - especially the LeBinPhys - thank you for your unconditional support. Some of you have been there since the very beginning of my studies, now a decade ago. I would not have come this far without you. I am deeply grateful for the close-knit group that was forged through long hours and late-night discussions over exercise sheets.
To Tom, to whom my profoundly heartfelt thanks belong, for being by my side through all the ups and downs of this PhD journey - supporting me from the very first step, editing my application video for the DKFZ PhD program, all the way to the final writing phase of this thesis. Thank you for listening to all my worries, complaints, and ideas, for sharing your valuable insights during scientific discussions, and for encouraging and motivating me when I was struggling and believing in me when I felt doubtful.